

**Design and characterisation of Ni-matrix  
nanocomposite films reinforced with Ag-coated  
SnO<sub>2</sub> nanowires for electrical contact applications**

Dissertation  
zur Erlangung des Grades  
des Doktors der Ingenieurwissenschaften  
der Naturwissenschaftlich-Technischen Fakultät III  
Chemie, Pharmazie, Bio- und Werkstoffwissenschaften  
der Universität des Saarlandes



von

Federico Luis Miguel

Saarbrücken

2016

<b>Tag des Kolloquiums:</b>	08.06.2016
<b>Dekan:</b>	Prof. Dr. Dirk Bähre
<b>Berichterstatter:</b>	Prof. Dr. Frank Mücklich Prof. Dr. Christian Motz
<b>Vorsitz:</b>	Prof. Dr. Martin Müser
<b>Akad. Mitarbeiter:</b>	Dr. Anne Jung

# Acknowledgements

I am deeply grateful to Prof. Dr. Frank Mücklich for giving me the unique opportunity to form part of his research group and conduct this doctoral thesis as well as for his kind and steady support throughout this endeavour. Special thanks also to Prof. Dr. Christian Motz for accepting the revision of this work. I would like as well to acknowledge the Roberto Rocca Education Program and the German Academic Exchange Service (DAAD) for their financial support.

Prof. Dr. Sanjay Mathur and Dr. Ralf Müller deserve a special mention for their essential contribution to this project by providing state-of-the-art nanowires for the production of the studied composite material. I wish to thank also Prof. Dr. Rolf Hempelmann for allowing me to use his electrochemistry laboratories and Dr. Martin Weinmann for his guidance during the electrodeposition experiments.

I owe my deepest gratitude to my dear colleagues Dr. Flavio Soldera, Dr. Sebastián Suárez, Federico Lasserre and Nicolás Souza for their invaluable support and countless contributions to my work as well as for their unconditional friendship along these years. I am also particularly grateful to Dr. Carsten Gachot and Dr. Andreas Rosenkranz for their insightful comments and suggestions as well as to Christoph Pauly for his diligent assistance with everything related to electron microscopy analysis.

Finally, I cannot thank my brother and parents enough for being always there for me, no matter the circumstances or distance, and my girlfriend Gyöngyi, who has been a warm, loving companion during each and every step of this journey.

## Abstract

This work introduces a novel composite film, which was developed to be applied as electrode material in electrical-contact devices. It consists of a Ni matrix reinforced with Ag-coated SnO<sub>2</sub> nanowires, whose processing combines different techniques, namely chemical vapour deposition (SnO<sub>2</sub>), electroless (Ag) and electrodeposition (Ni). The composite was investigated regarding its microstructure, mechanical properties, tribological behaviour, thermal stability and electrical resistivity. The microstructure analysis suggested that the secondary phases act as barrier for grain-boundary migration, promoting a fine grain morphology in the matrix. This was responsible for an overall increase in hardness and strength with respect to Ni reference samples, in agreement with the Hall-Petch relation. Consequently, the evaluation of friction and wear under dry-sliding conditions proved an enhanced wear resistance. The study of thermal stability on annealed samples revealed a limited grain growth and the absence of texture development, which derived from the combined effects of reduced grain-boundary mobility and non-miscibility of the phases. Finally, the analysis of electrical resistivity measurements showed that the insulating effect of the nanowires and microstructural defects is balanced by the highly conductive Ag phase.

## Zusammenfassung

Diese Arbeit beschäftigt sich mit einer neuartigen Komposit-Schicht, die als Elektrodenmaterial für elektrische Kontaktgeräten entwickelt wurde. Diese besteht aus einer mit Ag-beschichteten SnO<sub>2</sub>-Nanodrähten verstärkten Ni-Matrix. Zur Herstellung dieses Komposits wurde eine Kombination von verschiedenen Verfahren genutzt, d.h., chemische Gasphasenabscheidung (SnO<sub>2</sub>), Stromlos (Ag) und galvanische Abscheidung (Ni). Der Verbundwerkstoff wurde hinsichtlich Mikrostruktur, mechanischen Eigenschaften, tribologischem Verhalten, thermischer Stabilität sowie elektrischem Widerstand charakterisiert. Die Mikrostrukturanalyse belegte, dass die sekundären Phasen als Barriere für Korngrenzenmigration wirken, wobei diese eine feine Kornmorphologie in der Matrix hervorrufen. Dies führte, übereinstimmend mit der Hall-Petch Beziehung, zu einer Erhöhung der Härte und Festigkeit im Vergleich zu den Ni-Referenzproben. Infolgedessen, konnte ein erhöhter Verschleißwiderstand unter trockenen Reibbedingungen nachgewiesen werden. Die Untersuchung der thermischen Stabilität von geblühten Proben zeigte ein verringertes Kornwachstum sowie keine Texturentwicklung. Dies lässt sich auf die verringerte Korngrenzmobilität und die Unmischbarkeit der Phasen zurückführen. Abschließend konnte aus elektrischen Widerstandsmessungen gefolgert werden, dass der isolierende Effekt der Nanodrähte und der mikrostrukturellen Defekte von der hochleitenden Ag-Phase ausgeglichen wird.

# Contents

<b>Acknowledgements</b> .....	I
<b>Abstract</b> .....	II
<b>Zusammenfassung</b> .....	III
<b>Contents</b> .....	IV
<b>List of symbols</b> .....	VII
<b>List of abbreviations</b> .....	IX
<b>1 Introduction</b> .....	1
1.1 Motivation and aim of the work .....	1
1.2 Structure of the work.....	3
1.3 Related peer-reviewed publications .....	4
<b>2 Theory and state of the art</b> .....	5
2.1 Methods for the production of metallic films and coatings .....	5
2.1.1 Chemical vapour deposition.....	5
2.1.2 Chemical vapour deposition of Ni films.....	6
2.1.3 Physical vapour deposition (PVD) .....	6
2.1.3.1 Sputter deposition.....	7
2.1.3.2 Other PVD methods .....	7
2.1.4 Electrochemical deposition methods .....	8
2.1.4.1 Electroless deposition.....	9
2.1.4.2 Electrodeposition .....	9
2.1.5 Cladding deposition .....	11
2.1.6 Thermal spraying.....	13
2.2 Ni and its application in coating materials .....	13
2.2.1 Pure-Ni coatings for decorative and engineering applications.....	15
2.2.2 Ni-alloy films and coatings produced by electrodeposition.....	17
2.2.3 Electroless Ni-alloy coatings .....	18
2.2.3.1 Ni-P alloys .....	19
2.2.3.2 Ni-B alloys.....	19
2.2.3.3 Polyalloy and composite coatings based on Ni-P and Ni-B .....	20
2.3 Electrical contact materials and applications.....	21

2.3.1 Overview of electrical contact materials .....	22
2.4 The Ni-Ag system.....	23
2.5 The science of SnO <sub>2</sub> .....	25
<b>3 Materials and methods</b> .....	<b>27</b>
3.1 Fabrication procedure of Ni-Ag-SnO <sub>2</sub> composite films.....	27
3.1.1 Synthesis of SnO <sub>2</sub> nanowires.....	27
3.1.2 Electroless Ag deposition onto SnO <sub>2</sub> nanowires .....	27
3.1.3 Electrodeposition of the Ni matrix.....	29
3.1.4 Specific-purpose isothermal annealing.....	31
3.2 Material characterisation techniques .....	32
3.2.1 Focused ion beam (FIB) and scanning electron microscopy (SEM) .....	32
3.2.2 Electron backscatter diffraction (EBSD) .....	33
3.2.3 Energy-dispersive X-ray spectroscopy (EDS) .....	33
3.2.4 Transmission electron microscopy (TEM) .....	33
3.2.5 Atomic-force microscopy (AFM).....	33
3.2.6 High-temperature X-ray diffraction (XRD).....	33
3.2.7 Nanoindentation for the analysis of mechanical properties .....	34
3.2.8 Friction and wear evaluation .....	35
3.2.8.1 White-light interferometry (WLI).....	36
3.2.9 Four-point probe electrical resistivity measurements.....	36
<b>4 Microstructure and mechanical properties characterisation</b> .....	<b>37</b>
4.1 Introduction.....	37
4.2 Experimental details .....	38
4.3 Results and discussion .....	38
4.3.1 Microstructure characterisation.....	38
4.3.2 Mechanical properties evaluation.....	45
4.3.2.1 Hardness.....	45
4.3.2.2 Young's modulus.....	49
4.3.2.3 Evaluation of the stress-strain relationship from nanoindentation data.....	50
4.4 Conclusions .....	53
<b>5 Analysis of the dry-sliding friction and wear behaviour</b> .....	<b>55</b>
5.1 Introduction.....	55

5.2	Experimental details .....	56
5.3	Results and discussion .....	56
5.3.1	Analysis of the wear tracks and subsurface microstructure.....	58
5.3.2	Analysis of the dynamic friction coefficient.....	63
5.3.3	Analysis and modelling of the wear volume .....	66
5.3.4	Modelling and evaluation of the wear rate.....	71
5.3.4.1	Generalisation of the normal-displacement parameters $\alpha$ and $\beta$ .....	75
5.4	Conclusions .....	76
<b>6</b>	<b>Analisis of the microstructural thermal stability.....</b>	<b>78</b>
6.1	Introduction.....	78
6.2	Experimental details .....	79
6.3	Results and discussion .....	79
6.3.1	Microstructural features of the as-deposited films.....	79
6.3.2	Analysis of the thermal stability by means of different annealing treatments .....	82
6.3.2.1	In-situ XRD analysis during non-isothermal annealing.....	83
6.3.2.2	Microstructure characterisation after isothermal annealing at elevated temperature .....	87
6.3.2.3	Abnormal growth at the onset temperature of grain growth .....	94
6.4	Conclusions .....	96
<b>7</b>	<b>Electrical resistivity evaluation .....</b>	<b>98</b>
7.1	Introduction.....	98
7.2	Experimental details .....	98
7.3	Results and discussion .....	99
7.4	Conclusions .....	102
<b>8</b>	<b>Summary and outlook.....</b>	<b>103</b>
8.1	Summary.....	103
8.2	Outlook .....	105
	<b>References.....</b>	<b>107</b>
	<b>List of figures .....</b>	<b>125</b>
	<b>List of tables .....</b>	<b>129</b>

## List of symbols

$y$	Positive charge value
$z$	Valence number
$2\theta$	Diffraction angle
$H$	Hardness
$F$	Normal load
$h$	Indenter's maximum displacement
$S$	Contact rigidity
$h_c$	Depth of contact of the indenter with the sample
$\epsilon$	Parameter related to the elastic deformation during nanoindentation
$A_c$	Projected area of contact during indentation
$E_r$	Reduced Young's modulus
$E$	Young's modulus
$\nu$	Poisson's ratio
$f$	Cycle frequency
$W$	Wear volume
$R_q$	Root-mean-squared roughness
$\rho$	Bulk electrical resistivity
$I$	Current
$Ni_{cg}$	Coarse-grained Ni
$Ni_{fg}$	Fine-grained Ni
$d_A$	Mean area-weighted grain size
$H_0$	Intercept of Hall-Petch (hardness) equation
$k_H$	Slope of Hall-Petch (hardness) equation
$d$	Grain diameter in Hall-Petch equation
$R^2$	Coefficient of determination
$E_0$	Porosity-free elastic modulus in the Watchman and Mackenzie relation
$p$	Porosity
$f_i$	Constant parameters of the Watchman and Mackenzie relation
$\sigma$	Stress
$\epsilon$	Strain
$\sigma_y$	Initial yield strength
$K$	Constant parameter of the power-law work-hardening equation
$n$	Work-hardening coefficient
$\sigma_{8\%}$	Stress corresponding to a representative strain of 8%
$\sigma_{y0}$	Intercept of Hall-Petch (yield stress) equation
$k_y$	Slope of Hall-Petch (yield stress) equation
$\mu$	Dynamic-friction coefficient

$f_{AB}$	Zum Gahr's cutting-efficiency parameter
$A_A$	Cross-sectional area of the side ridges of a wear track
$A_B$	Cross-sectional area of the groove of a wear track
$p_{max}$	Maximal contact pressure by Hertzian elastic contact
$R$	Radius of sliding sphere
$\Delta T_{flash}$	Flash temperature as the temperature difference with respect to the bulk
$k$	Archard's wear coefficient
$x$	Sliding distance
$A$	Slope of the linear relation between wear volume and hardness
$B$	Intercept of the linear relation between wear volume and hardness
$a_i$	Coefficients (2) of linear relation between $A$ and $F$
$b_i$	Coefficients (2) of linear relation between $B$ and $F$
$L$	Length of wear track
$\eta$	Total number of cycles in a wear test
$W_{100}$	Wear volume after 100 cycles
$D$	Normal displacement of the sliding ball, i.e., penetration depth
$N$	Cycle number
$\alpha$	Parameter of the fitting function relating $D$ and $N$ (1/2)
$\beta$	Parameter of the fitting function relating $D$ and $N$ (2/2)
$t$	Total time elapsed after $N$ cycles
$\alpha_H$	$\alpha$ expressed as a function of $H$
$c_i$	Coefficients (2) of the linear relation between $\alpha$ and $H$
$\beta_m$	Mean value of $\beta$ from all samples of the same type
$\alpha_{LF}$	Linear-thermal-expansion coefficient of the film
$\alpha_{LS}$	Linear-thermal-expansion coefficient of the substrate
$\Delta T$	Temperature change
$\alpha_L$	Linear thermal-expansion coefficient
$I(hkl)$	Integrated intensity of the (hkl) reflection from a film sample
$I_0(hkl)$	Integrated intensity of the (hkl) reflection from a standard powder sample
$N_R$	Total number of reflections used in relative texture coefficient analysis
$C$	Constant from Johnson-Mehl-Avrami-Kolmogorov equation
$r$	Constant from Johnson-Mehl-Avrami-Kolmogorov equation
$\tau$	Elapsed time during recrystallization and growth
$d_0$	Initial average grain radius in normal-growth power law
$d_f$	Final average grain radius in normal-growth power law
$m$	Grain-growth exponent in normal-growth power law
$\kappa$	Constant in normal-growth power law
$C_{ij}$	Stiffness constants
$f_T$	Frequency of nucleation of the texture orientation

$f_R$	Frequency expected for random nucleation
$d_T$	Average diameter of the grains with the preferred orientation
$d_R$	Average diameter of the grains with random orientation
$\rho$	Bulk electrical resistivity
$V$	Voltage
$I$	Current
$t_f$	Film thickness
$F_g$	Geometry factor

## List of abbreviations

CVD	Chemical vapour deposition
PVD	Physical vapour deposition
Red	Reductant
Me	Metal
FCC	Face-centred cubic
BCC	Body-centred cubic
HCP	Hexagonal close-packed
VLS	Vapour-liquid-solid
FIB	Focused ion beam
SEM	Scanning electron microscopy
STEM	Scanning transmission electron microscopy
EBSD	Electron backscatter diffraction
CI	Confidence index
EDS	Energy-dispersive X-ray spectroscopy
TEM	Transmission electron microscopy
SAD	Selected-area diffraction
AFM	Atomic-force microscopy
XRD	X-ray diffraction
WLI	White-light interferometry
FWHM	Full width at half maximum
RTC	Relative texture coefficient
JMAK	Johnson-Mehl-Avrami-Kolmogorov

# 1 Introduction

## 1.1 Motivation and aim of the work

A chain is only as strong as its weakest link. This old proverb can be used to symbolise the importance of surface engineering in materials science. Due to their singular structure and being continuously exposed to the action of external agents, surfaces are generally the most vulnerable part of materials and components. A conventional approach for preserving their integrity and functionality is the application of protective films or coatings. In this manner, it is possible not only to introduce or enhance specific features and properties, extending the capabilities and working life of the whole system, but also to reduce costs by employing less expensive materials for the core.

In the particular case of electrical contact applications, the involved materials might be faced against a broad variety of detrimental phenomena, which can originate from mechanical, chemical, thermal and electrical interactions, just to name some. For mild load regimes, some base metals or simple alloys are able to meet the system's demands. However, for heavy duty applications or severe environmental conditions, more complex solutions are often required. Under these circumstances, a conventional alternative is given by the use of composite materials, which display unique properties as a result of the different nature of their constituent phases. In several cases, these are applied in the form of thin films and coatings, with thickness ranging between 0.1 and 100  $\mu\text{m}$  [1]. The shortcomings of these materials are their quite limited field of applicability (restricted to a set of very specific working conditions and devices) and that the sought enhancement of certain properties is achieved most frequently at the expense of a loss in performance in other areas.

In view of this, it is the aim of the present work to develop a novel type of metal-matrix composite film, which would find application as electrode material in electrical-contact systems. Said composite should possess tailored properties, which would allow meeting the demands of different sorts of devices over a wide range of mild to severe operating conditions (in terms of current, temperature and mechanical stresses, among others). Moreover, aiming to reach a broader technological segment, the processing technique should make possible its fabrication both for small-sized devices and as coatings on relatively large components. Attending to these premises, the composite in question was designed upon the following elements:

- *SnO<sub>2</sub> nanowires as reinforcing phase.* SnO<sub>2</sub> particles and fibres are widely used in composite materials for electrical contact applications for inhibiting electrode welding [2–4]. In this work, arrays of single-crystalline, one-dimensional nanowires are synthesised via chemical vapour deposition (CVD), which would be later embedded in the matrix while still standing, adhered, on the substrate. The anchoring of the wires by the substrate would assist in preventing the formation of oxide agglomerates (and the associated porosity), which usually takes place upon few switching operations. Moreover, the nanowires could eventually hinder grain-boundary mobility, which might enhance the mechanical properties and thermal stability of the composite.
- *Ni as matrix material.* Ni possesses good resistance to oxidation and corrosion as well as relatively high electrical and thermal conductivities [5]. The matrix is here applied by the electrodeposition method, which allows an accurate control of the process and provides several means for tailoring the microstructure. Moreover, Ni electrodeposits are well-known for their remarkable mechanical properties, which might in turn result in a higher wear resistance of electrodes during sliding or fretting events [6–8].
- *Ag as binding phase.* The nanowires are coated with Ag using the electroless method, with the main purpose of decreasing the effective electrical resistivity of the system and to provide a conductive surface for the electrodeposition of the matrix. In addition, Ag has virtually neither solubility nor reactivity with Ni [9], what is quite important for the thermal stability of the films.

According to its composition, this novel composite material will be referred from here onwards as Ni-Ag-SnO<sub>2</sub>. Whether or not it is actually possible to successfully produce this material (having such a specific configuration) is not a trivial matter. A multistep fabrication route was conceived specifically to that end, which combines the CVD, electroless and electrodeposition techniques. The success in this attempt will be determined not only by the structural integrity of the composite film but also by the quality and potential of its attributes. To that end, different aspects will be investigated, concerning features and properties of high relevance both for technical applications in general and, more specifically, for electrical contact materials. The selected topics include:

- *Microstructure.* It is the key to understanding the relationship between processing and material properties, making its analysis an important optimisation tool.

- *Mechanical properties.* High mechanical strength is a requisite for preventing severe wear between contacting electrodes and for avoiding their plastic deformation due to repeated bumping and bouncing during closure operations.
- *Tribological behaviour.* Both moving and stationary contacts sustain damage from friction and wear related phenomena, which shortens their working life. Especially relevant is the case of fretting wear, given by the small-amplitude reciprocating motion experienced by closed electrodes.
- *Thermal stability.* Heat-triggered microstructural changes may well result in the degradation of material properties, such as the loss of mechanical strength. Electrical contacts might experience this both locally (by friction or arc discharges) and in a widespread manner (by Joule heating).
- *Electrical resistivity.* Affects the extent of Joule heating and thus the dissipation of energy, which determines the electrical efficiency of the device.

During the analysis of these topics, the main emphasis will be placed on discerning the fundamental mechanisms responsible for the experimental observations as well as on the individual contribution of the three constituent phases and their mutual interactions.

## 1.2 Structure of the work

Following the introductory aspects described in the present chapter, a selection of topics closely related to the work reported in this doctoral thesis is reviewed in chapter 2, establishing a broad theoretical and technical background.

Chapter 3 provides a thorough description of the fabrication procedure which was developed for assembling the Ni-Ag-SnO<sub>2</sub> composite films. Afterwards, the different characterisation techniques applied are summarised, together with related experimental parameters.

Next, the results of the different investigations are detailed and discussed, comprising the microstructure characterisation and analysis of mechanical properties (chapter 4); the study of the tribological behaviour under dry-sliding conditions (chapter 5); the evaluation of thermal stability, regarding the evolution of grain size and crystallographic texture induced by annealing (chapter 6); and the assessment of the electrical resistivity and its determining factors (chapter 7).

At last, chapter 8 summarises the main results previously discussed and suggests a series of topics for future research, which would complement and expand on the findings of the present work.

### **1.3 Related peer-reviewed publications**

The experimental results described in this doctoral thesis (chapters 4 through 7) have been fully or partially published in different peer-reviewed journals in the field of materials science. This is detailed next.

#### *Chapter 4:*

- F.L. Miguel, R. Müller, M. Weinmann, R. Hempelmann, S. Mathur, F. Mücklich, Production and characterization of nanocomposite thin films based on Ni matrix reinforced with SnO<sub>2</sub> single-crystalline nanowires for electrical contact applications, *J. Alloys Compd.* 603 (2014) 14–18.
- F.L. Miguel, R. Müller, S. Mathur, F. Mücklich, Microstructure and mechanical properties of electrodeposited Ni and Ni–matrix-nanocomposite thin films, *Mater. Sci. Eng. A.* 646 (2015) 254–262.

#### *Chapter 5:*

- F.L. Miguel, R. Müller, A. Rosenkranz, S. Mathur, F. Mücklich, Analysis and modelling of the dry-sliding friction and wear behaviour of electrodeposited Ni and Ni-matrix-nanocomposite films, *Wear.* 346-347 (2016) 87–98.

#### *Chapter 6:*

- F.L. Miguel, R. Müller, S. Mathur, F. Mücklich, On the thermal stability of electrodeposited Ni-matrix-nanocomposite films reinforced with Ag-coated SnO<sub>2</sub> nanowires, *Surf. Coatings Technol.* 287 (2016) 93–102.

Additional findings which do not explicitly form part of this thesis, but yet set the foundations upon which this research project was established, are available in:

- F.L. Miguel, H. Shen, F. Soldera, T. Fischer, R. Müller, S. Mathur, F. Mücklich, Electroless deposition of a Ag matrix on semiconducting one-dimensional nanostructures, *Thin Solid Films.* 536 (2013) 54–56.

## 2 Theory and state of the art

This chapter reviews several topics related to the research presented in this doctoral thesis, providing a thorough theoretical and technical background for assisting the reader in the interpretation of this work's findings. First, the main techniques available for the deposition of metallic films and coatings are described. Next in order is the characterisation of a rich variety of Ni-based films and coatings, whose properties attracted interest in both the academic and industrial spheres. Here, the focus is placed on those produced by means of electrochemical techniques (i.e., electroless and electrodeposition), since these are certainly the most technically relevant and also play a major role in the fabrication of the Ni-Ag-SnO<sub>2</sub> film. Following, a brief review of electrical contact materials and their applications is provided. Then, closing the chapter, the components of the composite under study are analysed regarding their features and applications, starting with the Ni-Ag system and concluding with the most remarkable aspects of SnO<sub>2</sub>, with emphasis on nanowires.

### 2.1 Methods for the production of metallic films and coatings

The available literature presents a remarkably large number of film fabrication techniques, which allow obtaining specimens with a thickness ranging from few nanometres up to several millimetres. The most relevant among them are here briefly reviewed, with focus on those able to deposit metal-based coatings. Special attention is given to Ni-related deposition procedures, being this metal the main constituent of the Ni-Ag-SnO<sub>2</sub> composite film under evaluation.

#### 2.1.1 Chemical vapour deposition

During CVD, a chemical reaction in the vapour phase results in the formation of a solid film over a heated surface by the progressive deposition of atoms and/or molecules (atomistic process). Its main advantages are the adaptability to complex substrate geometries and fast reaction rates which allow producing both very thin films and thick coatings. However, it requires in many cases temperatures of 600 °C and above, which is enough for many substrate materials to become unstable [10]. A large variety of materials can be deposited by CVD, including metals (pure, alloys and intermetallics), carbon allotropes, semiconductors (e.g., Si and Ge) and ceramics (e.g., carbides, nitrides and metal-oxides).

One of the key aspects of CVD is the selection of the precursor gases, which are the source of the chemical species which react to produce the desired film. These fall into several general groups, namely halides, carbonyls, hydrides and metallo-organics. Depending on the type of precursors involved and the specific material to be deposited, the nature of the CVD reactions can vary (e.g., thermal decomposition, H<sub>2</sub> reduction, oxidation, hydrolysis, nitridation, etc.) and their activation may be thermally induced by laser or other light sources (standard CVD) or assisted by plasma. The general sequence of events taking place during CVD reactions are summarised in Fig. 2.1.

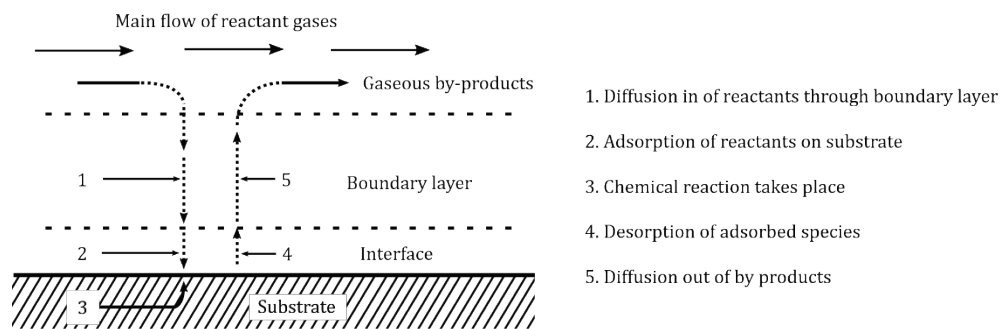
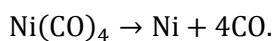


**Fig. 2.1** Sequence of events during CVD reactions (adapted from [10]).

### 2.1.2 Chemical vapour deposition of Ni films

The most common reaction for the CVD of Ni is the decomposition of Ni carbonyl [10,11]:



The optimum temperature for this reaction ranges between 180 and 200 °C, at pressures of up to 1 bar. This reaction can proceed either thermally activated or assisted by laser. Other routes are the H<sub>2</sub> reduction of the alkyl Ni(C<sub>5</sub>H<sub>5</sub>)<sub>2</sub> [12] or the chelate complex Ni(C<sub>5</sub>HF<sub>6</sub>O<sub>2</sub>)<sub>2</sub> [13] at 200 and 250 °C, respectively. Such films are readily found in moulds and dies, structural parts and electrical contacts.

### 2.1.3 Physical vapour deposition (PVD)

Like CVD, PVD is an atomistic process where the deposited species are atoms or molecules. Here, the material is vaporised from a solid or liquid source and then transported in gas form towards a substrate, where it condenses. Unlike in CVD, no chemical reaction takes place. PVD can be carried out in different environments, namely vacuum, low-pressure gas or plasma. The deposition rates are much slower than in CVD, therefore the thickness of the

deposits normally ranges from some nanometres up to several micrometres. PVD can be used to produce all sorts of single-element materials and compounds.

PVD methods can be classified, according to the way in which the target material is vaporised, as: vacuum evaporation, arc vapour deposition, ion assisted deposition and sputtering [14–16]. The latter category comprises the most relevant and widespread PVD techniques to be found in the literature, which are briefly summarised next.

### **2.1.3.1 Sputter deposition**

This family of PVD procedures is characterised by a non-thermal vaporisation process. Atoms from a target material are ejected from their positions by the momentum transfer from bombarding particles, which are usually gaseous ions accelerated from a plasma by an electric field. Some of the vaporised target atoms, travelling in all directions, reach the substrate and adsorb. Some compounds (e.g., TiN and ZrN) can be deposited by interposing a reacting gas in the trajectory of the ejected ions, with whom it reacts to form the compound [17]. Sputter-deposited films are widely used for metallisation of semiconductors, as reflective and magnetic coatings in recording media and for dry lubrication, among several other applications [14].

There are various sputter PVD configurations readily available, which may differ, for instance, in the nature of the applied potential (direct or alternate current, the latter at low up to radio frequency) or the location of the plasma generation (in the chamber or externally). Among them, magnetron sputtering is the most spread PVD technique [18,19]. Here, the secondary electrons emitted by the target are forced to stay close to it and follow a spiral trajectory over its surface, under the influence of a magnetic field. This enhances the ionisation and collision processes, thus increasing the sputtering yield. A typical magnetron configuration is displayed in Fig. 2.2.

### **2.1.3.2 Other PVD methods**

As before mentioned, the vaporisation of the source material can proceed by other methods aside from sputtering. In the vacuum deposition PVD, the source's atoms are thermally vaporised and follow afterwards a quasi-linear trajectory towards the substrate, mostly without collisions along it. Another alternative is the use of electric arcs to vaporise the source material, produced with high currents coupled with low voltages. Since the resulting vapour

is highly ionised, a bias is usually set on the substrate in order to accelerate the film's ions towards it.

Complementing the PVD techniques described so far, the method known as ion-assisted deposition is characterised by the bombardment of the deposited film by atom-sized energetic particles, in order to alter its formation process and thus control its properties [21]. This can be implemented in most of the PVD procedures already discussed.

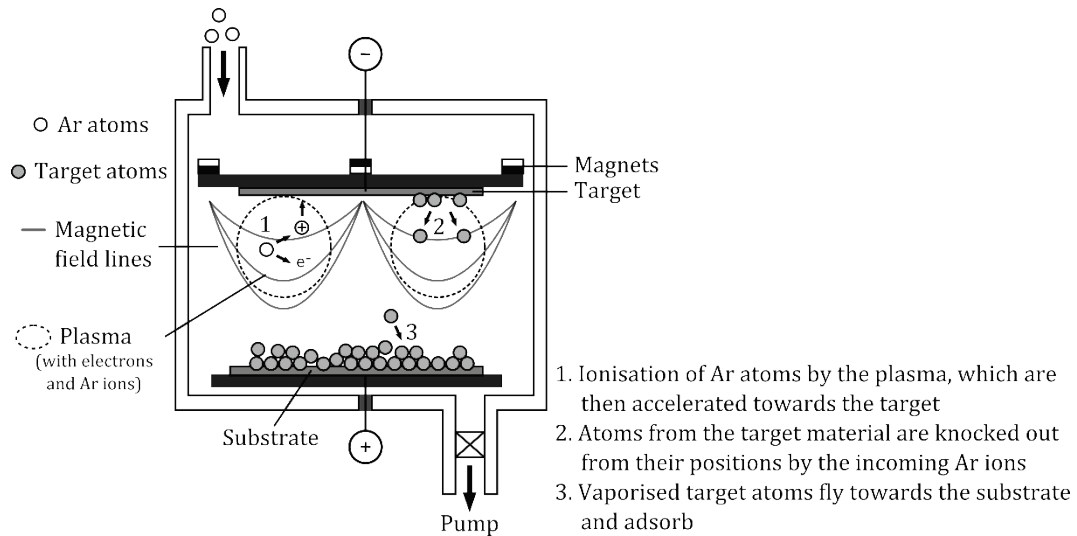


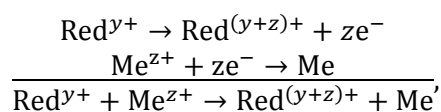
**Fig. 2.2** Portrayal of a typical magnetron sputtering setup and the basic sequence of events during film deposition [20]. Electrons travelling close to the target (forced by a magnetic field) enhance ionisation and collision processes, increasing the sputtering yield.

#### 2.1.4 Electrochemical deposition methods

These involve a series of techniques by which metallic films or coatings are deposited onto a substrate by means of an electrochemical reaction which, in most cases, takes place in an aqueous solution (atomistic process). Here, dissolved metal cations are reduced on a surface, forming a coherent metallic layer. This family of methods is by far the most used in industrial applications given its versatility, fast deposition rates, high scalability and relatively simple setup and operation. It can be divided into two main classes, namely electroless and electrodeposition, which differ primarily in the source providing the electrons which are responsible for the reduction of the metallic cations.

### 2.1.4.1 Electroless deposition

The electroless deposition of metals can be defined as the controlled autocatalytic reduction of a dissolved metal ion by a dissolved reducing agent (internal electron source) at a substrate surface to give a uniform coherent film. In addition to the source of metal ions and the reducing agent, the electroless bath includes also complexing agents (preventing the excess of free cations), reaction accelerators, bath stabilisers and pH regulators and buffers. The electrochemical nature of the deposition process can be represented, in most cases, by the following coupled reaction:



where the reductant (Red) of positive charge  $y$  becomes oxidised, while the  $z$ -valent metal (Me) ion is reduced [22]. This method allows uniformly coating both conducting and insulating substrates, independently of their shape.

In context of industrial applications, electroless deposition is practically synonym of electroless Ni. This is indisputably the type of coating mostly produced by this method, mainly due to its uniform thickness, good mechanical properties and high wear and corrosion resistance. Three types of films can be here distinguished: pure Ni, Ni alloys (mainly Ni-P and Ni-B) and Ni-matrix composites (mostly Ni alloys reinforced with ceramic particles, such as  $\text{Al}_2\text{O}_3$ ,  $\text{ZrO}_2$  and SiC) [23,24]. The alloys and composites are produced by the co-deposition of the alloying element or reinforcement during the reduction of Ni ions. Ni can be deposited from both alkaline and acidic baths, normally using Ni acetate ( $\text{C}_4\text{H}_6\text{NiO}_4$ ) as metal source for pure-Ni films, while Ni sulfate ( $\text{NiSO}_4$ ) and Ni chloride ( $\text{NiCl}_2$ ) in the case of alloys and composites. As for the reducing agent, hydrazine ( $\text{N}_2\text{H}_4$ ) is majorly employed for producing pure Ni (99%); Na hypophosphite ( $\text{NaPO}_2\text{H}_2$ ) for Ni-P alloys; and Na borohydride ( $\text{NaBH}_4$ ) and dimethylamine borane ( $\text{C}_2\text{H}_{10}\text{BN}$ ) for Ni-B alloys [24].

### 2.1.4.2 Electrodeposition

This method involves conducting an electric current through two electrodes which are submerged in an electrolyte solution containing ions of the metal to be deposited. The negatively charged electrode (cathode) is given by the substrate/structure to be coated, whose surface must be therefore electrically conductive (as opposed to the electroless technique).

The positively charged electrode (anode) can be made either from an inert conductive material (e.g., Pt, Ti and C) or from the same metal as the deposit. In the latter case, it gradually dissolves and thus replenishes the ions in the electrolyte as they are consumed during the deposition, keeping its concentration constant. A direct-current power supply (external electron source) is connected to the electrodes, closing the electrical circuit. Then, metal ions who reach the cathode's surface are reduced, building up the film. The basic configuration is displayed in Fig. 2.3. Three mechanisms are involved in the mass transport in the electrolyte: convection, either natural (due to concentration gradients) or forced (e.g., agitation and air blowing); diffusion, which takes place in the cathode-electrolyte interface, where convection is not possible due to hydrodynamic friction; and migration under the influence of the electric field. The latter is not relevant in the practice, being this process governed by convection and diffusion [25].

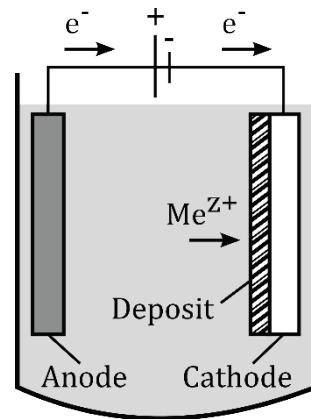


**Fig. 2.3** Basic representation of an electrodeposition cell, indicating its essential components.

Electrodeposition has a major presence in industrial applications given its low cost, fast deposition rates, great adaptability to complex shapes and the high purity of the resulting deposits, just to name some of its benefits. Its use for electroforming is especially relevant, which consists in the manufacture of metal parts by using a mandrel or mould as substrate which is subsequently separated from the deposit [26]. Not only pure metals can be produced by electrodeposition, but also alloys, metal matrix composites and multi-layered systems. As in the electroless method, this is achieved by the co-deposition of the secondary constituent, which is dissolved or dispersed in the electrolyte [22].

Another key application of electrodeposition is the fabrication of ultrafine-grained and nanocrystalline films and coatings, due to their superb mechanical properties [27,28]. Three

combinable approaches are normally employed to achieve this, which operate by regulating the two competing processes which govern the film development, namely crystallite nucleation and growth. The first and most relevant approach is the use of pulsed current, which allows considerably increasing the voltage and current density applied [29]. This results in a high nucleation rate and smaller crystallite size. Moreover, by reducing the duration of the pulses, surface diffusion is limited, preventing the coarsening of the microstructure [30]. The second alternative is the addition of organic additives in the bath (e.g., saccharin and citric acid), which block active sites of the electrode surface by adsorbing onto them. This inhibits crystallite growth and interferes with surface diffusion, thus favouring nucleation [31]. Lastly, alloying elements or secondary phases in metal matrix composites can be used to exert pinning or drag forces on migrating grain boundaries of the deposits, while also acting as nucleation sites, resulting in finer microstructures [32].

Two types of electrolytes are mostly used for depositing Ni, namely the Watts and sulfamate baths. The majority of Ni electrodeposition solutions (particularly those for decorative purposes) are based on the former, while the latter is mainly employed for depositing functional coatings and electroforming, where its superior performance (low stress and enhanced properties of the deposits; higher deposition rate) is required and thus its higher costs are justified [33]. The typical basic compositions of these electrolytes are listed in Table 2.1. Moreover, several types of additives can be incorporated to the bath in order to modify the resulting characteristics of the deposits. Examples of these are brighteners, levelling agents, surfactants, grain refiners, stress relievers and texture inducers. Besides pure Ni, a wide variety of its alloys can be obtained by means of electrodeposition. Ni binary and ternary systems containing the alloying elements Co, Fe, Sn, Mo, W, P, Mn, Cr, In and Cu can be found among those who had been produced on a significant commercial scale [34].

### **2.1.5 Cladding deposition**

The general term cladding describes a series of coating methods by which a pure metal, alloy or composite (the cladding material) is bonded electrically, mechanically or through some other high pressure and temperature process onto another dissimilar metal (the substrate), in order to enhance its durability, strength or appearance. Among these, the laser cladding technique is of special interest due to its outstanding performance with respect to other thick-coating processes. Its highly accurate energy and material delivery allows avoiding the degradation of the substrate and the dilution of the coating in it, which are vital for

achieving superb adherence and to meet the strict composition requirements of complex and expensive hardfacing materials, respectively [35,36].

**Table 2.1** Basic compositions of the most relevant types of electrolytes used for the electro-deposition of Ni, namely the Watts and Ni-sulfamate solutions [33].

	Watts bath	Ni-sulfamate bath
Ni sulfate - NiSO <sub>4</sub> .6H <sub>2</sub> O	240 - 300 g/l	–
Ni sulfamate - Ni(SO <sub>3</sub> NH <sub>2</sub> ) <sub>2</sub> .4H <sub>2</sub> O	–	300 - 450 g/l
Ni chloride - NiCl <sub>2</sub> .6H <sub>2</sub> O	30 - 90 g/l	≤ 30 g/l
Boric acid - H <sub>3</sub> BO <sub>3</sub>	30 - 45 g/l	30 g/l
Distilled H <sub>2</sub> O	Balance	Balance
Temperature	40 - 60 °C	40 - 60 °C
pH	3.5 - 4.5	3.5 - 4.5
Current density	2 - 7 A/dm <sup>2</sup>	2 - 15 A/dm <sup>2</sup>
Deposition rate	25 - 85 μm/h	25 - 180 μm/h

In the laser cladding method, a laser beam scans the surface to be coated while melting locally the cladding material (usually in form of powder, foil or wire) and a thin layer from the substrate's surface. A fast cooling takes place after the passing of the beam due to the heat transfer to the bulk, initiating the solidification of the coating at the bottom of the melted region, progressing rapidly towards the surface (Fig. 2.4). This results in thick coatings (50 μm to 2 mm) free of porosity and cracks. The high solidification rates lead to the formation of fine microstructures, sometimes containing non-equilibrium phases and supersaturated solid solutions, which may result in interesting and potentially useful properties [35].

Ni-based alloys and composites are among the most commonly applied materials by laser cladding [37]. Hardfacing Ni alloys are of special commercial interest, owing to their low cost and superb resistance against abrasion, corrosion and high temperature [38]. These usually incorporate several alloying elements (e.g., C, Cr, Si, B, Co, Fe and W), allowing for a wide range of compositions.

In addition to laser-based techniques, cladding methods include the use of flame, plasma and electric arcs as energy source for the melting of the coating material. Roll bonding (with or without heating) falls also in this category, making use of high pressures for adhering the coating to the substrate.

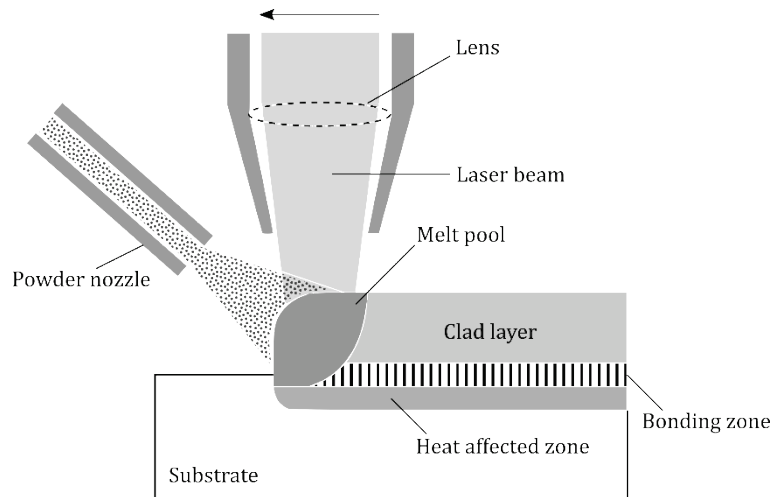


**Fig. 2.4** Schematic of metallic-coating deposition by laser cladding.

### 2.1.6 Thermal spraying

Thermal spraying comprises a family of processes in which the coating precursor (feedstock) is heated and accelerated towards a substrate in order to produce coatings with thickness of up to several millimetres. The feedstock material is typically found in the form of powder or wire, but also solutions and dispersion are used for producing sub-micrometre and nanostructured coatings [39,40]. Its heating is most commonly done with a combustion flame, plasma or electric arc. The resulting molten droplets and remaining solid particles are then propelled in a gas stream towards the targeted surface [41]. Coatings produced by thermal spraying include pure metals, alloys, ceramics, composites and plastics, presenting usually a lamellar microstructure which results from the nature of their sintering and solidification process [42].

Ni-based coatings are readily produced by high velocity oxy-fuel thermal spraying, which is a versatile route for applying adherent, homogeneous coatings with low porosity and oxide content, mostly for protecting critical components used in high temperature, corrosive and erosive environments [43]. Common examples of such coatings are those made from nanocrystalline Ni [44], commercial Ni alloys [45] and intermetallic compounds, such as NiAl [43].

## 2.2 Ni and its application in coating materials

Ni is the fifth most common element on the planet, being extensively present in the Earth's crust. It belongs to the transition metals and is characterised by a relatively high melting

point, ductile behaviour, good resistance against corrosion and oxidation and remarkable propensity towards alloying (a diverse selection of its properties is listed in Table 2.2). These aspects make Ni certainly appealing for a large variety of industries and applications which include, but are not limited, to transportation (aerospace and automotive), the food industry, medical devices, electronics, metal processing equipment and structural materials.

**Table 2.2** Characteristic physical and mechanical properties of Ni [5].

Atomic number	28
Crystal structure	face-centred cubic
Density	8.902 g/cm <sup>3</sup> (at 25 °C)
Melting point	1453 °C
Thermal expansion	13.3 µm/m · K (at 0 to 100 °C)
Thermal conductivity	82.9 W/m · K (at 100 °C)
Electrical resistivity	68.44 nW · m (at 20 °C)
Magnetic ordering	ferromagnetic
Curie temperature	358 °C
Young's modulus	207 GPa
Shear modulus	76 GPa

The current use of Ni is primarily directed to the manufacture of stainless steels, consuming about 65% of its annual production [5]. Secondly, Ni is applied as base element for countless heat, corrosion and wear resistant materials. Here, a special mention should be made for Fe-Ni and Ni-base superalloys (e.g., Ni-Ti/Al), which display an exceptional combination of high-temperature strength, toughness and resistance to corrosive or oxidising environments [46]. Other applications of Ni materials which involve some unique physical properties include low expansion alloys (e.g., Fe-36% Ni, also known as Invar), which exhibit anomalously low (almost zero) and/or uniform thermal expansion over a wide temperature range [47]; resistance alloys (e.g., Ni-Cr-Al/Fe/Si), displaying uniform and stable electrical resistivity [48]; soft magnetic alloys (such as several Ni-Fe systems), with high initial permeability coupled to low saturation induction [49]; and shape memory alloys (mainly Ti-Ni intermetallics), which possess the ability to return to certain previously defined shape or size upon proper heating (high strength, ductility and pseudoelasticity are common traits of these materials) [50,51].

A special mention deserves the use of Ni-based materials for coating applications, which is of great technological and commercial importance. Not only stands Ni as the most electroplated metal, but also about 10% of its annual production is achieved in this way [5]. Several examples from a variety of engineering applications of Ni coatings are displayed in Fig. 2.5. The characteristics and significant features of several commercially relevant Ni-based coating materials are summarised in the following sections, with the focus set on those produced by means of electrochemical methods. These techniques attract the foremost scientific and commercial interest and are closely related to the work presented in this doctoral thesis.

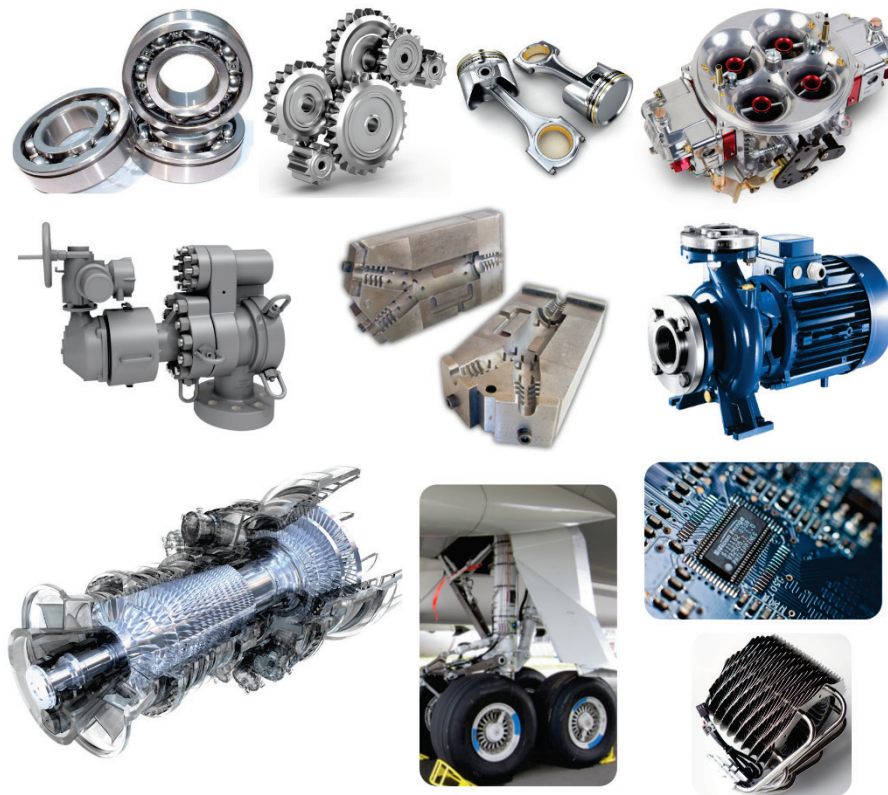


**Fig. 2.5** Exemplary engineering applications where Ni-based coatings are readily used, namely: bearings, gears, pistons, carburetors, control valves, moulds, water pumps, gas-turbine compressors, landing gears, printed circuit boards and heatsinks.

### 2.2.1 Pure-Ni coatings for decorative and engineering applications

Single-phase, non-alloyed Ni coatings are most widely produced by electrodeposition for their use in decorative applications. Bright-Ni deposits are normally obtained by using variations of the Watts bath presented in Table 2.1, including several additives (mostly organic ones) such as brightening and levelling agents. This allows obtaining either highly lustrous

or satin coatings, with good ductility and levelling properties. In order to avoid the tarnishing of Ni over time from the exposure to ambient conditions, a layer of Cr is usually deposited on top of it, which passivates the surface by forming a thin oxide film.

In those cases where besides an attractive appearance, a long-time corrosion resistance is required, the use of multi-layered Ni is common practice. Because of the addition of organic species in the bath, the bright-Ni deposits possess certain amounts of sulfur, which deteriorate its corrosion resistance. For dealing with this problem, a relatively thick coating of semi-bright Ni is applied between the substrate and the bright layer, using sulfur-free organic additives [33]. The semi-bright Ni is electrochemically noble with respect to the bright layer (i.e., it has a less negative corrosion potential). Consequently, when the attack reaches the interface, the bright Ni is preferentially corroded laterally, which delays the penetration of the semi-bright layer. As already mentioned, it is also frequent to apply a passivating Cr film on top of the Ni layers. A simple Cr finish would normally exhibit some porosity and cracks. In contact with relatively small regions of Ni, these defects would act as large-area corrosion cells, leading to rapid pit penetration. This issue is solved by introducing a high and controlled degree of micro-porosity or micro-cracking by controlling the plating parameters. This results in an increased exposure area of Ni, thus reducing the corrosion current density and, with it, the size of individual pits (see Fig. 2.6).

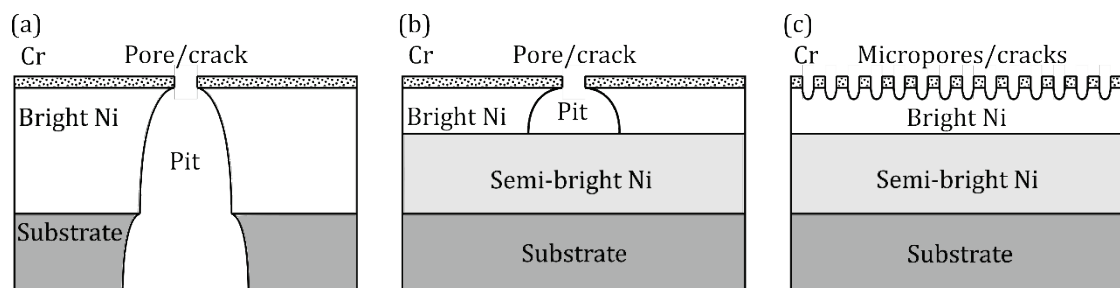


**Fig. 2.6** Corrosion pitting on (a) single-layer Ni plus Cr; (b) dual-layer Ni plus Cr; and (c) dual-layer Ni plus micro-discontinuous Cr (adapted from [33]).

Ni coatings for engineering applications are mostly deposited from Watts baths due to their low cost. Ni-sulfamate solutions are also very popular, since they induce rather low internal stresses. A variety of other electrolytes are also available, but their use is limited to specific engineering applications [5]. Since normally in those cases a fully-bright appearance is not needed, matte, sulfur-free deposits are applied. These Ni coatings are mostly used for corrosion and wear protection. Regarding the latter, there is a large body of recent and ongoing

research concerning the analysis of electrodeposited (mainly by pulsed plating) nanocrystalline Ni films, whose superb mechanical properties are directly responsible for their enhanced tribological performance [7,8,52,53].

### **2.2.2 Ni-alloy films and coatings produced by electrodeposition**

As stated earlier in this chapter, Ni can be co-deposited with a wide variety of other metals by means of the electrodeposition technique. While most of these alloys aroused interest only at the academic level, there are also several which succeeded in providing solutions for large-scale as well as niche technical applications. Some of the latter are presented next.

Electrodeposited Ni-Fe alloy coatings have been produced already for decades in a wide range of compositions, mostly for decorative applications. Their development was motivated firstly by the Ni shortage of 1970 and later by its increasing price, in an attempt to conserve Ni and reduce anode material costs by partially substituting Ni with Fe. They present full brightness, high levelling and ductility and are very receptive to a Cr overlay [34]. However, with increasing Fe content ( $> 15$  wt%), their use is limited to indoor applications, since the corrosion resistance is considerably reduced [5]. Though Ni and Fe display complete solubility, structural ordering is found at about 25 or 75 at% Fe ( $\text{Ni}_3\text{Fe}$  and  $\text{NiFe}_3$ , respectively). Moreover, Ni-rich alloys present face-centred cubic (FCC) crystal structure, while body-centred cubic (BCC) configuration is observed for Fe-rich ones [54]. Ni-Fe alloys have also gained interest in engineering applications as soft-magnetic coatings, being used in recording devices, magnetic microactuators and inductors, for instance [55]. Among them, Permalloy (19 wt% Fe) is probably the most known commercial alternative [56].

Ni-Co coatings awoke interest for engineering applications, since Co increases the hardness and strength of Ni electrodeposits. The mechanical properties of Ni-Co improve gradually with increasing Co content of up to 50 wt%, point at which they start to decline with further addition of the alloying element [57,58]. An enhanced wear resistance and reduced friction coefficient are also features of these coatings, which have been attributed to the hexagonal close-packed (HCP) lattice structure which progressively develops with the addition of Co. With up to 50 wt% Co, the coatings remain FCC. Then, and up to 80 wt%, a mixed FCC/HCP structure is observed, changing to pure HCP from there onwards [58]. Moreover, Ni-Co is actively co-deposited with a variety of reinforcing particles (such as SiC,  $\text{MoS}_2$  or C nanotubes), forming nanocomposite coatings with furtherly improved tribological properties

[59–61]. Because of its hard-magnetic nature, electrodeposited Ni-Co has been readily studied for its application in electromagnetic devices, with the focus on microsystem technologies for the fabrication of sensors, actuators, micro-relays and inductors [57,58]. In addition, films of these alloys constitute active materials for the H<sub>2</sub> and O<sub>2</sub>-evolution reactions in the water electrolysis [62].

Ni-Mn electrodeposits containing low amounts of Mn (< 0.5 wt%) allow the use of sulfur-containing additives in the bath (such as grain refiners or stress reducers), avoiding the associated embrittlement observed in the case of pure Ni (upon heating above 200 °C) [5]. Moreover, as-deposited Ni-Mn coatings exhibit higher strength, hardness and thermal stability. They are able to retain texture, fine-grained morphology and strength up to about 600 °C, while for pure Ni, the limit lays below 300 °C [63]. Moreover, research performed on their magnetic properties demonstrated that Ni-Mn electrodeposits exhibit enhanced coercivity and remanence [64,65]. Such characteristics allow this type of alloys to meet the requirements of several applications involving components of micromechanical systems [66].

Ni-Mo alloy coatings exhibit a high hardness; remarkable corrosion resistance in highly corrosive media; and nanocrystalline structure, which becomes finer with increasing Mo content. The hardness increases in parallel with the alloying-element content, reaching its maximum for compositions with about 17 to 19 wt% Mo [67,68]. Further alloying produces such a fine microstructure, that softening due to breakdown of the Hall-Petch effect takes place. A similar behaviour is observed for the corrosion resistance. On one hand, it increases with Mo content. However, the larger fraction of intercrystalline regions (which result from grain refinement) yields the opposite effect. Then, the optimal corrosion resistance was observed for alloys with 15 to 30 wt% Mo [67]. Another interesting feature of Ni-Mo alloys are their good electrocatalytic properties for the H<sub>2</sub>-evolution reaction [69,70].

### **2.2.3 Electroless Ni-alloy coatings**

The industrial relevance of electroless Ni coatings is almost entirely given by Ni-P and Ni-B alloys, with the former having about a 90% share of the commercial application [24]. These are briefly reviewed next.

### **2.2.3.1 Ni-P alloys**

Ni-P coatings are produced by means of the electroless technique, mostly from acidic baths containing hypophosphite ions (reducing agent) [23]. The microstructure of the deposits consists of a mixture of nanocrystalline and amorphous phases at low P contents (< 5 wt%), becoming completely amorphous for higher amounts of the alloying element [71]. High-P (> 10 wt%) coatings are normally employed for engineering applications due to their superior mechanical strength with limited, but decent, ductility. They present hardness ranging from 500 to 700 HV<sub>0.1</sub> in their as-deposited state, which can be increased up to about 1100 HV<sub>0.1</sub> (comparable to hard Cr) after annealing for 1 h at 400 °C [72,73]. This results in a superb resistance to wear, for which such coatings are readily applied [74].

Due to their amorphous nature and passivity, Ni-P coatings provide also outstanding corrosion resistance, even superior to that of pure Ni and Cr, depending on the environment. This has been attributed to the absence of crystalline defects and their chemically-homogeneous single-phase nature. Other interesting features of this material include inherent lubricity, high solderability and excellent thickness uniformity of the deposits.

### **2.2.3.2 Ni-B alloys**

Ni-B alloys are of special interest in highly-severe tribological applications and share similar characteristics with the Ni-P system. Their electroless deposition is most frequently carried out using borohydride as reducing agent, resulting in B contents of 3 to 6 wt% for the majority of commercial coatings. The fraction of amorphous phase grows with the amount of B, but a mixed structure containing crystalline Ni always remains (unlike in Ni-P) [75]. The major advantage of Ni-B against Ni-P is its higher hardness, which assumes values between 650 and 750 HV<sub>100</sub> in the as-deposited state, reaching up to about 1200 HV<sub>100</sub> after short annealing [76]. Two hardness peaks are found which correspond with annealing at about 350 and 450 °C, as a result of the precipitation hardening given by the transformation of the amorphous phase to crystalline Ni and Ni borides (Ni<sub>2</sub>B and Ni<sub>3</sub>B) [77]. On the other hand, its tensile strength and ductility are only about one fifth of those of Ni-P. Moreover, in certain media such as acids and ammonia solutions, Ni-B presents much worse corrosion resistance [5,24].

### **2.2.3.3 Polyalloy and composite coatings based on Ni-P and Ni-B**

These ternary and quaternary systems find application where very specific properties are required, performing higher than conventional Ni-P and Ni-B coatings. Their distinctive attributes may include enhanced chemical and high-temperature resistance, superior mechanical and tribological properties and specific electrical and magnetic characteristics.

Ni-Cu-P coatings stand out because of their improved thermal and non-magnetic stability, superior corrosion resistance (especially in marine atmosphere) and solderability [78–80]. The amount of Cu in the alloy is highly variable (even above 60 wt%), which is controlled by the concentration of the copper salt ( $\text{CuSO}_4$ ) in the electroless bath and its pH. The critical P content for the transition between amorphous and crystalline structures was found to be 7 wt% [81].

Ni-Co-P films gained interest because of their magnetic properties, finding application as thin magnetic-recording media and for electromagnetic shielding. Said properties are strongly dependent on the microstructure (which is in turn directly related to the amount of Co) and thickness of the deposits [82]. Amorphous Ni-Co-P presents soft-magnetic behaviour, which is the case for Co contents of up to about 8 wt% [83]. From that point onwards, a mix-crystalline structure develops, which is accompanied by an increase in saturation magnetisation, remanence and coercivity (magnetic hardening) [84]. On the other hand, the corrosion resistance is reduced. Electroless Ni-Fe-P is another related alloy coating which gained relevance due to its soft-magnetic properties [85].

Ni-W-P coatings are normally produced with W contents ranging between 3 and 15 wt%. They exhibit higher thermal stability than the binary alloy Ni-P and also increased hardness, both in the as-deposited and annealed states, which results in a superior wear resistance [74]. It was demonstrated that, unlike Ni-P, Ni-W-P does not completely recrystallize even after several thermal cycles, avoiding the degradation of its mechanical properties [86]. Another interesting characteristic of this material relates to its corrosion behaviour: unlike with most Ni-based metallic glasses, crystalline Ni-W-P exhibits higher resistance than its amorphous counterpart. This was attributed to the formation of a dense W-oxide film on the surface during annealing [87].

Electroless Ni-Tl-B alloy coatings have been found to perform especially well in applications exposed to fretting wear [88,89]. The same can be said for Ni-Sn-B [5], which has also been investigated for its appealing corrosion resistance and solderability [90,91].

Being different in nature from the systems described so far, electroless composite coatings deserve a special mention. Consisting of fine particles dispersed in a Ni-P matrix (most frequently below 30 wt%), they are aimed to provide enhanced mechanical properties and tribological behaviour. The hardness and wear resistance can be increased by the incorporation of hard particles (mostly SiC, but also TiO<sub>2</sub> or diamond, for instance) [92,93]. Soft particles (e.g., polytetrafluoroethylene, MoS<sub>2</sub> or graphite) are used in unlubricated conditions to reduce the friction coefficient of the matrix, at the expense of losing hardness, due to their ability to prevent adhesion between the mating surfaces [94,95]. Both types of reinforcements can be combined in order to obtain a well-balanced mix of their attributes [94]. Normally, the corrosion resistance of the composites is worse than that of Ni-P, but exceptions to that rule can be found for some specific combinations of materials and corroding media [93]. Several factors may affect the incorporation of the particles into the coating during their co-deposition with the matrix, which may lead to agglomeration and poor resulting properties. Among them, especially important are the particle size, shape and concentration; orientation of the target substrate; agitation of the electroless bath; and the use of additives [96]. It was observed that in the case of some commonly-used reinforcing materials, such as TiO<sub>2</sub>, the microstructure of the Ni-P matrix presented no difference with respect to that of the pure alloy [97]. Moreover, the crystallization energy and temperature did not vary significantly.

### **2.3 Electrical contact materials and applications**

Electrical contacts initiate, sustain and interrupt the flow of current in an electrical circuit. They do so by controlling the physical contact between electrodes which connect current-carrying members of electrical and electronic devices. At the interface, the nature of this contact is determined by interfacial transport processes, rates of heat generation and dissipation, mechanical stresses, material phase transformations and migration effects due to transient phenomena.

Electrical contacts can be either stationary or moving. As implied by their name, stationary contacts form a permanent joint, rigid or elastic, commonly secured by welding, soldering or clamping. These are usually found in many types of power connections [1,98]. In the case of moving contacts, the contacting partners can either separate completely or partially slide over each other. Separable contacts are mostly used at circuit breakers, plug connectors, switches, contactors and relays [99–101], while sliding contacts are very important components in many automatic, telemechanical and communication devices [102–104].

During operation, electrical contacts might be exposed to a broad variety of degrading phenomena, which can originate from mechanical, chemical, thermal and electrical interactions. Therefore, the selection of appropriate electrode materials plays a key role for ensuring the good performance and durability of the device. Accordingly, depending on the operating conditions, electrical contact materials are required to display several technical features, such as high conductivity (both electrical and thermal), low and stable contact resistance, good tribomechanical properties, thermal stability and high resistance against corrosion, welding and electrical-arc erosion.

### **2.3.1 Overview of electrical contact materials**

Cu and Al are the most widely used metals in electrical contact applications, due to their outstanding electrical and thermal conductivities as well as for their high availability and relative low cost. They are mostly used for heavy-current contact applications, usually in the form of alloys with enhanced mechanical and tribological properties. Bronzes (Cu-Sn), brasses (Cu-Zn) and Al-Mg alloys are some of the most common examples of this [105,106].

Noble metals are mostly applied in low-current electrical-contact devices, mainly alloyed but also as pure-metal coatings. For such applications which sustain low contact pressures, a both low and stable contact resistivity is required. Due to its superior tarnishing and oxidation resistance, Au is readily used in computers and telecommunication devices. It is generally alloyed with Cu, Ag, Pd, Pt and Ni, for instance, forming binary and ternary systems with enhanced mechanical properties [107]. Pt also presents excellent tarnishing, corrosion and oxidation resistance, however, it must be alloyed with Ir, Ru or Rh for its use due to its low hardness [1]. Even though Pd is not as resistant as Pt against corrosion and oxidation, it is regarded as a candidate contact-material replacement for Au in circuit boards and other applications due to its relative low cost [108].

With the highest electrical conductivity of all metals, Ag is the most used material in a broad variety of electrical-contact devices operating at low to medium-high currents (up to about 1000 A) [109]. While Cu is the best alloying element for improving its strength and wear behaviour, Pt, Pd and Au provide resistance against tarnishing together with a considerable increase in hardness [1,110]. Moreover, Ag-matrix composites reinforced with graphite, Ni or metal oxides (e.g., CdO, ZnO or SnO<sub>2</sub>) are the materials of choice for applications where the electrical-arc erosion and welding resistance are critical, such as switches, relays, contactors and even circuit breakers [111–113].

Finally, Ni is largely used in the electrical contacts industry, mostly as coating for Cu and Al power connectors. It extends their working life by reducing and stabilising their contact resistance [114,115]. Moreover, it is well-known that Ni coatings show a good behaviour in certain corrosive atmospheres, mainly because of their propensity to form a thin passivating film [6]. Another use of Ni is as diffusion barrier between Cu and Au in many electronic applications [116,117].

## 2.4 The Ni-Ag system

Ag is a soft transition metal, possessing the highest electrical and thermal conductivities of all the elements in the periodic table. Some of its characteristic properties are listed in Table 2.3. Due to the large difference in their atomic radius (about 15%) and highly positive enthalpy of mixing ( $> 15$  kJ/mol [118]), Ag presents virtually no mutual solid solubility with Ni [9]. This can be clearly appreciated in the phase diagram of Fig. 2.7. The maximum solubility of Ni in Ag is about 0.2 at% at 960 °C and that of Ag in Ni about 1 at%, close to the monotectic temperature of 1435 °C. However, by processing Ag and Ni in the nanoscale, it is possible to increase their miscibility and produce Ni-Ag solid solutions otherwise unobtainable. This is feasible due to the increased energetic contribution of surfaces, which significantly modify the attributes related to the thermodynamic stability of the phases [119]. Such approach includes the mechanical alloying and hot pressing of nanopowders, resulting in bulk nanocrystalline structures [118,120], and the synthesis of Ag-Ni nanoparticles by electrodeposition [119,121] or PVD [122], for instance.

**Table 2.3** Characteristic physical and mechanical properties of Ag [48,123].

Atomic number	47
Crystal structure	face-centred cubic
Density	10.49 g/cm <sup>3</sup> (at 20 °C)
Melting point	961.9 °C
Thermal expansion	19.0 $\mu\text{m}/\text{m} \cdot \text{K}$ (at 20 °C)
Thermal conductivity	428 W/m $\cdot$ K (at 20 °C)
Electrical resistivity	14.7 nW $\cdot$ m (at 0 °C)
Young's modulus	82.7 GPa
Shear modulus	30.3 GPa

Rather than in form of alloys, Ni-Ag systems find application or are subject of research mostly in form of composite structures of varied morphologies, thus conserving the individual Ni and Ag phases. For instance, Ni-Ag core-shell nanostructures (nanoparticles and nanowires) have been investigated for their potential application in the optical, magnetic, catalytic, biochemical and biomedical fields [124–126]. Also, Ni/Ag bilayers attract interest as ohmic contacts for p-type, GaN-based materials due to their low contact resistance. This is especially relevant for light-emitting and laser diodes as well as for ultraviolet photodetectors [127–129]. Finally, probably the most important use of Ni-Ag corresponds to electrical contact materials consisting of dispersed Ni within a Ag matrix. Their composition can reach up to 40 wt% Ni, ranging normally between 10 and 20 wt% [109]. Such composites are largely applied for motor-starting contacts and also in relays and switches, being suitable both for sliding and make-brake operation [5]. They are best suited to perform in low voltage, either with direct or alternate current of up to 100 A [1,109].

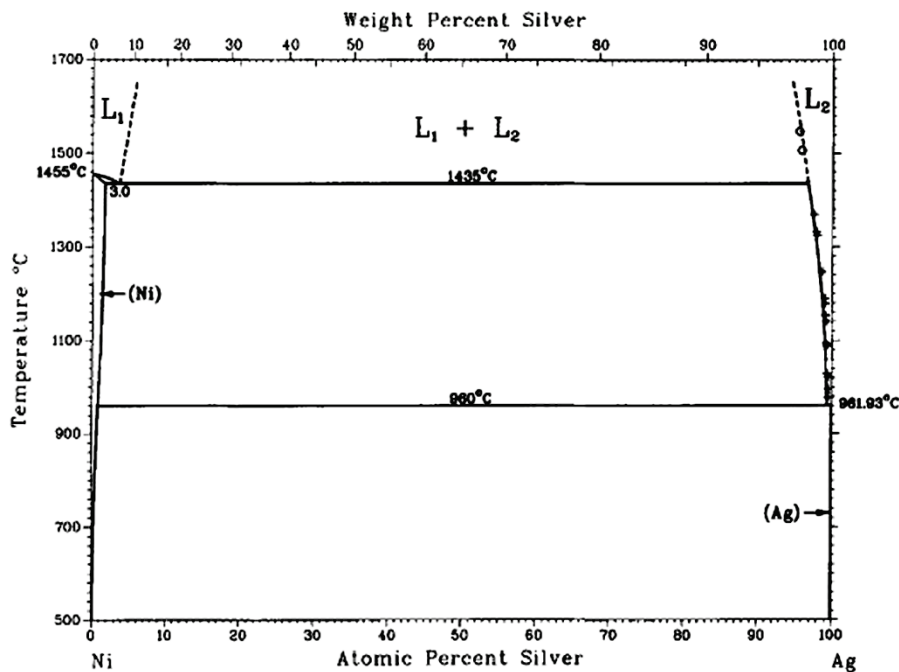


**Fig. 2.7** Phase diagram of the Ni-Ag system showing virtually no mutual solid solubility (reproduced from [9]).

## 2.5 The science of SnO<sub>2</sub>

Pure SnO<sub>2</sub> is an n-type, wide-band-gap semiconductor. Due to its interesting physical properties, it has been adopted for its use in several applications, mainly as transparent conducting oxide, oxidation catalyst and solid-state gas-sensing material. Some of its basic attributes are listed in Table 2.4.

A low electrical resistivity coupled with high transparency to visible light makes SnO<sub>2</sub> suitable as electrode material for solar cells, light-emitting diodes, flat-panel displays and field-effect transistors, among other applications. Being stoichiometric SnO<sub>2</sub> an insulator, the electrical conductivity is attributed to the existence of native defects, namely oxygen vacancies and Sn interstitials [130]. Since their energy of formation is very low, said defects develop readily, promoting the formation of shallow electron-donor centres. Moreover, SnO<sub>2</sub> was found to display much higher, metallic-like conductivity when doped with Sb [131,132].

**Table 2.4** Characteristic physical properties of SnO<sub>2</sub> [133].

Crystal structure	tetragonal, rutile
Density	6.99 g/cm <sup>3</sup>
Band gap	3.6 eV
Melting point	> 1900 °C
Thermal expansion	3.7 - 4.0 μm/m · K (at 20 °C)
Common extrinsic n-type dopants	Sb, F, Cl

Regarding its catalytic behaviour, SnO<sub>2</sub> exhibits good activity towards the reactions of CO with O<sub>2</sub> and NO [133]. Due to the two possible oxidation states of Sn (+2 and +4), SnO<sub>2</sub> gives up readily lattice-oxygen atoms for the oxidation of adsorbed molecules, which are subsequently restored by the O<sub>2</sub> present in the air.

Lastly, the gas sensing properties exhibited by SnO<sub>2</sub> are given by the change in its electrical resistivity when exposed to different partial pressures of certain gases. These adsorb on the oxide surface, bending its band gap due to their electric charge and reducing the amount of available charge carriers by capturing electrons [134,135]. Additives forming dispersed clusters over the surface of SnO<sub>2</sub> can be used to increase the sensitivity towards particular gases.

Most of the attractive properties of SnO<sub>2</sub> discussed so far are largely governed by surface-related phenomena. This has motivated the research and development of one-dimensional nanostructures (e.g., nanowires, rods and belts), which have shown superior performance in many applications as a consequence of their large surface-to-volume ratio [136,137]. Among them, SnO<sub>2</sub> nanowires present likely the largest body of literature and are directly related to the present doctoral thesis as a fundamental component of the composite film under study. Some of their possible configurations are displayed in Fig. 2.8.

As a final remark, the use of SnO<sub>2</sub> in electrical contact materials deserves a special mention. Ag-matrix composites with 8 to 20 wt% SnO<sub>2</sub> (in the form of particles or fibres) are widely used for their superb resistance against welding [2–4]. They were originally developed for replacing the hazardous Ag-CdO and are commonly found in switches, relays, circuit breakers and contactors, for both domestic and industrial use.

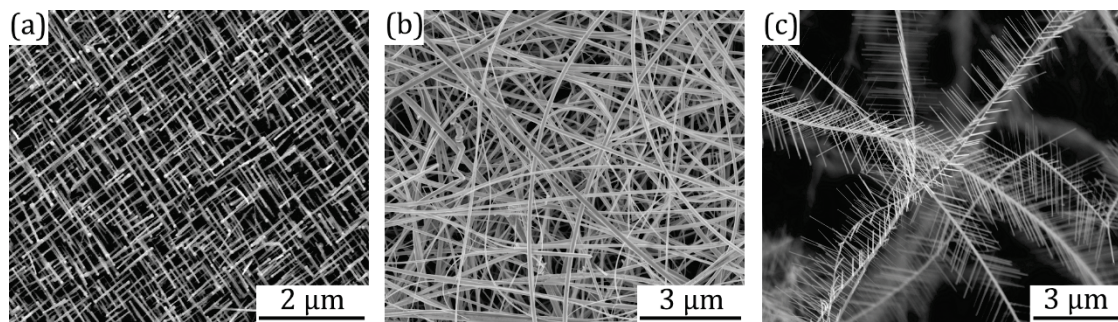


**Fig. 2.8** Top view of SnO<sub>2</sub>-nanowire arrays of different morphology: (a) ordered array of short nanowires which sustained epitaxial growth; (b) disordered network of long nanowires; and (c) hierarchical nanowire structures obtained by secondary growth onto primary nanowires.

## 3 Materials and methods

### 3.1 Fabrication procedure of Ni-Ag-SnO<sub>2</sub> composite films

The composite films which were subject of study in this work consisted of Ag-coated SnO<sub>2</sub> nanowires within a Ni matrix (Ni-Ag-SnO<sub>2</sub>). Their fabrication method involved a sequence of processes which are described next.

#### 3.1.1 Synthesis of SnO<sub>2</sub> nanowires

Single-crystalline SnO<sub>2</sub> nanowires were produced by CVD in a low-pressure, cold-wall reactor, following the vapour-liquid-solid (VLS) growth mechanism [138]. In this process, a molecular precursor is decomposed on a heated surface, where metallic catalyst particles act as nucleation sites dictating one-dimensional crystal growth; this is schematised in Fig. 3.1a. AISI316L stainless-steel sheets (of about 1 cm<sup>2</sup>) were used as substrates, being previously decorated with sputtered Au nanoparticles (catalysts for one-dimensional VLS growth).

The temperature of the source containing the Sn(O<sup>t</sup>Bu)<sub>4</sub> precursor was maintained at 27°C. This was then introduced into the reactor by applying a dynamic vacuum ( $5 \times 10^{-3}$  mbar) and the deposition took place for 15 min at 750 °C. This resulted in disordered arrays of high-aspect-ratio nanowires (as displayed in Fig. 3.1b), possessing about 100 nm diameter and several μm length.

#### 3.1.2 Electroless Ag deposition onto SnO<sub>2</sub> nanowires

Ag was deposited onto the SnO<sub>2</sub> nanowires by means of the electroless method. Previously, the samples were sensitised and activated in a two-step process using Sn and Ag, respectively [139]. This procedure was meant to increase the hydrophilicity of the nanowire array and to provide a high density of uniformly distributed catalytic sites for the electroless reaction, thus resulting in a smooth and continuous film morphology [140–142]. The electroless bath used was a modified version of the approach found in [143]. Here, Ag nitrate (AgNO<sub>3</sub>) was used as Ag-ion source, ammonia (NH<sub>3</sub>) and ethylenediamine (C<sub>2</sub>H<sub>8</sub>N<sub>2</sub>) as complexing agents and D-glucose (C<sub>6</sub>H<sub>12</sub>O<sub>6</sub>) as reducing agent. The compositions of all the involved solutions are listed in Table 3.1.

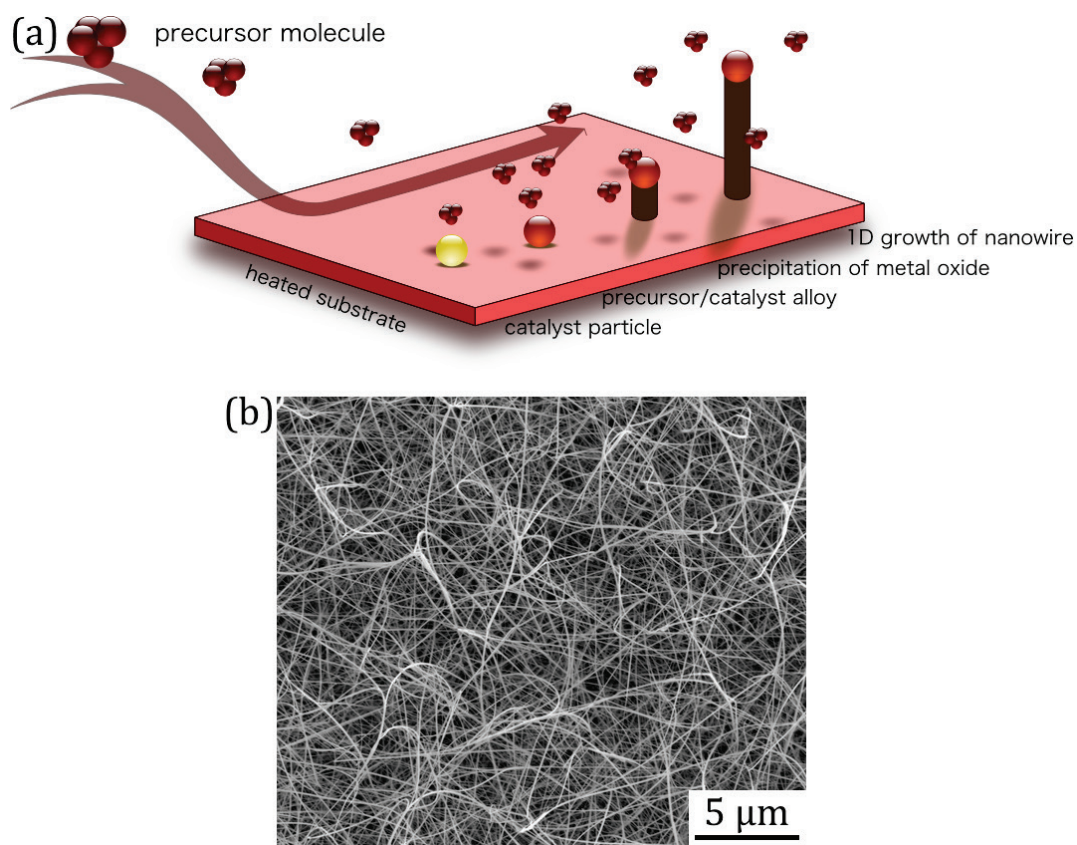


**Fig. 3.1** (a) Schematic representation of VLS nanowire growth and (b) disordered network of long  $\text{SnO}_2$  nanowires.

**Table 3.1** Compositions of the pretreatment solutions and electroless bath used for depositing Ag onto  $\text{SnO}_2$ -nanowire arrays.

Pretreatment solutions			
Sensitisation		Activation	
Sn chloride	0.35 g (0.04 M)	Ag nitrate	0.27 g (0.05 M)
Hydrochloric acid 37%	3 ml	Ammonia 25%	0.3 ml
Deionised water	47 ml	Deionised water	30 ml
Electroless bath			
Ag-complex solution		Reductive solution	
Ag nitrate	0.42 g (0.1 M)	D-glucose	0.54 g (3 M)
Ammonia 25%	0.4 ml	Deionised water	1 ml
Ethylenediamine	0.3 ml	Ethanol	0.1 ml
Deionised water	25 ml		

The experiments proceeded first by consecutively immersing the samples in the sensitising and activating solutions, for 10 min at each. Next, they were placed in the Ag-complex bath, followed by the addition of the reducing agent. Then, the electroless redox reaction was allowed to run for about 20 min, at room temperature and under mechanical agitation (pH  $\approx$  11). After each step, the samples were thoroughly rinsed with deionized water and then dried.

At the end of this process, a core-shell type of structure was obtained, consisting of SnO<sub>2</sub> nanowires (core) covered by a Ag layer (shell) 100 to 200 nm thick. The outer appearance of such structures can be observed in Fig. 3.2.

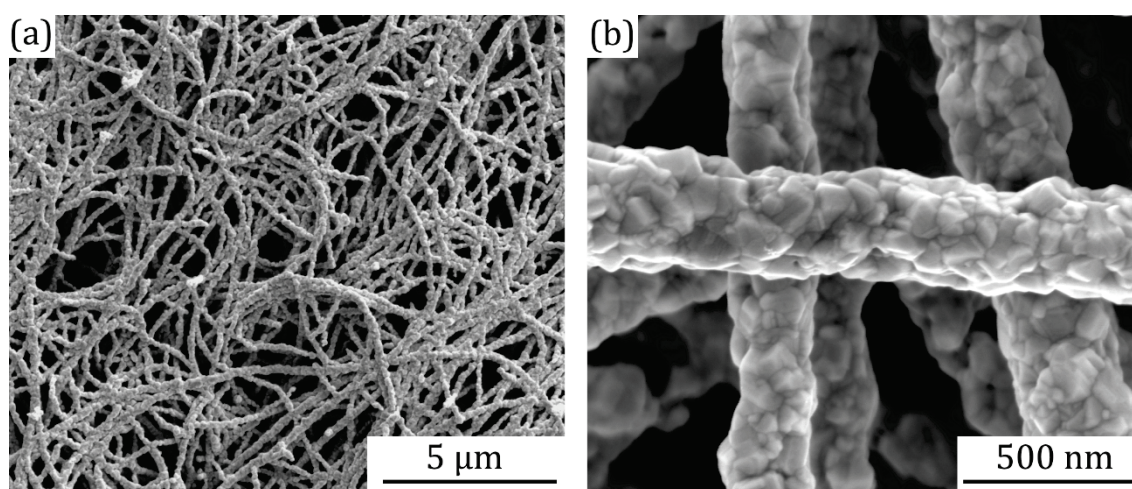


**Fig. 3.2** Ag-coated SnO<sub>2</sub>-nanowire arrays: (a) general and (b) close range visualisation.

### 3.1.3 Electrodeposition of the Ni matrix

The Ni matrix was galvanostatically (i.e., at constant current) deposited onto the Ag-coated SnO<sub>2</sub>-nanowire arrays. Here, a two-electrode electrochemical cell was used with Ni spheres acting as sacrificial anode. The electrolyte employed was a Ni-sulfamate solution, in which no enhancing additives (such as grain refiners, stress relievers or levelling agents) were present. Its composition is listed in Table 3.2. The Ni deposition was carried out at a nominal current density of 2 A/dm<sup>2</sup>, pH of 3.8 and 40 °C temperature, under magnetic stirring. The employed electrodeposition setup is displayed in Fig. 3.3.

The point at which the Ag-SnO<sub>2</sub> became fully embedded by the Ni matrix could be determined by observing the evolution of the cathode potential over time, which is represented in Fig. 3.4. Remaining constant the Ni-ion concentration, pH and temperature

**Table 3.2** Bath composition used during the electrodeposition of the Ni matrix onto the Ag-coated SnO<sub>2</sub> nanowires.

Ni sulfamate concentrate (185 g/l Ni)	924 g/l
Boric acid	35 g/l
Ni chloride	5 g/l
Na dodecyl sulphate	0.2 g/l
Balanced with distilled water	

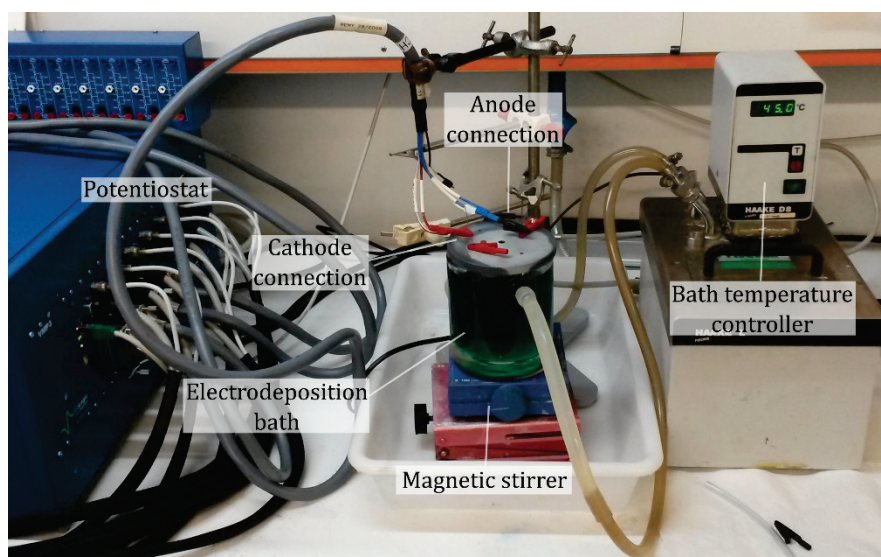


**Fig. 3.3** Two-cathode electrochemical cell (and related equipment) employed for the electrodeposition of the Ni matrix of the composite.

of the electrolyte, the behaviour of the cathode potential was essentially governed by the current density. For instance, almost constant voltage was measured when depositing a pure-Ni coating onto a flat substrate, after the initial transition period during which island formation and coalescence took place. This was the case since both current and cathode surface remained unchanged, thus resulting in a constant current density. For substrates crowded with Ag-coated nanowires, the nominal surface differed from real. The first corresponded to that of the flat substrate, which was in turn used for calculating the current required for producing the desired current density. The latter was given by the large surface of the nanowires and the free spots of the substrate. This was considerably larger than the nominal, thus resulting in a reduced initial (real) current density. As the matrix deposition proceeded, the nanowires became embedded and the real cathode surface gradually decreased. This resulted in an increasing current density and, therefore, an evolving cathode

potential. Once the nanostructures were completely integrated into the matrix, the Ni deposition would proceed at a practically constant cathode potential, as in the case of the flat substrate. Its value should be also quite similar to that of the flat-substrate situation, since nearly the same current density would be operating. At this point, the Ni electrodeposition had to be stopped.

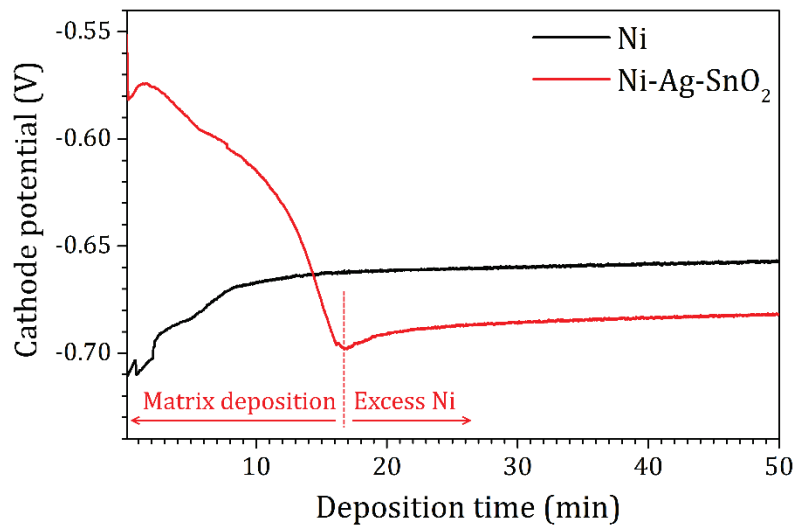


**Fig. 3.4** Comparison of the cathode potential evolution during the electrodeposition of a pure-Ni film and the Ni matrix of the Ni-Ag-SnO<sub>2</sub> composite. The sudden stabilisation of the cathode potential observed in the composite's curve is a good indicator of the moment at which the nanowires become completely embedded in the matrix.

Lastly, the excess of Ni eventually deposited above the volume containing the nanowires would be removed by mechanical polishing, achieving a final thickness typically between 5 and 10  $\mu\text{m}$ . In order to avoid damaging the surface, this was carefully performed using 3 and 1  $\mu\text{m}$  diamond suspensions and, finally, OP-S (40 nm SiO<sub>2</sub> colloid from Struers).

### 3.1.4 Specific-purpose isothermal annealing

The fabrication of standard Ni-Ag-SnO<sub>2</sub> composites did not involve thermal treating. Nevertheless, several samples were isothermally annealed for specific analysis purposes. In particular, this was done for the evaluation of thermal stability and for obtaining coarser microstructures for the investigation of tribomechanical properties. Said treatments were conducted at 300 and 500  $^{\circ}\text{C}$  for 10 h, at high vacuum ( $10^{-7}$  mbar), with heating and cooling rates of 10  $^{\circ}\text{C}/\text{min}$ .

## 3.2 Material characterisation techniques

A broad variety of methods were employed for characterising the microstructure and properties of the samples. These are briefly summarised in the next sections, including relevant experimental parameters.

### 3.2.1 Focused ion beam (FIB) and scanning electron microscopy (SEM)

A FEI Helios Nanolab 600 FIB/SEM dual-beam system was used for cross-sectioning and imaging the samples. The FIB consisted in a Ga-ion source operating at 30 kV, oriented at  $52^\circ$  with respect to a field-emission electron gun (see Fig. 3.5). The latter was used for SEM and scanning transmission electron microscopy (STEM) imaging at 5 and 30 kV, respectively. Moreover, FIB ion-channelling-contrast micrographs (i.e., images formed by ion-induced secondary electrons) were also recorded.

This device allowed also performing serial-sectioning tomography (FIB tomography). The subsequent reconstruction and quantitative analysis were carried out with the Mercury Amira and Mavi software, respectively.

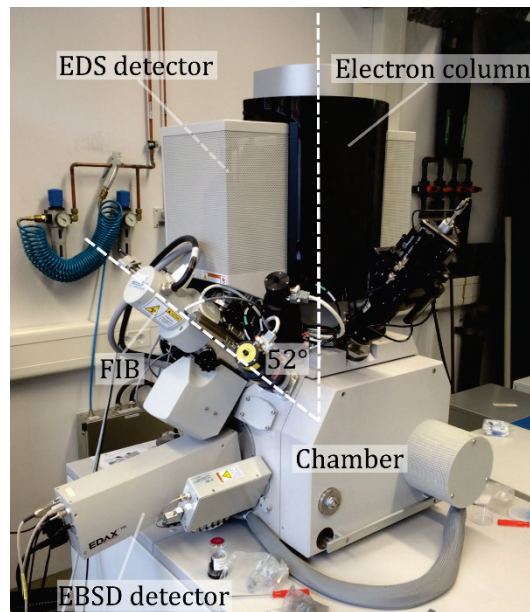


**Fig. 3.5** FIB/SEM dual-beam system used for cross-sectioning and imaging of the samples. FIB tomography, electron-backscatter diffraction and energy-dispersive X-ray spectroscopy analysis were also among its available features.

### 3.2.2 Electron backscatter diffraction (EBSD)

The FIB/SEM dual-beam system had an EBSD module (EDAX) incorporated, which was used for the determination of grain size and the analysis of crystallographic texture. This was performed at 15 or 20 kV, with currents of 11 or 22 nA. The obtained data was normalised and filtered by confidence index (CI), removing all points with  $CI < 0.1$  and those grains intersected by the edges of the scanned area. The step size was chosen to be one fifth (or less) of the average grain diameter of the sample.

### 3.2.3 Energy-dispersive X-ray spectroscopy (EDS)

The also available EDS detector (EDAX) allowed performing chemical analysis of the near-surface region of the samples. This was carried out at voltages ranging from 10 to 30 kV.

### 3.2.4 Transmission electron microscopy (TEM)

A JEOL JEM-2011 device was used for high-resolution TEM imaging and selected-area diffraction (SAD) analysis, operated at an acceleration voltage of 100 kV.

### 3.2.5 Atomic-force microscopy (AFM)

A Veeco Dimension 3000 atomic force microscope was employed for surface profiling and for the calculation of roughness parameters. The measurements were performed in tapping mode, recording 512 lines per scan at 0.5 Hz.

### 3.2.6 High-temperature X-ray diffraction (XRD)

In-situ XRD measurements during non-isothermal annealing were carried out using a Panalytical X'Pert MPD X-ray diffractometer, equipped with an Anton Paar HTK1200 high-temperature chamber. The diffractograms were recorded at high vacuum ( $10^{-6}$  mbar) using a Bragg-Brentano  $\theta$ - $\theta$  configuration with  $\text{CuK}_{\alpha 1}$  radiation, applying voltage and current of 40 kV and 40 mA, respectively. The diffraction angle ( $2\theta$ ) varied from 35 to 95° with a step size of 0.0131°. The diffractograms were obtained at 30 °C; and from 50 to 600 °C, with a 50 °C step. For doing so, the samples were heated at a rate of 10 °C/min, letting the temperature stabilise for 5 min before each measurement, which proceeded afterwards for about 7 min.

### 3.2.7 Nanoindentation for the analysis of mechanical properties

An ASMEC UNAT nanoindenter was used for recording load-displacement curves, allowing the evaluation of mechanical properties by means of the Oliver-Pharr method [144,145]. The nanoindentation tests followed the standard procedure for fast hardness ( $H$ ) measurements according to the norm ISO-14577 [146]. A diamond Berkovich indenter (172 nm radius) was used, applying a maximal normal load ( $F$ ) of 10 mN. For the sake of obtaining statistically representative values, several tens of measurements were carried out over different areas at the surface of each sample.

The analysis of the results was automatically carried out by the software of the device (InspectorX). This started with the indenter's maximum displacement ( $h$ ) and the contact rigidity ( $S$ ), parameters which were directly obtained from the load-displacement curves (see Fig. 3.6). The latter corresponded to the initial slope of the unloading segment of the curves. Next, the depth of contact of the indenter with the sample ( $h_c$ ), which differed from  $h$  due to the pile-up/sink-in effect, was given by

$$h_c = h - \epsilon(F/S), \quad (3.1)$$

where the parameter  $\epsilon$  described the relationship between the elastic deformation over and beneath the indenter-sample contact area. A value of  $\epsilon$  of 0.75 was adopted (which normally lies between 0.7 and 0.8), as recommended by the norm [146]. Then, the projected area of contact during indentation ( $A_c$ ) could be calculated from the indenter area function as

$$A_c = (-0.0015 + 0.0803h_c^{0.25} + 0.4457h_c^{0.5} + 3.7893h_c + 0.9987h_c^{1.5})^2. \quad (3.2)$$

Once knowing  $S$  and  $A_c$ , the sample's  $H$  and the reduced Young's modulus ( $E_r$ ) were computed as

$$H = F/A_c \quad (3.3)$$

and

$$E_r = (S/2)(\pi/A_c)^{0.5}. \quad (3.4)$$

Finally, the proper Young's modulus ( $E$ ) of the indented material was determined as

$$E = (1 - \nu^2)/[1/E_r - (1 - \nu_i^2)/E_i], \quad (3.5)$$

where  $\nu$  denoted the Poisson's ratio (0.3 for the analysed samples) and the subindex  $i$  referred to the properties of the indenter ( $E_i$  and  $\nu_i$  had values of 1140 GPa and 0.07, respectively).

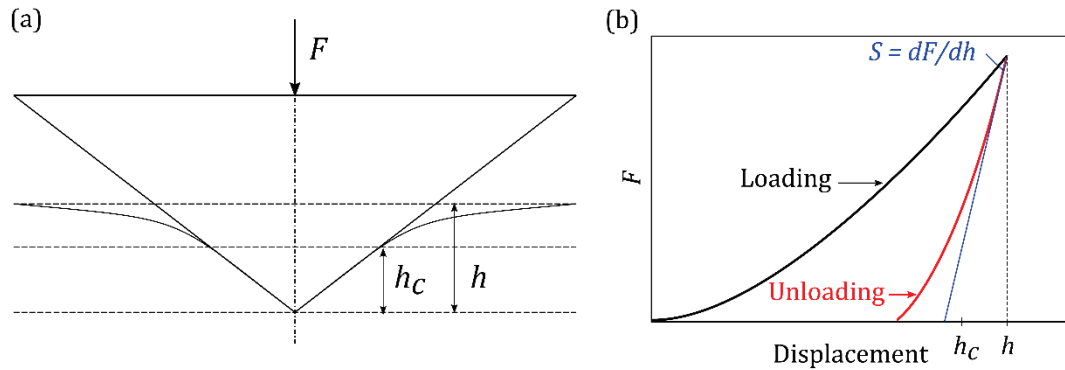


**Fig. 3.6** (a) Sink-in of a surface during indentation (which is normally the case for ductile metals), resulting in a reduced depth of contact ( $h_c$ ) with respect to the indenter's maximum displacement ( $h$ ). The opposite case is known as pile-up, where the indented material flows plastically and surrounds the indenter above the original surface plane. (b) Exemplary load-displacement curve obtained from a nanoindentation measurement. The contact rigidity ( $S$ ) is given by the slope of the unloading segment at maximum load. This magnitude, together with the applied load and  $h$ , were used to derive all other parameters and material properties.

### 3.2.8 Friction and wear evaluation

The same equipment used for the nanoindentation measurements had a lateral force unit incorporated, which allowed performing tribological experiments in a linearly reciprocating ball-on-flat configuration. Unlubricated sliding friction and wear tests were conducted in ambient air using a diamond ball of 5.8  $\mu\text{m}$  radius subjected to  $F$  of 5, 10, 20 and 30 mN. At each experiment the ball slid along a 100  $\mu\text{m}$ -long track, performing 100 cycles. A cycle was defined as two stroke lengths (back and forth, amounting a sliding distance of 200  $\mu\text{m}$ /cycle), having a frequency ( $f$ ) of 0.1 Hz. In order to obtain statistically representative values, at least three measurements were carried out at each  $F$  at different areas of each sample.

### **3.2.8.1 White-light interferometry (WLI)**

The resulting wear volumes ( $W$ ) and the initial (prior testing) root-mean-square roughness ( $R_q$ ) were measured by means of WLI using a ZYGO NewView™ 7300 (profilometer).

### **3.2.9 Four-point probe electrical resistivity measurements**

The bulk electrical resistivity ( $\rho$ ) of the samples was determined employing a linear-array 4-point-probe setup, having a 1 mm probe separation. The measurements were carried out at room temperature, applying currents ( $I$ ) ranging from 5 to 99 mA.

## 4 Microstructure and mechanical properties characterisation

### 4.1 Introduction

The microstructure and properties of materials are intrinsically connected by the fact that the former defines and governs the latter. For that reason, the materials science has sought since its beginnings to further understand their hidden relationships and, accordingly, to develop novel processing methods which would allow tailoring the microstructure and thus controlling and enhancing the resulting properties. Such efforts have been always driven by the ever-expanding demand of new high-tech applications and the need to comply with increasingly demanding standards and service conditions.

A well-known example of this is given by the use of films and coatings for improving the performance of the coated material with regard to certain properties and operating conditions. Ni-based films have been widely applied to this end, both as single-phase materials (pure and alloyed) and as metal-matrix composites, mostly due to their high strength and hardness [33,34]. The electrodeposition technique has proven to be a fast, relatively simple and highly scalable method for the production of such films. Through the modification of experimental parameters such as the current density, bath composition and temperature, the microstructure and mechanical properties of the films can be accurately modified [147–149]. Most research efforts and available literature on this subject concentrate on the controlled reduction of grain size, aimed to enhance the mechanical response of the materials. This strengthening is given by the increase in the density of grain boundaries, which act as pinning points for dislocations, impeding their further propagation upon plastic deformation. Moreover, an additional hardening results from dislocation interactions induced by multiple slip in the vicinity of grain boundaries. The relationship between grain size and strength was firstly mathematically described by Hall and Petch [150,151], which led to a renewed interest in the investigation of the working principles behind this strengthening mechanism and the development of new methods for the production of high-strength materials.

That being said, the work presented in this chapter had two main purposes. First, to provide a detailed picture of the main microstructural features of the Ni-Ag-SnO<sub>2</sub> films, gaining an understanding of the role played by the Ag-coated nanowires in their configuration. Second,

to evaluate the mechanical behaviour of the composite, elucidating its governing mechanisms with the help of the obtained microstructural information.

Supporting this analysis and for comparison purposes, two sets of pure-Ni films were also investigated: (i) one which was deposited using exactly the same bath and experimental parameters as for the Ni-Ag-SnO<sub>2</sub> and (ii) another whose grain size was refined to match that of the composite's matrix. The hardness, Young's modulus and stress-strain relationship of the films were evaluated from nanoindentation data. For the study of the plastic component of the tensile behaviour of the samples, a straightforward calculation method was performed, based on the combination of analytical and computational models available in the literature.

## **4.2 Experimental details**

The Ni-Ag-SnO<sub>2</sub> composite films were produced as described in 3.1. Two sets of pure Ni films were used for comparison and analysis purposes, denominated coarse-grained (Ni<sub>cg</sub>) and fine-grained (Ni<sub>fg</sub>) Ni. They were deposited using the same bath and experimental parameters as for the composite's matrix, with the only addition of 0.1 g/l of saccharin (grain refiner) in the case of Ni<sub>fg</sub>, in order to obtain a grain size similar to that of the composite's matrix.

The evaluation of the mechanical properties of the samples was based on nanoindentation tests, which followed the procedure described in 3.2.7.

## **4.3 Results and discussion**

### **4.3.1 Microstructure characterisation**

The Ni-Ag-SnO<sub>2</sub> composite presented an inhomogeneous, gradient microstructure which, in the as-deposited state, could be divided into four regions or layers according to their phase distribution (as depicted in Fig. 4.1). From the substrate upwards, these arbitrary zones enclosed the following: (i) a Ag-SnO<sub>2</sub>-rich region, given by the presence of all the existing nanowires and, therefore, with higher Ag content (Ag was deposited onto the SnO<sub>2</sub> nanowires and onto the exposed substrate at their feet); (ii) an area with higher predominance of the Ni matrix, since fewer nanowires reached this level given their different lengths and how they bent during growth; (iii) a Ni-rich region where only the longest and straightest Ag-coated nanowires were able to extend; and, finally, (iv) an excess

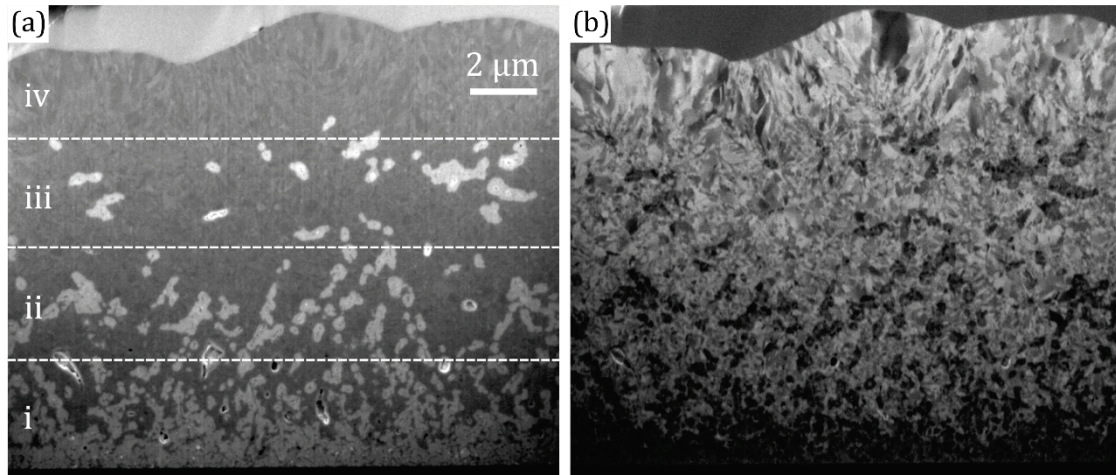


**Fig. 4.1** Cross-section of an as-deposited Ni-Ag-SnO<sub>2</sub> film (prior to polishing and removal of excess Ni) imaged by (a) standard SEM and (b) FIB ion-channelling contrast. The former exposes clearly the gradient nature of the microstructure, where the dotted lines enclose regions (i-iv) of different composition in terms of reinforcement content. Here, the brighter phase embedded in a darker matrix corresponds to the Ag-SnO<sub>2</sub>. The second image (b) reveals the fine-grained morphology of the matrix, which resulted from the strong pinning of grain boundaries exerted by the Ag-coated nanowires during the Ni deposition.

of pure Ni close to the surface, as a consequence of an overextended electrodeposition time. This excess of Ni and part of the adjacent layer (iii) were removed by polishing, leaving behind a fine-grained microstructure which resulted from grain growth stagnation due to the pinning force exerted by the Ag-SnO<sub>2</sub> during the electrodeposition of the matrix [152,153]. The nanowires reaching the surface were randomly oriented with respect to it. Most of them, long ones, would bend and thus lie parallel to the film. The shorter, straight nanowires could intercept the surface at almost right angles.

The topography of the electrodeposited Ni matrix was also influenced by the presence of the nanowires. The Ni-Ag-SnO<sub>2</sub> composite developed a much more irregular surface, consisting of agglomerated spherical protrusions, contrasting with the much flatter pure-Ni films (see Fig. 4.2). This was confirmed by AFM measurements, which revealed that the roughness parameter  $R_q$  of the composite was about six times that of pure Ni. This can be understood considering the fact that the Ni matrix deposition proceeded not only from the substrate upwards but also from the nanowires outwards, thus differing from the progressive layer-by-layer formation which characterise uniform films. Moreover, the randomly oriented nanowires and the irregularly growing Ni deposits constituted high-curvature (or

edged) surfaces, where the concentration of electrical field lines increased, leading to gradients in the amount of the deposited metal. The rough features of the composite's surface were later flattened upon the removal of the excess of Ni by mechanical polishing.

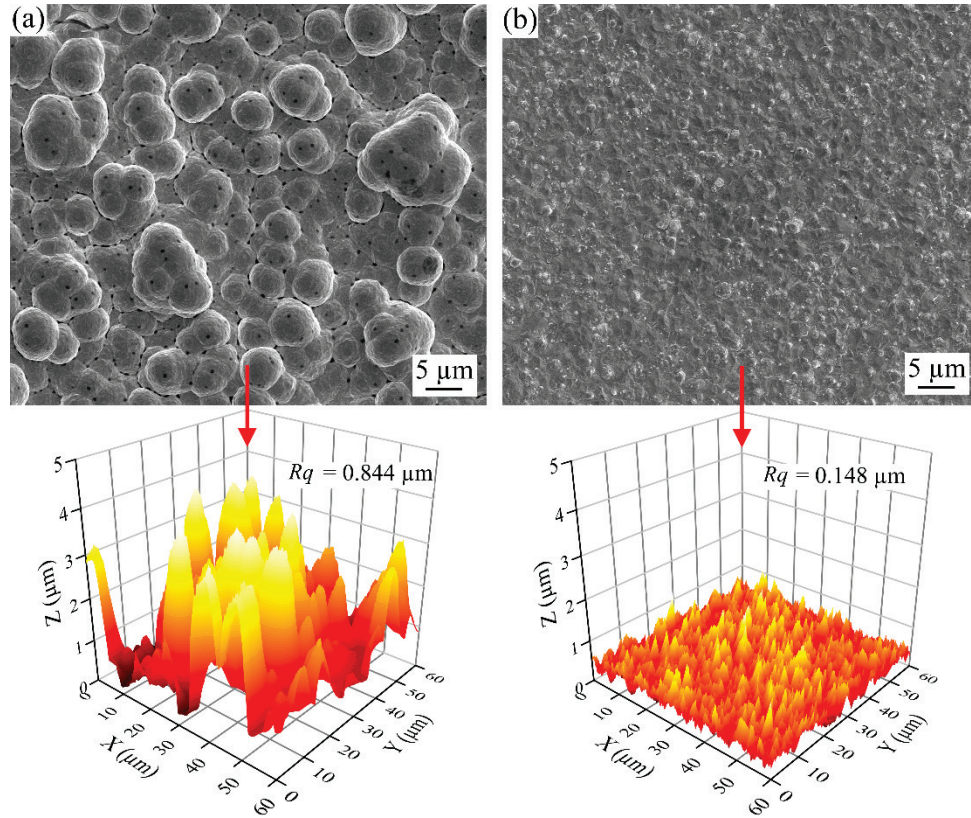


**Fig. 4.2** Surface view of electrodeposited Ni (a) onto Ag-coated SnO<sub>2</sub> nanowires (composite) and (b) on a flat substrate. Corresponding AFM topographic height profiles are also shown with their respective  $R_q$  values. The presence of the nanowires translated into a 500% increase in roughness.

TEM analysis allowed studying the bonding between Ag and SnO<sub>2</sub>. As observed in Fig. 4.3, a continuous, pore-free interface was found, indicating good wetting between them. Furthermore, SAD patterns from both phases allowed clearly confirming their crystalline nature (single-crystalline in the case of the nanowires). Regarding their integration into the matrix, the Ag-Ni interface displayed good wetting between both metals in general, which characterised the good quality and strength of their bonding (Fig. 4.4). However, some degree of porosity was also observed at said interface in a small number of cases. Other than from weak bonding or incomplete wetting, this could have resulted from the release of internal stresses upon removal of the thin specimen (used for imaging) from the sample. Moreover, the ion-beam-assisted thinning procedure could have introduced further damage.

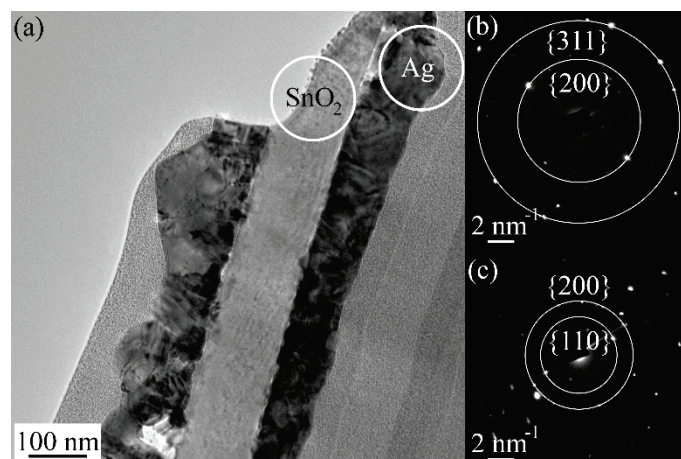


**Fig. 4.3** (a) Bright-field TEM image of the longitudinal section of a Ag-coated nanowire. The SAD patterns from (b) Ag and (c) SnO<sub>2</sub> were obtained from the areas enclosed by circles.

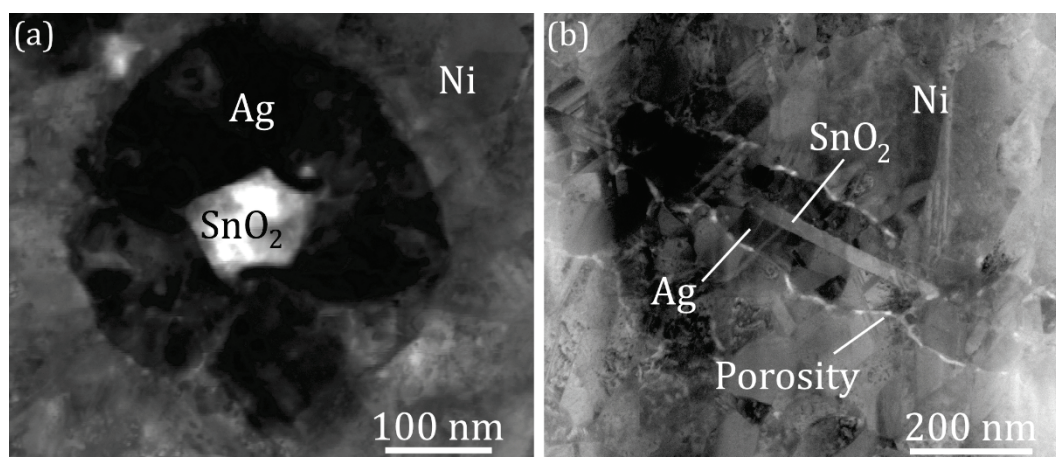


**Fig. 4.4** Bright-field STEM images displaying the (a) cross and (b) longitudinal sections of Ag-coated SnO<sub>2</sub> nanowires within a Ni matrix.

Determining the relative amount of each phase present in the composite resulted quite challenging. Many fabrication methods allow precisely defining the resulting material composition by controlling, for instance, the quantities of different powders being mixed for sintering; the concentration of species to be co-deposited in an electrochemical bath; or the sputtering rate of different targets. Unfortunately, such direct and conclusive approaches were not available (or rather possible) for the three-step fabrication procedure of the Ni-Ag-SnO<sub>2</sub> films. Moreover, no experimental characterisation technique available was able to provide such information (at least not with an acceptable relation between speed and analysed volume) due to restrictions inherent to the samples. These limitations were mainly morphological or compositional in nature. The former involved the gradient microstructure (which

impeded using surface techniques as their results would not be representative of the whole) and the impossibility of performing large and clean cross-sectional cuts without damaging the films (due to their negligible thickness with respect to that of the substrate). The latter related to the large content difference between the three phases (mainly Ni and Ag vs SnO<sub>2</sub>), resulting in spectroscopic techniques yielding poor signal-to-noise ratios or ambiguous results. For instance, an interesting approach considered was to perform EDS on FIB cross-sections. However, the low signal from the characteristic X-rays of Sn ( $L_{\alpha 1}$  at 3.44 eV) overlapped with the secondary peaks of Ag ( $L_{\beta 2}$  and  $L_{\gamma 1}$  at 3.35 and 3.52 eV, respectively) [154]. Moreover, the X-rays reaching the detector did not originate homogeneously from all over the scanned surface (due to higher absorption of those close to the substrate plus the shadowing effect), yielding only localised (non-representative) results.

In light of the issues above described, the approach taken for evaluating the composition of the films involved the stereological analysis of SEM images from a large number of cross-sectional cuts performed with a FIB, which was complemented by FIB tomography. It is known from the fundamental relationships of stereology, that the volume fraction of a phase within the structure can be estimated from its area fraction on an image [155,156]. Then, first, the combined area fraction of Ag and SnO<sub>2</sub> was easily determined given the high contrast observed in SEM micrographs between Ni and Ag (see Fig. 4.1a). Similar information was obtained from FIB tomography of the composite but directly in terms of volume fraction. Assessing the amount of SnO<sub>2</sub> nanowires was not so straightforward. Given their small diameters, it was not always possible to clearly discern them within the Ag at the relatively low magnification levels required to display the whole thickness of the film. Consequently, the SnO<sub>2</sub> content was calculated by analysing several Ag-SnO<sub>2</sub> clusters from different regions of the cross-sections, in which the SnO<sub>2</sub> could be certainly distinguished. The results from these observations (i.e., the fraction of SnO<sub>2</sub> within the Ag-SnO<sub>2</sub> clusters) were then extrapolated for the whole composite. Such procedure would be valid since the amount, disposition and morphology of the Ag phase were directly related to those of the nanowires, independently from the gradient nature of the microstructure. Moreover, high-resolution FIB tomography of several arrays of shorter, free-standing nanowires (i.e., without Ag and Ni) revealed spatial occupation values in good agreement with the volume fraction of SnO<sub>2</sub> estimated for the composite. Some of the FIB-tomography reconstructions considered for this analysis are displayed in Fig. 4.5. Then, through this whole process, the contents of Ag and SnO<sub>2</sub> were found in the range of 25-40 and 2-3 vol%, respectively, together with a porosity of about 4%. Specifically in the top or near-surface region of the composite, which

was mostly accountable for the response towards nanoindentation, the films contained 5 to 15 vol% Ag and about 1 vol% SnO<sub>2</sub>. This showed consistency with EDS measurements at the surface, which detected  $9 \pm 4$  vol% Ag.

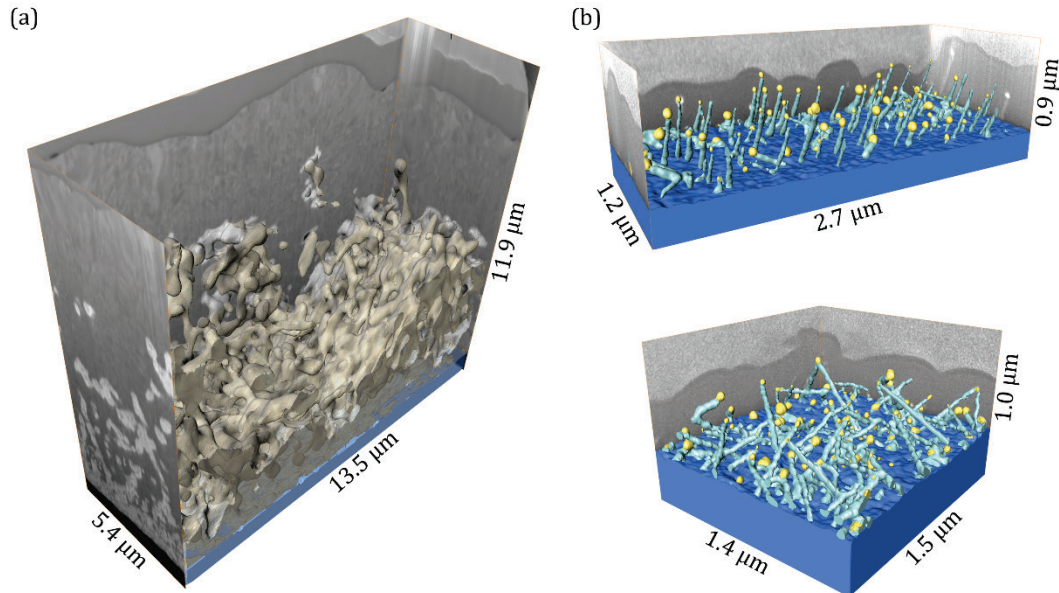


**Fig. 4.5** FIB-tomography reconstructions from (a) a Ni-Ag-SnO<sub>2</sub> composite film and (b) from arrays of free-standing SnO<sub>2</sub> nanowires.

The mean area-weighted grain size ( $d_A$ ) of the composite and Ni reference samples (Ni<sub>cg</sub> and Ni<sub>fg</sub>) was determined by EBSD, and the results are displayed in Fig. 4.6. The collected data showed very good fitting with the lognormal distribution function (bimodal in the case of Ni<sub>cg</sub>). The introduction of the Ag-SnO<sub>2</sub> produced a reduction in  $d_A$  of 85%. This was attributed to the pinning of grain boundaries by the nanowires and the collision of multiple Ni growth fronts advancing in all directions (not only from the substrate upwards but also from the randomly oriented nanostructures outwards), resulting in high energy barriers for further crystallite growth. A reduction of the same order was achieved in the case of Ni<sub>fg</sub> by the addition of 0.1 g/l of saccharin in the electrolyte. Grain refiners as such adsorb onto the deposit, limiting the surface diffusion of ions and, thus, increasing nucleation while hindering two-dimensional growth [157].

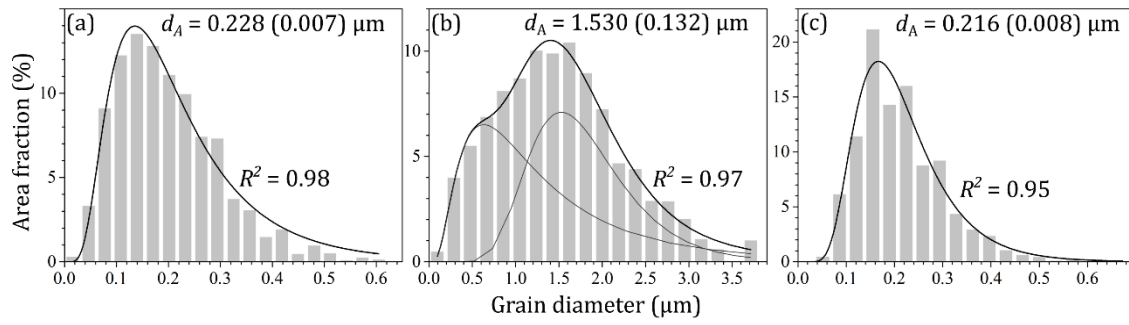


**Fig. 4.6** Grain size distribution histograms (with their corresponding fitting curves) obtained by means of EBSD from (a) Ni-Ag-SnO<sub>2</sub>, (b) Ni<sub>cg</sub> and (c) Ni<sub>fg</sub>. The values of  $d_A$  are shown with their standard deviation in brackets.

Unlike the non-textured, equiaxed-grain structure of the Ni-Ag-SnO<sub>2</sub> (displayed in Fig. 4.1b), both Ni samples presented columnar or rather fibrous-like grains (Fig. 4.7) with a  $\langle 100 \rangle$  fibre texture perpendicular to the film surface (Fig. 4.8). Such characteristics are commonly found in the literature for similar deposition conditions [147–149,158–160]. The elongated grains indicated the absence of continuous nucleation [161], caused by the relatively low current densities required for the galvanostatic deposition. According to the preferred-growth model, the texture of films is controlled by their lattice surface energy and the concentration of adjacent ions [162]. It states that, at low concentrations (i.e., low current density), the crystal planes of lowest energy deposit parallel to the substrate. With increasing ion concentration (higher current density), the orientation shifts to that of higher-energy planes. Then, for FCC metals, the energy of crystallographic planes is ordered as follows:  $\{111\} < \{100\} < \{110\}$ . Pangarov had previously arrived at similar conclusions by calculating the work of formation of two-dimensional nuclei. He found that with increasing deposition overpotential (i.e., increasing current density), the preferred orientation of FCC metals shifts from  $\{111\}$  to  $\{100\}$  and then  $\{110\}$  [163,164]. Thus, the  $\{100\}$  orientation of Ni<sub>cg</sub> and Ni<sub>fg</sub> corresponded with a middle overpotential according to Pangarov, which resulted from the combination of a relatively low current density and the intrinsically large overpotential of Ni electrodeposition [163]. The dissimilar features of the Ni-Ag-SnO<sub>2</sub> composite (i.e., randomly oriented, equiaxed grains) were the result of non-flat crystal growth fronts (given by the random spatial orientation of the nanowires), larger surface diffusion paths, the strong pinning of boundaries of growing crystals and a reduced current density (due to the large surface inherent to the nanowires, significantly greater than that from the flat substrate). As a final remark, no porosity was detected in the cross-section of the pure-Ni films by FIB/SEM.

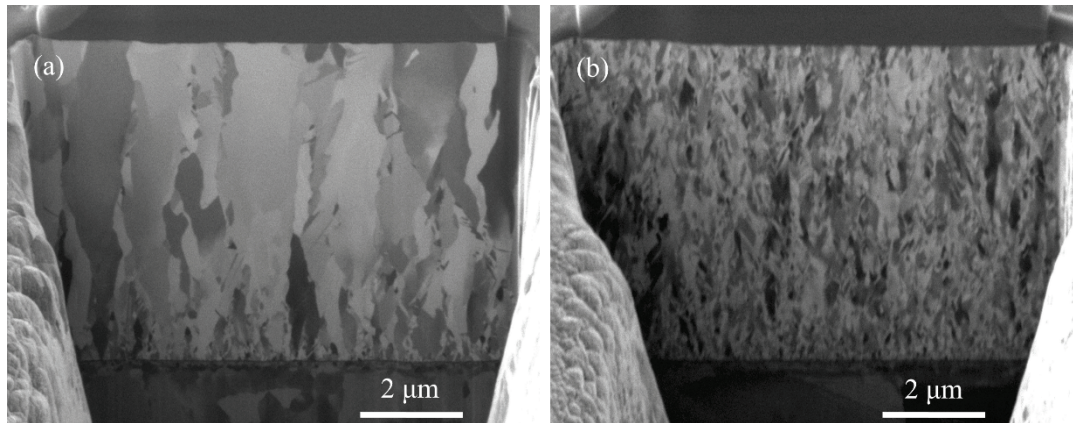


**Fig. 4.7** Ion-channelling-contrast images of FIB cross-sections of (a)  $Ni_{cg}$  and (b)  $Ni_{fg}$  samples.

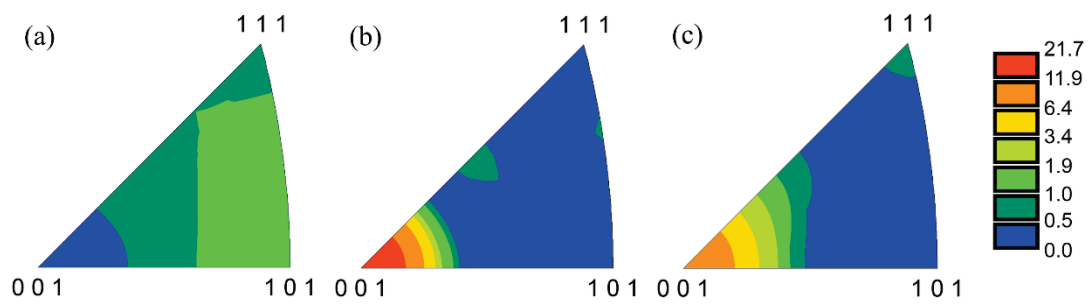


**Fig. 4.8** [001] inverse pole figures recorded at the surface of (a)  $Ni-Ag-SnO_2$ , (b)  $Ni_{cg}$  and (c)  $Ni_{fg}$  films.

## 4.3.2 Mechanical properties evaluation

### 4.3.2.1 Hardness

Typical force-displacement curves of the investigated materials are displayed in Fig. 4.9. The indentation depths fell in the range of 270-420 nm, comprising in all cases less than 10% of the film thickness (mostly under 5%), excluding any influence of the substrate on the experimental results [165].

The obtained values of hardness ( $H$ ) are shown in Table 4.1.  $Ni_{fg}$  showed a 100% increase with respect to  $Ni_{cg}$ , which can be attributed to the grain-boundary strengthening mechanism since the only major difference between these samples was their grain size. Regarding the composite, a first glimpse revealed a 66% increment for the  $Ni-Ag-SnO_2$  with respect to  $Ni_{cg}$ , being this the net effect of introducing the  $Ag-SnO_2$  phase in the material. As it was the case for  $Ni_{fg}$ , this increase in  $H$  originated mostly from the aforementioned 85%

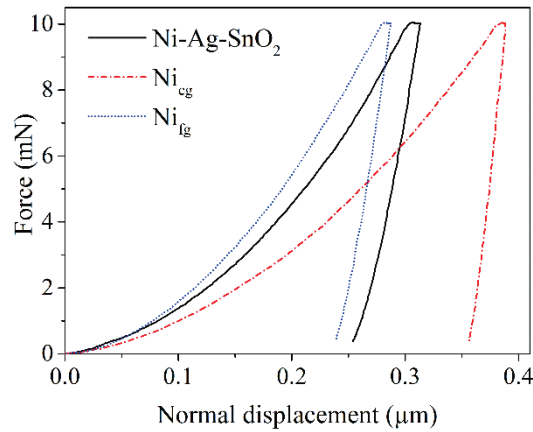


**Fig. 4.9** Exemplary nanoindentation load-displacement curves from the investigated films.

reduction in  $d_A$ . Several complementary models have been developed to describe material strengthening through grain refinement, which have been summarised in the review papers from Kato [166], Malygin [167] and Meyers et al. [168]. Among them, the dislocation pile-up model [169] and those based on higher dislocation production in polycrystals are usually adopted. The dislocation pile-up model states that at the onset of plastic deformation, dislocations generated from Frank-Read sources pile up at grain boundaries. This builds up a stress concentration until a critical value is reached, at which dislocations start to form in the contiguous grain and thus the material yields. If the grain size is reduced (i.e., the total grain-boundary surface is increased), a higher stress will be needed for concentrating the same amount of dislocations in the pile-up. The models based on a higher dislocation yield in polycrystals contemplate, for instance, grain boundaries acting as sources of dislocations (as proposed by Li [170]) and Ashby's concept of geometrically-necessary dislocations [171], responsible of accommodating the deformation of plastically inhomogeneous parts of materials (e.g., grains in polycrystals). These grain-boundary strengthening mechanisms are valid for grain sizes down to about 10 nm. Underneath that limit, material softening commonly associated to grain-boundary sliding is likely to occur [172].

**Table 4.1** Hardness and Young's modulus of the samples, obtained by nanoindentation (standard deviation in brackets).

	$H$ (GPa)	$E$ (GPa)
Ni-Ag-SnO <sub>2</sub>	4.45 (0.30)	135.8 (13.9)
Ni <sub>cg</sub>	2.68 (0.12)	162.6 (28.4)
Ni <sub>fg</sub>	5.34 (0.06)	177.5 (12.1)

Another mechanism which could have played a role in increasing the composite's  $H$  was the dispersion strengthening produced by the SnO<sub>2</sub> nanowires. According to Orowan's theory [173], hard reinforcing particles force moving dislocations into bowing out between them, hindering their motion and leaving behind dislocation loops, which increase the stress required for the propagation of other incoming dislocations. This mechanism becomes more active with increasing volume fraction and smaller size of the particles. In the composite's case, the inhomogeneous distribution of the nanowires as well as their relatively low content and large dimensions ruled out the possibility of a significant weight of this mechanism in the whole strengthening of these films.

On the other hand, a decrease in  $H$  of about 17% was observed for the composite with regard to Ni<sub>fg</sub>, having both approximately equal grain sizes. In order to determine if this deviation corresponded to a mild random fluctuation or rather was microstructure related, the Hall-Petch [150,151] behaviour of the films was analysed, which is given by

$$H = H_0 + k_H d^{-0.5}. \quad (4.1)$$

Here,  $H_0$  and  $k_H$  are constants and  $d$  refers to grain size. In order to obtain additional points for the Ni curve, more samples were produced with grain sizes differing from those of Ni<sub>fg</sub> and Ni<sub>cg</sub>. Intermediate sizes were achieved by using saccharin concentrations below 0.1 g/l and larger ones through annealing. For the Ni-Ag-SnO<sub>2</sub> curve, larger grain sizes were obtained by removing slightly less material from layer iii (Fig. 4.1) during polishing. Therefore, less Ag-coated nanowires were present at the top of the film, resulting in coarser matrix grains. Moreover, even larger grains emerged from annealing this last set of samples. In all cases, the annealing treatments were performed as described in 3.1.4.

The Hall-Petch curves are shown in Fig. 4.10. Only by the inclusion of the data point corresponding to the composite, the coefficient of determination  $R^2$  of the linearly fitted Ni curve dropped from 0.99 to 0.94 and the residual sum of squares increased by almost 500% (see Fig. 4.10a and b), indicating a weaker fit and a much higher discrepancy with the model, respectively. This information supported the idea that other factors intervened in the mechanical response of the composite, which were absent for the Ni films. This softening of the Ag-Ni-SnO<sub>2</sub> with respect to Ni<sub>fg</sub> was a consequence of the presence of the weaker Ag phase. With negligible solubility or reactivity with Ni [9], no solid-solution strengthening was possible, leaving pure Ag as a relatively easier path for dislocation motion. With much lower stacking-fault energy than Ni (18 vs 110 mJ/m<sup>2</sup>, respectively [174]), Ag readily deforms by

twinning, which also derives from the slip of Schockley partial dislocations. Porosity is also to be accounted in part responsible for degrading the mechanical response of the composite, since it disrupts the approximately homogeneous load transfer that should take place in a fully dense microstructure. Stresses concentrate around pores, leading in some cases to their collapse and thus, local failure of the material occurs.

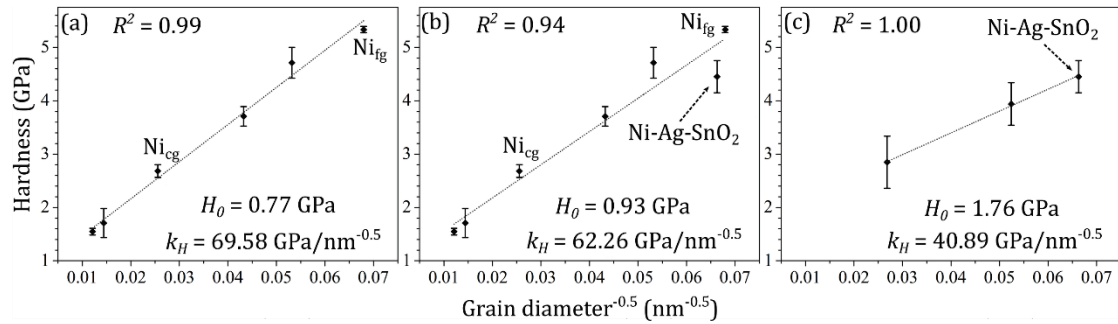


**Fig. 4.10** Hall-Petch plots from the hardness of (a) pure-Ni films, (b) pure Ni together with one data point corresponding to the Ni-Ag-SnO<sub>2</sub> and (c) composite films. The error bars are given by the standard deviation.

Another interesting observation was the 41% reduction in the slope  $k_H$  of the Hall-Petch curve of the composite (Fig. 4.10c) with respect to that of Ni (Fig. 4.10a). This showed a higher strengthening for pure Ni or, likewise, less sensitivity in the mechanical response of the composite towards changes in grain size (i.e., for an equal variation in grain size, the change in  $H$  of the composite would be 41% smaller than that of pure-Ni films). The main reason behind this was that the grain size of the Ni-Ag-SnO<sub>2</sub> samples considered for the Hall-Petch analysis corresponded to the one measured by EBSD at the surface, which did not necessarily match that from inner regions closer to the substrate. These inner regions possessed a higher Ag-SnO<sub>2</sub> content, bearing stronger pinning forces which would have resulted in a quite stable grain size even after annealing. Therefore, the inner region of all these samples possessed similar strength, which partially compensated the softening produced at the samples whose outer grain size changed. Finally, the texture could have also played a role in this matter. The slope  $k_H$  is expected to be larger for {100}-textured Ni than for the randomly oriented matrix of the composite, likely as a result of a reduced density of dislocation sources due to the lower density of high-angle grain boundaries [175].

#### **4.3.2.2 Young's modulus**

The Young's modulus ( $E$ ) is a characteristic parameter of the elastic behaviour of materials. It depends on the binding energy of atoms and it is generally considered to be relatively unaffected by changes in the grain size distribution.

The  $E$  obtained from the three systems under study are listed in Table 4.1. Both  $Ni_{cg}$  and  $Ni_{fg}$  showed reduced values with respect to the 200 GPa of bulk Ni [123]. Several works from different authors reported similar results for Ni films, even down to values below 100 GPa [158,176–179]. Based on their findings in relation to similar electrodeposition parameters and resulting film features, the reduction in  $E$  observed in the present work could be attributed to the following reasons: the use of current densities high enough to limit the mass transport of Ni ions, which hindered the rearrangement of atoms and thus produced less dense coatings (i.e., nanoporosity); the texture of the films, since the theoretical  $E$  of {100}-oriented Ni is 130 GPa; and the presence of internal stresses, which are inherent to electrodeposited Ni coatings. Another reason to consider would be the incorporation of non-metallic species (e.g., ammonium and sulfate ions from hydrolysis reactions or carbonaceous material and sulfur from the saccharin), which would affect the film's microstructure and atomic arrangement [161].

The Ni-Ag-SnO<sub>2</sub> films exhibited even lower values, which was expected due to the nature of the of Ag phase (having  $E$  of 83 GPa [123]) and the presence of both porosity and sites of poor bonding between the three constituent phases. In order to support these observations, an attempt was made to model the composite's  $E$ . This was carried out by applying the fundamental analytical solutions, as presented by Wang and Pan [180], for calculating the effective properties of two-component materials. For the matrix, the  $E$  of  $Ni_{cg}$  was adopted, since their deposition conditions were identical. Considering that these models are, basically, different variants of the rule of mixtures, the weight of the SnO<sub>2</sub> nanowires could be conveniently neglected due to their low volume fraction. The contribution of porosity was weighed in by using the empirical relation given by Watchman and Mackenzie [181,182]:

$$E = E_0(1 - f_1p - f_2p^2), \quad (4.2)$$

where  $E_0$  is the elastic modulus of the pore-free material,  $p$  is the porosity and  $f_1$  and  $f_2$  are constants, which assume values of 1.9 and 0.9, respectively, when considering spherical voids and Poisson's ratio of 0.3. It can be deduced from Eq. 4.2 that, for low up to middle

porosity ( $p < 20\%$ ), the percent reduction in  $E$  is about two times the value of  $p$ . Accordingly, the 4%  $p$  of Ni-Ag-SnO<sub>2</sub> corresponded to a reduction in  $E$  of about 8% with respect to  $E_0$ .

The values obtained from these models are listed in Table 4.2. All of them returned similar results, with an average value of 142 GPa (4.6% higher than the one measured by nanoindentation). The best fit was achieved with the denominated series model (which is actually Reuss' transverse-loading rule of mixtures [183]), with an error of 1.9%. This was in agreement with the fact that the longest Ag-coated SnO<sub>2</sub> nanowires tend to bend and run mostly parallel to the film's surface and perpendicular to the indentation load direction.

**Table 4.2** Results of the calculation of the composite's Young's modulus from different models based on the rule-of-mixtures, together with their deviation from the measured values.

Model	$E$ (GPa)	Error (%)
Parallel (Voigt)	143.8	5.9
Series (Reuss)	138.4	1.9
Effective-medium theory	142.6	5.0
Maxwell	142.6	5.0
Hamilton	143.3	5.5
Reciprocity	141.5	4.2
Average values	142.0	4.6

#### 4.3.2.3 Evaluation of the stress-strain relationship from nanoindentation data

The application of standard bulk-material methods for measuring the stress-strain ( $\sigma$ - $\varepsilon$ ) relationship in thin films has proved to be a highly complex task. As a consequence, big efforts have been made to develop procedures for extracting the elastoplastic properties of ductile materials from nanoindentation experiments [184–188]. Such attempts usually involved dimensional analysis and finite-element simulations which, assisted by theoretical and experimental investigations, provided analytical expressions which linked nanoindentation data to the uniaxial  $\sigma$ - $\varepsilon$  behaviour of materials. One disadvantage of these methods is that their application is not straightforward. They normally involve several complex calculation steps which must be performed for each individual indentation performed on the samples. Moreover, these techniques consider only load-displacement curves whose unloading starts immediately upon reaching maximal force. This ignores those measurements which incorporate constant-load times (mostly for creep effects), which are quite standard procedures (like the one employed in this work).

Then, for evaluating the tensile properties of the studied films, a method based on the results from Ma et al. [184] regarding finite-element simulations of Berkovich-indentation experiments was employed. Assuming a power-law work-hardening behaviour of polycrystalline metals, the response to uniaxial tension is given by:

$$\sigma = \begin{cases} E\varepsilon, & \text{for } \sigma \leq \sigma_y \\ K\varepsilon^n = \sigma_y^{1-n}(E\varepsilon)^n & \text{for } \sigma \geq \sigma_y, \end{cases} \quad (4.3)$$

where  $\sigma_y$  denotes the starting yield strength,  $K$  is a constant and  $n$  is the work-hardening coefficient ( $0 < n < 1$ ). The latter lies normally, for metals, between 0.2 and 0.5 (a higher  $n$  means greater work-hardening capacity). However, it can be much lower in the case of dislocation-saturated microstructures, such as those found in nanocrystalline metals processed by severe plastic deformation. For this analysis,  $\sigma$  and  $\varepsilon$  refer to true (rather than engineering) stress and strain. Fitting their simulation results, Ma et al. found that

$$(H/\sigma_y) = (1.76 - 3.7n + 2.52n^2)(\sigma_y/E)^{(-0.073-0.96n)}, \quad (4.4)$$

which we would use later to calculate  $\sigma_y$ . To this end, only  $n$  remained unknown, since the values of  $H$  and  $E$  were already available from the nanoindentation measurements. Several authors have developed different models relating  $n$  to both the indenter's maximum displacement ( $h$ ) and the depth of contact of the indenter with the sample ( $h_c$ ) [189–191]. As explained in Fig. 3.6,  $h$  and  $h_c$  are likely to differ because of pile-up/sink-in effects. In the present work, the solution from Hill et al. [191] based on the plastic deformation theory was adopted, in view that it showed very good agreement with the simulations of Ma et al. along the whole range of values of  $n$  analysed in their paper [184]. This model is given by:

$$h_c/h = [5(2 - n)]/[2(4 + n)]. \quad (4.5)$$

The values of  $h$  and  $h_c$  used here to calculate  $n$  with Eq. 4.5 were direct and derived results, respectively, from the nanoindentation experiments (as described in 3.2.7). Then,  $\sigma_y$  was finally calculated for each material by using Eq. 4.4. The calculated values of  $n$  and  $\sigma_y$  are listed in Table 4.3, together with other relevant parameters related to the plastic behaviour of the films. The corresponding  $\sigma$ - $\varepsilon$  curves are shown in Fig. 4.11.

**Table 4.3** Parameters associated to the plastic behaviour of the films under uniaxial tension (given by Eq. 4.3), which were calculated from indentation data. Standard deviation values are listed in brackets.

	$K$ (GPa)	$n$	$\sigma_y$ (MPa)	$\sigma_{0.2\%}$ (MPa)	$\sigma_{8\%}$ (MPa)
Ni-Ag-SnO <sub>2</sub>	5.01	0.42 (0.00)	444 (26)	587	1719
Ni <sub>cg</sub>	2.44	0.36 (0.01)	226 (1)	332	978
Ni <sub>fg</sub>	5.88	0.42 (0.01)	510 (15)	687	2046

The  $\sigma_y$  of Ni-Ag-SnO<sub>2</sub> showed a 96% increment with respect to Ni<sub>cg</sub> due to grain-boundary strengthening. On the other hand, a 13% reduction with respect to Ni<sub>fg</sub> was observed, explained by the softening induced by the presence of weaker phases (Ag and porosity). This scenario was analogous to that previously observed for the  $H$ . However, the composite films performed relatively better in terms of  $\sigma_y$  than in terms of  $H$ , when using the Ni samples as comparison reference. This was evidenced by the larger increment with respect to the softer Ni<sub>cg</sub> (96 vs 66%) and the smaller reduction with respect to the stronger Ni<sub>fg</sub> (13 vs 17%). The reason behind this was the detrimental effect of the lower  $E$  of the composite on its  $H$ . The larger amount of elastic deformation would result in an increased contact area of the indenter with the sample, thus reducing the contact pressure which defines its  $H$ .

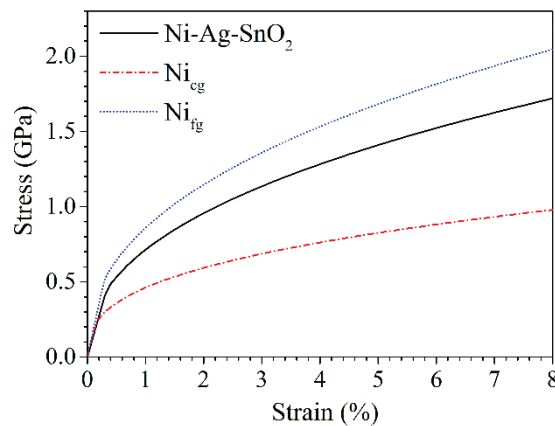


**Fig. 4.11** Strain-stress curves of the investigated films derived from nanoindentation data.

Tabor established that for materials which do not experience work-hardening (i.e., perfectly plastic,  $n \sim 0$ )  $\sigma_y = 3H$  [192]. For the case of work-hardening metals ( $n > 0$ ), he suggested that  $\sigma_y$  should be replaced in that relationship by the flow stress at a representative strain of 8 to 10%, which would also represent a fairly good approximation to the ultimate tensile

strength [161,192,193]. The stress corresponding to a representative strain of 8% ( $\sigma_{8\%}$ ) was calculated for the samples under study using Eq. 4.3 and is listed in Table 4.3. The ratio between  $H$  and  $\sigma_{8\%}$  ranged between 2.58 and 2.74, showing consistency with Tabor's relationship. Moreover, Cheng and Cheng showed that when  $\sigma_y/E < 0.02$  (as in this work), the ratio between  $H$  and the stress corresponding to Tabor's representative strain should range between 2.4 and 2.8 [194], what further supports the results here obtained.

Finally, the Hall-Petch relationship was analysed, now in terms of  $\sigma_y$ . It is expressed by Eq. 4.1, replacing  $H$ ,  $H_0$  and  $k_H$  with their analogues  $\sigma_y$ ,  $\sigma_{y0}$  and  $k_y$ , respectively. The experimental data was accurately fitted with linear curves, as shown in Fig. 4.12, confirming the Hall-Petch behaviour of the films. This was expected due to the fact that grain-boundary strengthening was believed to govern their mechanical response. A weaker dependency of  $\sigma_y$  on the grain size was found for the Ni-Ag-SnO<sub>2</sub> (indicated by a lower  $k_y$  with respect to that of pure Ni). This suggested the activity of other mechanisms in the behaviour of the composite, which partially reduced the degree of grain-boundary strengthening. This situation is equivalent to that observed in the case of the  $H$ , which was already discussed at the end of 4.3.2.1. The value of  $k_y$  calculated for the Ni samples (7.3 GPa·nm<sup>0.5</sup>) was in good agreement with results from other authors, which usually range between 5.7 and 7.6 GPa·nm<sup>0.5</sup> [175].

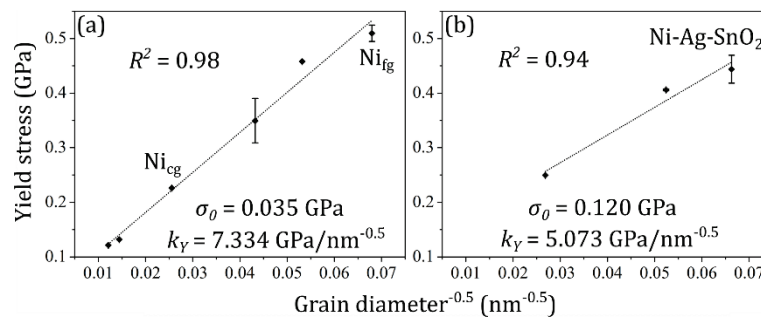


**Fig. 4.12** Hall-Petch plots from the yield stress of (a) pure-Ni and (b) Ni-Ag-SnO<sub>2</sub> films. The error bars are given by the standard deviation.

#### 4.4 Conclusions

Ni-Ag-SnO<sub>2</sub> composite films were successfully produced using the proposed fabrication procedure, which combined the CVD, electroless and electrodeposition techniques. Their microstructure and mechanical properties were investigated, together with those from two

types of pure-Ni films (coarse and fine-grained) for comparison and analysis purposes. The main results here obtained are summarised next.

- The Ni-Ag-SnO<sub>2</sub> presented a gradient microstructure with decreasing content of the secondary phases towards the surface. Its  $d_A$  was reduced by 85% with respect to the similarly deposited Ni<sub>cg</sub>, as a result of grain-boundary pinning by the Ag-SnO<sub>2</sub> phase during the electrodeposition of the matrix.
- Nanoindentation experiments revealed an increase in the composite's  $H$  of 66% with respect to Ni<sub>cg</sub>, as a result of grain-boundary strengthening. However, a 17% reduction was observed with respect to Ni<sub>fg</sub> (having similar  $d_A$ ), which was attributed to the presence of the softer Ag component and porosity.
- The pure-Ni samples showed reduced values of  $E$  (163-177 GPa) with respect to bulk Ni (200 GPa). This was likely caused by a limited mass transport of Ni ions during the electrodeposition, which could result in less dense coatings. The even lower  $E$  of the composite (136 GPa) was accurately modelled using several variants of the rule of mixtures, confirming that the weaker Ag phase was the main reason behind said reduction.
- A straightforward method based on analytical and simulation results from several works available in the literature was proposed for characterising the  $\sigma$ - $\varepsilon$  response of the materials from indentation data. Similarly as observed for the  $H$ , the calculated  $\sigma_y$  of the Ni-Ag-SnO<sub>2</sub> was 96% higher and 13% lower than those of Ni<sub>cg</sub> and Ni<sub>fg</sub>, respectively.
- Both  $H$  and  $\sigma_y$  of the studied materials satisfied the Hall-Petch relationship. The lower slopes in the curves of the composite indicated that other mechanisms besides grain-boundary strengthening influenced its mechanical response.

# 5 Analysis of the dry-sliding friction and wear behaviour

## 5.1 Introduction

The use of films and coatings is a matter of great interest for tribologists, since it allows improving the performance of materials which operate under the influence of friction and wear phenomena. Countless engineering applications profit from this, such as cutting tools, electrical contacts, magnetic recording devices, biomedical components and microelectromechanical systems [195]. This is true not only for moving parts but also for nominally stationary couples which undergo normal and tangential micromotion during operation. Such conditions may promote all sorts of degrading processes at the involved surfaces, such as deformation, wear, oxidation and corrosion.

The influence of the microstructure on the tribological properties of diverse films is a widely investigated topic. Special attention is usually paid to the role of grain size on the mechanical strength, since the hardness of materials largely determines their friction and wear behaviour [8,157,196,197]. As mentioned in the previous chapter, the relationship between strength and grain size was firstly mathematically described by Hall and Petch [150,151]. Ni-based films have been frequently subject of these studies due to their high technical relevance, which is given by their superb mechanical and tribological properties as well as remarkable corrosion and oxidation resistance [52,53,147,198].

The work presented in this chapter aimed to evaluate the tribological behaviour of the Ni-Ag-SnO<sub>2</sub> composite and to gain an understanding of the role played by its constituents. Again, two sets of pure Ni-films were also studied: (i) one which was deposited using the same bath and experimental parameters as for the composite's matrix; and (ii) another possessing a hardness similar to that of Ni-Ag-SnO<sub>2</sub>, which was achieved through grain refinement. The former served as comparison reference, allowing to assess the net effect of introducing the Ag-SnO<sub>2</sub> phase. The latter provided information on whether the reinforcement induced any other effects, other than grain-boundary strengthening, which could have influenced the tribological response of the composite.

Friction and wear were evaluated in dry-sliding conditions (i.e., without lubrication) in ambient air, using a linearly reciprocating ball-on-flat experimental setup. Such configuration

simulated the fretting type of wear (i.e., surfaces contacting during small-amplitude reciprocating motion) experienced by the electrodes of electrical-contact devices. Diamond was employed as counter-body material, aiming to avoid any material transfer towards the samples. This would simplify the interpretation of results and reduce the number of variables for consideration when modelling the system's behaviour, providing a deeper understanding on a fundamental basis.

## 5.2 Experimental details

The Ni-Ag-SnO<sub>2</sub> composite films were produced as described in 3.1. Two sets of pure-Ni films were used for comparison and analysis purposes, denominated coarse-grained (Ni<sub>cg</sub>) and fine-grained (Ni<sub>fg</sub>) Ni. They were deposited using the same bath and experimental parameters as for the composite's matrix, with the only addition of the grain refiner saccharin (< 0.1 g/l) in the case of Ni<sub>fg</sub>, in order to obtain a hardness similar to that of the composite.

The evaluation of the mechanical properties and tribological behaviour of the samples was carried out according to the procedures described in 3.2.7 and 3.2.8, respectively.

## 5.3 Results and discussion

The hardness ( $H$ ) and Young's modulus ( $E$ ) of the studied samples obtained by nanoindentation are listed in Table 5.1, together with their grain size and surface roughness ( $R_q$ ). The basic outputs of the tribometer from the friction and wear tests were the mean dynamic-friction coefficient ( $\mu$ ) and the mean normal displacement of the ball (i.e., penetration depth) at each cycle. These results are displayed in Fig. 5.1 and 5.2, respectively, and are the basis of the analysis in following sections.

**Table 5.1** Area-weighted average grain diameter, mechanical properties and roughness of the samples, obtained by EBSD, nanoindentation and WLI, respectively (with the standard deviation in brackets).

	Ni-Ag-SnO <sub>2</sub>	Ni <sub>cg</sub>	Ni <sub>fg</sub>
Grain diameter (nm)	228 (7)	1436 (455)	353 (15)
$H$ (GPa)	4.5 (0.3)	2.6 (0.2)	4.7 (0.3)
$E$ (GPa)	136 (14)	143 (8)	153 (21)
$R_q$ (nm)	16 (7)	20 (6)	9 (1)

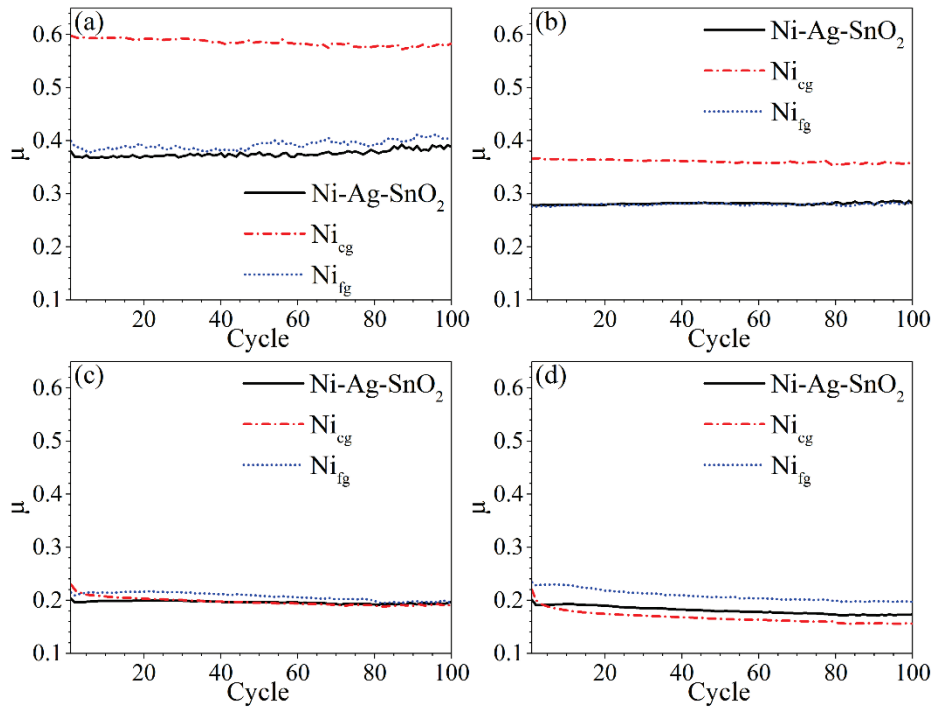


**Fig. 5.1** Evolution of  $\mu$  for the tests at  $F$  of (a) 5, (b) 10, (c) 20 and (d) 30 mN.

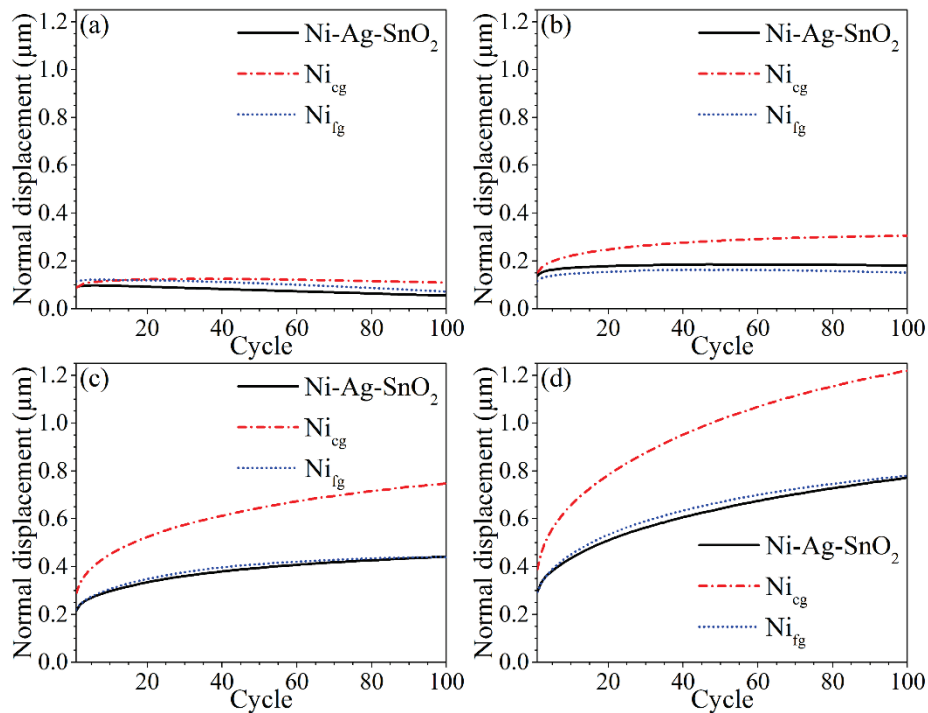


**Fig. 5.2** Mean normal displacement (i.e., penetration depth) of the sliding ball for the tests at  $F$  of (a) 5, (b) 10, (c) 20 and (d) 30 mN.

### 5.3.1 Analysis of the wear tracks and subsurface microstructure

Typical wear tracks for each type of sample tested are shown in Fig. 5.3 and 5.4. The relatively smooth worn surfaces, characterised by the absence of cracks, large detached parts or any other sign of delamination (all associated to adhesion), indicated a predominantly abrasive wear process, which produced quite similar features on the three systems under study. According to the wear debris produced and the behaviour of  $\mu$ , Kayaba et al. classified this type of wear into four categories: cutting, flaking, wedging and ploughing [199]. Considering the description given by them for each case, the absence of evident wear debris (the films were not cleaned after the tests); the formation of well-defined grooves, with ridges at both sides; and the practically constant values of  $\mu$  (see Fig. 5.1) clearly indicated the occurrence of ploughing-type wear in the performed tests. For large loads ( $F$ ), i.e., 20 and 30 mN, fragmented material pieces (microchips) could be noticed at side ridges (Fig. 5.4), which were sign of a certain degree of cutting wear. The ploughing of a hard abrasive body against a softer surface may cause the partial detachment of chips by cutting. The chip formation usually comes together with a heavy plastic deformation (both at ridges and under the groove) and changes in the microstructure of the near-surface layer [200]. This suggested also a shift towards a more brittle wear behaviour, caused by the local work-hardening of the films during sliding [198]. The formation of a brittle oxide tribolayer (discussed later in this section) could have also contributed to this.

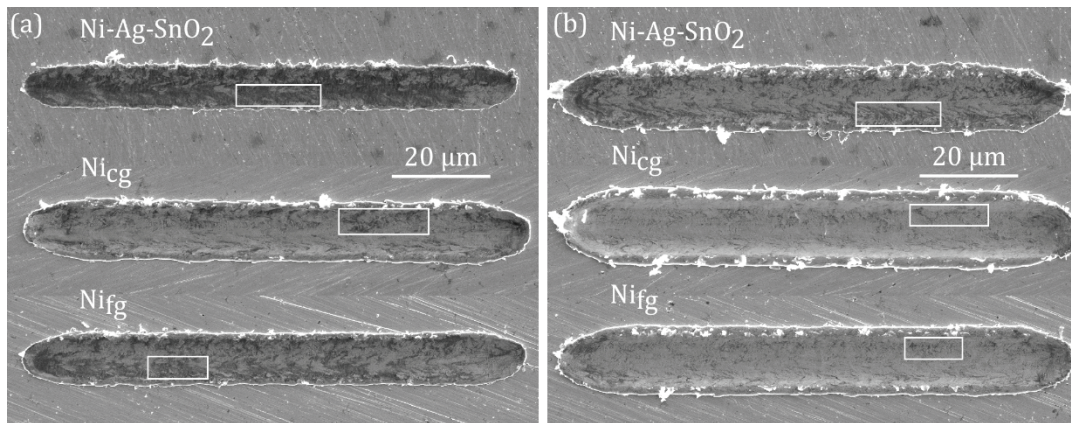


**Fig. 5.3** SEM micrographs showing wear tracks from all the types of samples under study for the tests at (a) 20 and (b) 30 mN. The white rectangles show examples of dark spots corresponding to oxygen-rich tribolayers.

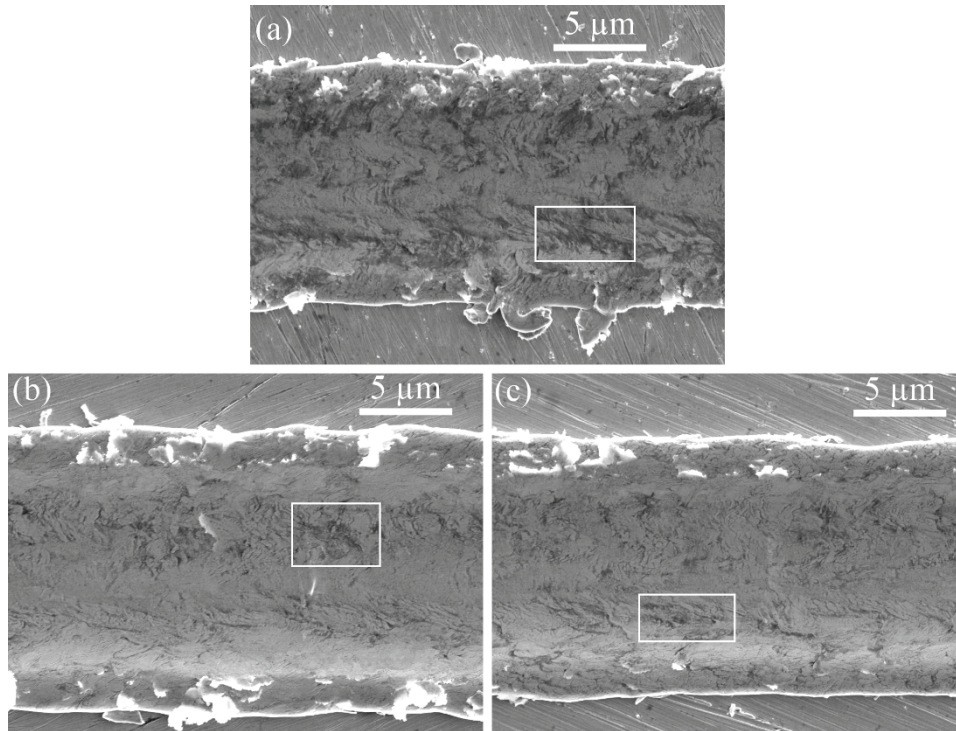


**Fig. 5.4** SEM micrographs showing the groove and side ridges of wear tracks produced at  $F = 30$  mN on (a) Ni-Ag-SnO<sub>2</sub>, (b) Ni<sub>Cg</sub> and (c) Ni<sub>Jg</sub>. The white rectangles show examples of dark spots corresponding to oxygen-rich tribolayers.

In order to assess the magnitude of this possible shift towards a cutting-wear mode, the Zum Gahr's cutting-efficiency parameter ( $f_{AB}$ ) was calculated. It is given by

$$f_{AB} = (A_B - A_A)/A_B, \quad (5.1)$$

where  $A_A$  and  $A_B$  are the areas of the side ridges (above the surface) and the groove (below the surface), respectively, from a cross-section of a wear track, perpendicular to the sliding direction. It follows from this definition that ideal microploughing results in  $f_{ab} = 0$  and ideal microcutting in  $f_{ab} = 1$  [201]. The resulting  $f_{AB}$  values from Eq. 5.1 are listed in Table 5.2, which were calculated from SEM images of several FIB cross-sections. WLI measurements could not be applied here for evaluating the whole wear track (instead of only a few cross-sectional cuts), since this technique is unable to detect the void gap between the side ridges and the underlying surface, artificially increasing  $A_A$ . The very low values of  $f_{AB}$  obtained (though with relatively large standard deviations due to local features) allowed disregarding the weight of the cutting component of wear.

**Table 5.2** Zum Gahr’s cutting-efficiency parameter calculated for all the studied samples. The low values obtained indicate ploughing-type wear behaviour. Standard deviation values are listed in brackets.

	Ni-Ag-SnO <sub>2</sub>	Ni <sub>cg</sub>	Ni <sub>fg</sub>
$f_{AB}$	0.106 (0.104)	0.035 (0.029)	0.005 (0.009)

In the SEM micrographs of Fig. 5.3 and 5.4, regions with markedly different contrast at the worn surfaces suggested the formation of an oxide-containing tribolayer [198]. This was evaluated by means of EDS at the surface of the specimens and the results are displayed in Fig. 5.5. The oxygen concentration at the wear tracks was markedly higher than at the surrounding areas, implying that oxidative wear took place. A brittle oxide layer can form during wear, in air, of ductile metals, which in turn could mix mechanically with non-oxidised metal to form a nanocomposite [202]. For Ni-Ag-SnO<sub>2</sub> and Ni<sub>fg</sub>, the concentration of remaining oxygen reached a maximum after the tests at  $F = 20$  mN and then decreased. This resulted from the increase in the rate of removal of the oxide scale relative to its rate of formation. This was not the case for the Ni<sub>cg</sub> samples, since their softer nature allowed them to accommodate the increasing stresses with more deformation in the load direction, instead of shearing, thus lowering their oxide-removal rate.

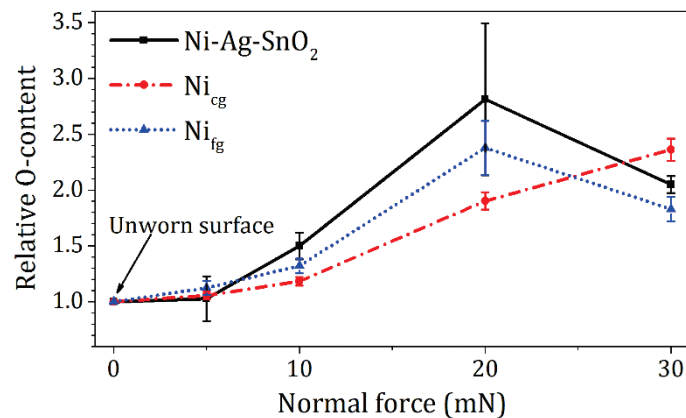


**Fig. 5.5** Oxygen-content measured at the entire surface of the groove of the wear tracks by means of EDS. The values are normalised according to the oxygen-content measured at the unworn surrounding area (0 mN). The error bars are given by the standard deviation.

Flow patterns observed at the surface of the wear tracks were another sign of plastic deformation [202]. A usual analytical approach for determining the likelihood of plastic deformation is given by the evaluation of contact pressures. According to the Hertzian classical solution for the non-adhesive elastic contact between a sphere and a flat surface [203], the maximum contact pressure is given by

$$p_{max} = [(6FE_r^2)/(\pi^3 R^2)]^{1/3}, \quad (5.2)$$

where  $E_r$  is the reduced Young's modulus [144] and  $R$  the radius of the sphere. The values of  $p_{max}$  from the present work are listed in Table 5.3. Even at the lowest  $F$ ,  $p_{max}$  largely surpassed the values of  $H$  from all the samples, corroborating the experimental observations of plastic deformation.

**Table 5.3** Maximum contact pressure according to the Hertzian elastic-contact model, calculated for the investigated samples and experimental conditions.

$F$ (mN)	$p_{max}$ (GPa)			
	5	10	20	30
Ni-Ag-SnO <sub>2</sub>	8.0	10.0	12.6	14.5
Ni <sub>cg</sub>	8.2	10.3	13.0	14.9
Ni <sub>fg</sub>	8.5	10.8	13.6	15.5

It can be observed in Fig 5.6 that also the subsurface microstructure of the films was affected during the wear tests. The softer Ni<sub>cg</sub> displayed the most extended variation in grain morphology, reaching about 2 μm underneath the groove of the wear track. As discussed so far, the frictional energy of two bodies sliding against each other can be dissipated by plastic deformation, whose working mechanism is based on slip processes within grains, that shift crystal planes relative to each other, shearing plastically the material [204]. Another possibility is the dissipation of energy in form of heat. Under certain conditions, this could lead to a spread or local rise in the temperature at the near-surface. Such thing could in turn induce thermally activated phenomena such as dynamic recrystallization (highly relevant for tribology [205–210]) or creep. These effects could also account for the observed changes in the near-surface grain structure.

For low-speed sliding, a low temperature and negligible thermal effects are normally assumed. However, signs of phase transformations (characteristic of high temperatures) can also be found in such experiments [211]. This could be explained by considering the flash

temperature, which is defined as the highest temperature which appears close to the areas of true contact (where energy is dissipated) [212–217]. It is normally expressed as the temperature difference with respect to the bulk,  $\Delta T_{flash}$ , which was evaluated for the present experiments by applying several models from different authors [217–220]. The results of this, listed in Table 5.4, showed that the increase in temperature during the tests was negligible, mostly as a consequence of the very low sliding speed. Accordingly, the resulting homologous temperature of 0.17 disregards the possibility of activation of the mentioned temperature-dependent phenomena, since a value of at least 0.3 is required in the case of Ni [204,221]. However, fine microstructures possess a very high density of defects, which could in turn reduce considerably the dynamic recrystallization temperature. This is usually accompanied by pronounced variations in the evolution of  $\mu$ , which was clearly not the case here. These observations suggest that plastic deformation was responsible for the microstructural changes observed underneath the wear tracks.

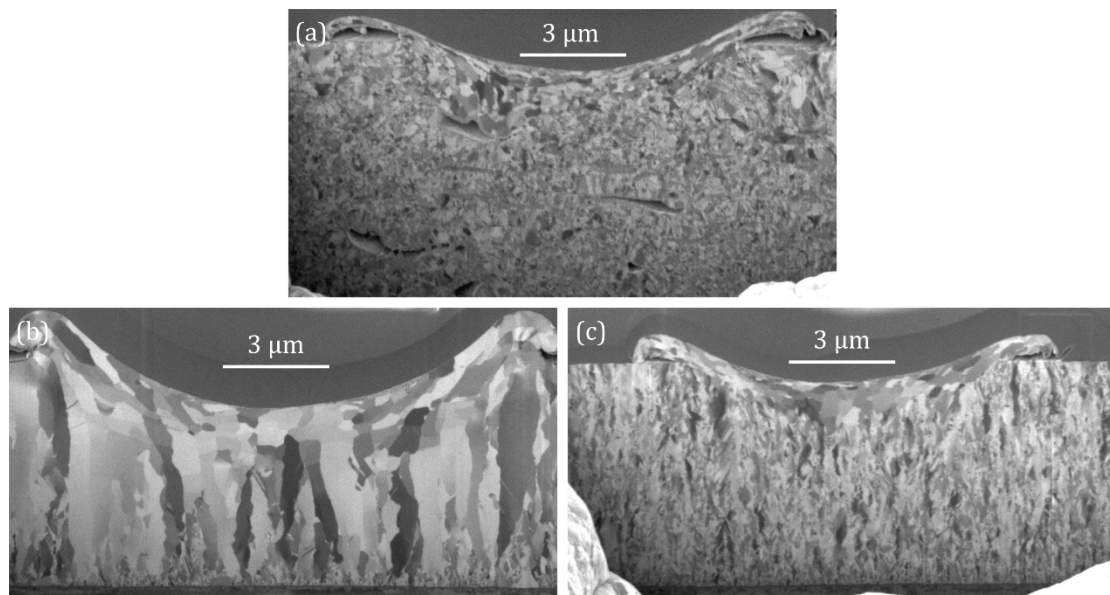


**Fig. 5.6** FIB ion-channelling-contrast images from the cross-sections of wear tracks produced at  $F = 30$  mN on (a) Ni-Ag-SnO<sub>2</sub>, (b) Ni<sub>cg</sub> and (c) Ni<sub>fg</sub>. In each case, a layer of plastically deformed grains is observed directly underneath the surface.

The idea behind using several flash temperature models was to reduce the uncertainty given by their differing physical, dynamic and geometrical assumptions [211]. It should be also noted that such models tend to underestimate the temperature rise, since they do not incorporate several influential factors such as chemical effects, the evolution of mechanical properties during sliding and the variation of the thermal conductivity with temperature.

**Table 5.4** Estimation of flash temperatures for the performed tests, expressed as the temperature difference between the hot real-contact areas and the bulk, according to different models available in the literature [217–220].

	Kuhlmann-W.	Archard	Holm	Rabinowicz
$\Delta T_{flash}$ (K)	$6.4 \times 10^{-6}$	$2.4 \times 10^{-5}$	$2.7 \times 10^{-5}$	$2.0 \times 10^{-3}$

Moreover, many contact parameters are usually neglected, such as the random roughness, size and shape of the real contact area as well as the geometry and thermal properties of wear particles [214]. In order to somehow compensate for this, the selected models were stress tested by inflating the involved parameters (e.g., thermal conductivity, contact area and  $\mu$ ) up to values way beyond what could be considered physically reasonable. That resulted in an increase in  $\Delta T_{flash}$  of up to some orders of magnitude but, in all cases, remaining under 1 K due the extremely low initial values.

### 5.3.2 Analysis of the dynamic friction coefficient

The study of the  $\mu$  evolution curves (Fig. 5.1) revealed different patterns: (i) steady-state values were reached already after a short number of cycles, with no substantial variation along the whole duration of the tests; (ii) at low  $F$  (5 and 10 mN), the softer Ni<sub>cg</sub> exhibited higher  $\mu$  than the harder Ni<sub>fg</sub> and Ni-Ag-SnO<sub>2</sub> films; and (iii) a general dependence of  $\mu$  on  $F$  for all the studied samples.

The first pattern was already addressed in the previous section and was attributed to the observed ploughing-type abrasive wear. The largest material removal occurred already during the first cycle, achieving rapidly an almost steady-state surface condition, which was followed by a relatively low wear rate (even negligible for low  $F$ ). This can be better understood by observing Fig. 5.2, which shows that a very large fraction of the total penetration depth (relatable to the wear volume) was reached upon contact during the initial cycle. This first cycle represented the run-in period, which is commonly defined as the transition during which the surface is plastically deformed into a steady-state condition and a stable wear rate is achieved.

The second pattern is widely discussed in the literature and relates to the dependence of  $\mu$  on  $H$ , which was the case for the tests at low  $F$  (5 and 10 mN). In metals,  $\mu$  usually increases

with decreasing  $H$ . Softer surfaces are more prone to deform plastically and more susceptible to adhesion, which in turn favours the formation of asperity junctions [52,222,223]. Larger grains are also associated to higher values of  $\mu$ , but that is the result of the Hall-Petch effect by which they exhibit lower  $H$  [8]. However, at higher  $F$  (20 and 30  $\mu\text{m}$ ),  $\text{Ni}_{\text{cg}}$  displayed approximately the same  $\mu$  (about 0.2) as the harder  $\text{Ni}_{\text{fg}}$  and  $\text{Ni-Ag-SnO}_2$ . This behaviour resulted from the work hardening during the high plastic deformation of the first cycles (run-in stage), which hardened the surfaces and thus reduced their ductility [198,224]. Moreover, the higher oxygen content observed after the 20 and 30 mN tests (Fig. 5.5) could have also played a role. Oxide tribolayers are well-known for providing a lubricating effect due to their low shear strength and reduced ductility, which depends on different factors such as their thickness, cohesion and attachment to the underlying material [53,198,203,223,224]. However, Scharf et al. suggested that this would not be the case for  $\text{NiO}$ , but rather the opposite [225].

The third and final pattern was the dependence of  $\mu$  on  $F$  for all samples, which is made clear in Fig. 5.7. Such behaviour contradicts the first of Amontons' empirical laws of friction, which states that the friction force is directly proportional to  $F$ , resulting in  $\mu$  being independent of  $it$ . These laws work very well for dry friction on the macroscopic scale but, nevertheless, such contradicting behaviour has been frequently observed in experiments. Several theoretical models have been developed to explain this. For experimental results similar to those of the present work (decreasing  $\mu$  at higher  $F$ ), the earlier explanations relayed on recrystallization phenomena at higher loads [226] or on the gradual shift of surface asperities from plastic to elastic deformation [227]. The model developed by Rigney and Hirth affirms that steady-state friction forces result from the plastic deformation of the near-surface region, with the confinement of most of the deformation work within cell-type structures [228]. This theory is based on an earlier wear model from Rigney and Glaeser, according to which the ploughing of asperities produces high dislocation densities, leading to the formation of cells [229]. These cells consist of dislocation-free regions delimited by dense networks of entangled dislocations, which develop with increasing strain. The cell walls act as source and sink of dislocations which can freely travel through the cell's core without affecting the microstructure. Depending on the strain rate, this would allow to accommodate much larger strains than the cell-free structure. According to this friction model, a cell layer could not form at low  $F$ , resulting in higher friction forces.

In view of the dimensions of the features observed in these experiments, which developed from the nano to the microscale, the identified dependence of  $\mu$  on  $F$  can be more accurately

explained in terms of scale effects, which are well established in tribology [230–232]. The models from Bhushan and Nosonovsky incorporate the influence of scale effects to the parameters which govern friction [230,233]. Based on the adhesion theory, these parameters are the real area and the shear strength of asperity contacts.

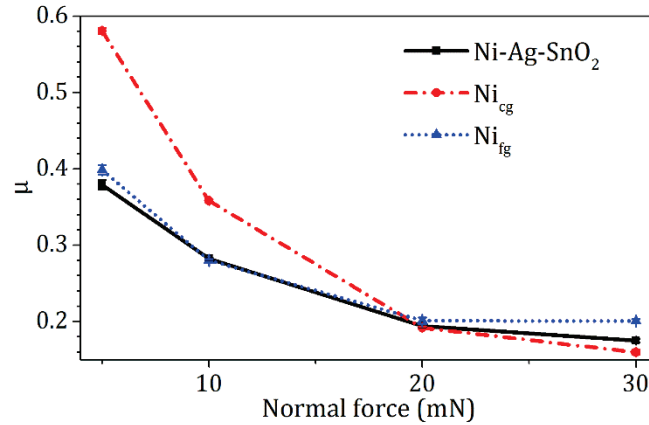


**Fig. 5.7** Steady-state  $\mu$  from all the evaluated samples and test conditions, calculated by averaging the value from the last 50 cycles of each test. The error bars (almost negligible) are given by the standard deviation. A pronounced dependence of  $\mu$  on  $F$  can be clearly observed.

The scale effect on the real area of contact is explained by means of the strain-gradient plasticity theory. According to it, the mechanical properties of materials can vary under the influence of strain gradients, which are accommodated by geometrically-necessary dislocations [234,235]. Then, the smaller the size of an indentation, the larger is the strain gradient and likewise the dislocation density. This results in an increased  $H$ , which in turn reduces the area of contact.

The scale effect on the shear strength of asperity contacts is given by a change in the operating microslip mechanism for sliding. For contact sizes up to few  $\mu\text{m}$ , dislocation-assisted sliding is more energy profitable than the conventional mechanism of concurrent slip with simultaneous breaking of adhesive bonds [236,237]. Accordingly, due to a higher dislocation density at their interface, the shear strength of asperity contacts is reduced with respect to the bulk. Moreover, up to a certain point, the larger the area of contact, the higher the thickness of the interface zone from which dislocations can climb and assist in the microslip. Consequently, the average shear strength of asperity contacts increases with decreasing scale.

Then, according to the above-discussed scale-related phenomena, the behaviour of the friction force is defined by the degree of variation of both the real area and shear strength of asperity contacts. From the different model variations of Bhushan and Nosonovsky, the multi-asperity plastic-contact situation is the one which best describes the contact characteristics of the present experiments. Depending on material parameters, it predicts an increase in  $\mu$  with decreasing scale, which is in agreement with the findings of this work.

### **5.3.3 Analysis and modelling of the wear volume**

The wear volume ( $W$ ) is the amount of material removed due to wear during a tribological test, which is a parameter commonly used to quantify and compare the wear resistance of materials. In the present work, WLI was used for measuring  $W$ , which corresponded to the volume of the wear track's groove. Special care must be taken when applying this technique, since image artefacts in form of jumps or spikes might distort the results. Such features were hardly present in the recorded surface profiles, thus having no real impact in the reliability of the measurements. Then, the resulting  $W$  values are displayed in Fig. 5.8. The composite exhibited a much higher wear resistance than  $\text{Ni}_{\text{cg}}$ , which was deposited using the exact same bath and deposition parameters as the composite's matrix. This was evidenced by a significant reduction in  $W$ , which ranged between 52 and 74%. The reason behind this was the higher  $H$  of  $\text{Ni-Ag-SnO}_2$ , since the similarly hard  $\text{Ni}_{\text{fg}}$  produced equivalent results. These findings, together with the fact that all the studied materials displayed the same type of friction and wear behaviour, suggest that the effect of the  $\text{Ag-SnO}_2$  phase in the tribological response of the composite is given exclusively by the induced grain-boundary strengthening. Because of their low content, the  $\text{Ag-coated SnO}_2$  nanowires did not produce any qualitative changes in the friction and wear behaviour of the films. Moreover, any possible influence from the soft, lubricating nature known to  $\text{Ag}$  could have been neutralised by the high contact pressures involved, which might have led to the mechanical overstressing of the films.

Back in the middle of the 20<sup>th</sup> century Archard established that for sliding wear

$$W = k(Fx/H), \quad (5.3)$$

where  $k$  is the wear coefficient (dimensionless) and  $x$  is the sliding distance [238,239]. The model of Eq. 5.3 can be analytically derived from both the adhesive and abrasive traditional wear mechanism theories. Since the time of its formulation, several variations and other new models have been developed [240,241]. Nevertheless, Archard's original model has remained frequently used over the years for the qualitative and quantitative characterisation

of wear [222,242,243]. A typical application of Archard's theory is the use of Eq. 5.3 for calculating  $k$ , which is a measure of the severity of wear. The values of  $k$  from the present experiments are listed in Table 5.5. In all cases was  $k \geq 10^{-4}$ , which corresponds to severe wear [223].

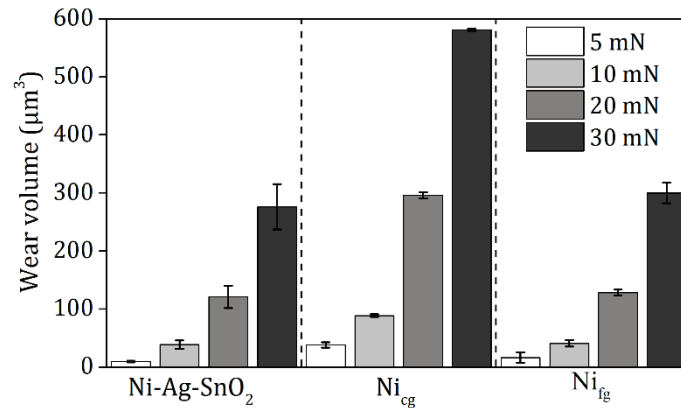


**Fig. 5.8**  $W$  from all the evaluated samples and test conditions, obtained by means of WLI. The error bars are given by the standard deviation.

**Table 5.5** Evaluation of the parameter  $k$  from Archard's model for the performed tests. In all cases, the values of  $k$  indicated the occurrence of severe wear ( $k \geq 10^{-4}$ ).

$F$ (mN)	$k$ ( $\times 10^{-4}$ )			
	5	10	20	30
Ni-Ag-SnO <sub>2</sub>	4.4	8.7	13.5	20.5
Ni <sub>cg</sub>	9.9	11.6	19.3	25.2
Ni <sub>fg</sub>	7.8	9.7	15.2	23.6

The parameter  $k$  is not a fixed material property. It relates  $W$  to a specific combination of  $F$ ,  $x$  and  $H$  for a certain material and experimental setup [244]. Therefore, Eq. 5.3 cannot be used to predict the response to wear of a given tribosystem unless two of its three variables are fixed and  $k$  is known. By combining and processing all the collected data from the performed wear tests, an attempt was made to develop a numerical model of  $W$  based on Eq. 5.3, which could be able to describe the behaviour of the tribosystems under study and provide valuable information for their analysis. The processing of the experimental data was partitioned into pure-Ni and composite samples, since different behaviours could be expected from different type of materials, even when they possessed similar mechanical properties. In order to obtain additional experimental data from Ni films, more samples were

produced with different grain sizes, resulting in also different  $H$ . This was achieved by using different concentrations of saccharin in the electroplating bath and through annealing. In the case of Ni-Ag-SnO<sub>2</sub>, larger grain sizes were obtained also by annealing. In all cases, the annealing treatments were performed as described in 3.1.4.

The first step of the modelling process was to determine the relation between  $W$  and  $H$ . In view of their inverse proportionality expressed in Eq. 5.3, lineal functions of negative slope were proposed to describe their relationship. As observed in Fig. 5.9, an accurate fitting was obtained, leading to the following expression:

$$W = AH + B, \quad (5.4)$$

where  $A$  and  $B$  are the slope and intercept, respectively, of the linear fit functions. Since  $A$  and  $B$  clearly changed with the applied  $F$ , the next step was to quantify this dependence in order to incorporate the effect of  $F$  into the model. Fig. 5.10 shows the result of this process. Linear functions were used once again, since that would lead to the linear dependence of  $W$  on  $F$  described by Archard. Consequently,

$$A = a_1 + a_2F \quad (5.5a)$$

and

$$B = b_1 + b_2F, \quad (5.5b)$$

where  $a_i$  and  $b_i$  are the coefficients of the linear fit functions, whose values are listed in Table 5.6 for both types of materials. Then, Eq. 5.4 can be rewritten in terms of  $H$  and  $F$ , by using Eq. 5.5, as

$$W = (a_1 + a_2F)H + b_1 + b_2F. \quad (5.6)$$

The final step of the analysis was the incorporation of  $x$  into the model. According to the relevant ASTM norm,  $x = 2L\eta$  [245], where  $L$  is the length of the wear track and  $\eta$  the total number of cycles of the test. Due to the unsteady nature of the wear rate, the incorporation of  $\eta$  into Eq. 5.6 would require the definition of new functions relating  $\eta$  to both  $a_i$  and  $b_i$ . Given the complexity of determining such threefold relationship and the lack of the required experimental data (i.e., several hundreds of repeats for different values of  $\eta$ ), the modelling process was simplified by fixing  $\eta$  at 100, which was the value adopted in all the performed wear tests. Under this condition, it is reasonable to assume that varying  $L$  (100  $\mu\text{m}$  for these experiments) would not affect the nature of Eq. 5.6, resulting only in  $W$  changing in the same

proportion. For instance, if  $L$  were to be doubled, it would be the same as performing two times the same test over different (but contiguous) areas, resulting in  $W$  being also doubled. For this to be certainly true, the sliding speed should not differ significantly from the one used in the analysed tests. Doing otherwise could result in a qualitative change in the tribological behaviour of the materials.

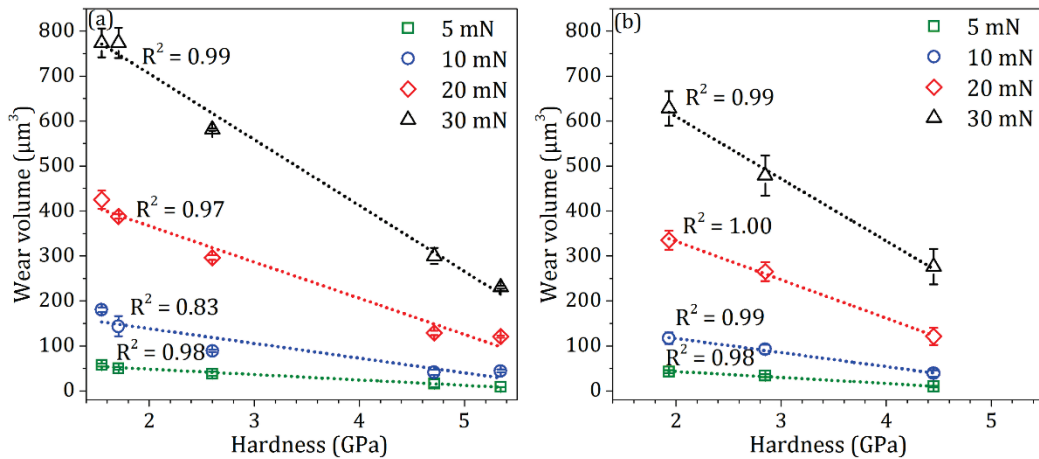


**Fig. 5.9** Linear dependence of  $W$  on  $H$  for the (a) pure-Ni and (b) composite films. The error bars are given by the standard deviation.

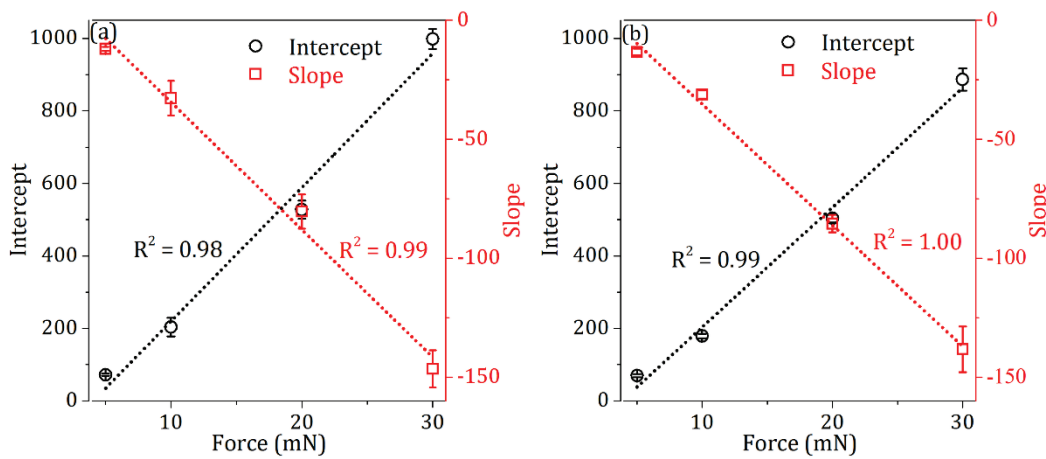


**Fig. 5.10** Linear dependence on  $F$  of both the slope and intercept from Eq. 5.4 ( $A$  and  $B$ , respectively), which describes the linear relationship between  $W$  and  $H$  for (a) pure-Ni and (b) composite films. The error bars are given by the standard error in the calculation of  $A$  and  $B$  using the fit functions of Fig. 5.9.

Then, Eq. 5.6 was modified accordingly, obtaining the final version of the model:

$$W_{100} = [(a_1 + a_2F)H + b_1 + b_2F](L/100), \quad (5.7)$$

where the subscript in  $W_{100}$  denotes the fixing of  $\eta$  at 100 and the right term (outside the square brackets) indicates the proportion of a chosen  $L$  to the reference value of 100  $\mu\text{m}$ .

In order to calculate the value of  $W_{100}$  in  $\mu\text{m}^3$  by using Eq. 5.7, the selected  $F$ ,  $H$  and  $L$  must be computed in mN, GPa and  $\mu\text{m}$ , respectively, together with the values of  $a_i$  and  $b_i$  from Table 5.6. It should be also possible to apply this model for values of  $F$  and  $H$  outside the ranges used in the present experiments, as long as no qualitative change in the wear mode occurs (and thus neither in the observed tendencies). Fig. 5.11 shows the dependence of  $W_{100}$  on  $F$  and  $H$  according to Eq. 5.7. The average error of the model with respect to the experimental values showed a large discrepancy at  $F = 5$  mN (92%), which gradually decreased for higher values (20, 15 and 5% for 10, 20 and 30 mN, respectively). The reason behind this was the quite constant fluctuations of the measured  $W$  around the linear fit of the model, which had more weight for the smaller values of  $W$ .

**Table 5.6** *Coefficients of the linear fit functions describing the relationships of A and B (from Eq. 5.4) with F, according to Eq. 5.5.*

	$a_1$	$a_2$	$b_1$	$b_2$
Ni-Ag-SnO <sub>2</sub>	15.6	-5.1	-126.8	33.0
Ni	19.2	-5.4	-149.6	36.9

As a concluding remark, even though 100 cycles may seem rather limited for most engineering applications, the obtained results allowed extracting very clear information about up to which extent the analysed variables (namely  $H$  and  $F$ ) affect the wear behaviour of the analysed specimens (e.g.,  $\partial W/\partial F$  or  $\partial W/\partial H$ ). This could be useful, for instance, for roughly determining a range of sustainable loads when targeting specific applications, especially when the same type of ploughing wear is likely to predominate. According to the curves of Fig. 5.2 and the characterisation of the wear track features presented earlier, the nature of the wear process did not change significantly for the different  $F$  applied, but it was the speed at which it took place what was mostly affected. Therefore, it would be reasonable to assume that, for the lower values of  $F$ , the observed behaviours or tendencies are likely to continue for a much larger number of cycles. In the case of higher  $F$ , the wear of some of the films proceeded so fast that a critical fraction of the original thickness was already compromised

after 100 or few more cycles, raising questions about the necessity or possible contribution of longer testing times. For a more thorough evaluation, the outcome of the above presented model should be complemented with the wear rate analysis which is developed in the following sections.

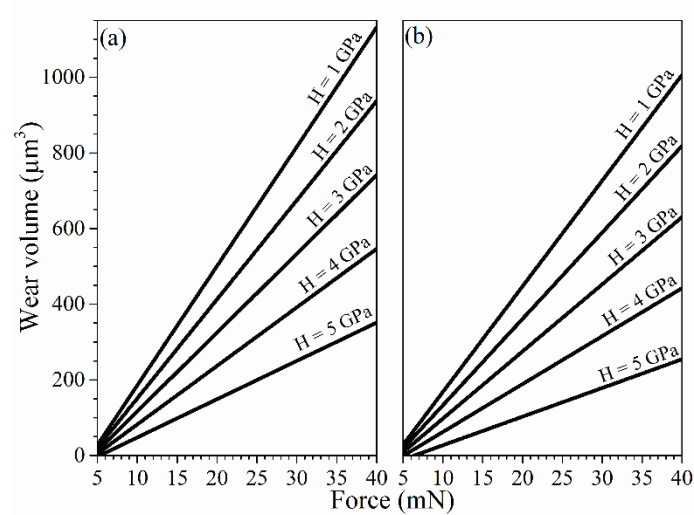


**Fig. 5.11** Results from the  $W_{100}$  model of Eq. 5.7 for (a) pure-Ni and (b) Ni-Ag-SnO<sub>2</sub> films.

### 5.3.4 Modelling and evaluation of the wear rate

Since wear rate normally changes throughout tribological experiments, its determination requires either evaluating its instantaneous value during the whole test or, at least, measuring it upon reaching a steady state after the run-in period. From the available experimental data, the most relevant variable which could be used for such analysis is the normal displacement of the ball ( $D$ ), whose mean value at each cycle was known (as seen in Fig. 5.2). The basic concept behind this was that the deeper the ball ploughed, the higher the resulting  $W$ .

Then, the first step of this modelling process was to find mathematical expressions for the recorded  $D$  curves. Only the tests at 20 and 30 mN were considered, since at lower  $F$  most of the samples exhibited negligible wear after the first cycle (i.e.,  $D$  remained practically constant afterwards, indicating a null wear rate). With each new cycle, the ploughing ball removed decreasing amounts of material. Since this was governed by the work hardening of the films, it was safe to assume that  $D$  behaved also according to this strengthening mechanism. Given the nature of the involved stresses, the most relevant material property in this process was the shear strength. According to the von Mises yield criterion, the shear

strength is proportional to  $H$ , which in turn is proportional to the yield strength, as we know from Tabor's work [192]. Consequently, proportionality could also be assumed for the shear and yield strengths, for which they should display similar behaviour patterns. Following this reasoning, a power-type function was used to fit the experimental data, resembling Hollomon's work-hardening power law (see Eq. 4.3). Accordingly,

$$D = \alpha N^\beta, \tag{5.8}$$

where  $N$  is the cycle number (not to be confused with the total number or amount of cycles,  $\eta$ ) and  $\alpha$  and  $\beta$  are the parameters of the fit function. The resulting values of  $\alpha$  and  $\beta$  for each type of sample and  $F$  under study are listed in Table 5.7. The average error of Eq. 5.8 with respect to the measured values was 0.8%, with an average  $R^2$  of 1.00 (ideal fit). Some examples of the fitted curves are displayed in Fig. 5.12.

**Table 5.7** Parameters of the power functions used for fitting the experimental data concerning the evolution of  $D$  during wear tests (Eq. 5.8).

	Ni-Ag-SnO <sub>2</sub>		Ni <sub>cg</sub>		Ni <sub>fg</sub>	
$F$ (mN)	20	30	20	30	20	30
$\alpha$	0.21	0.25	0.28	0.35	0.22	0.27
$\beta$	0.17	0.24	0.22	0.27	0.16	0.24

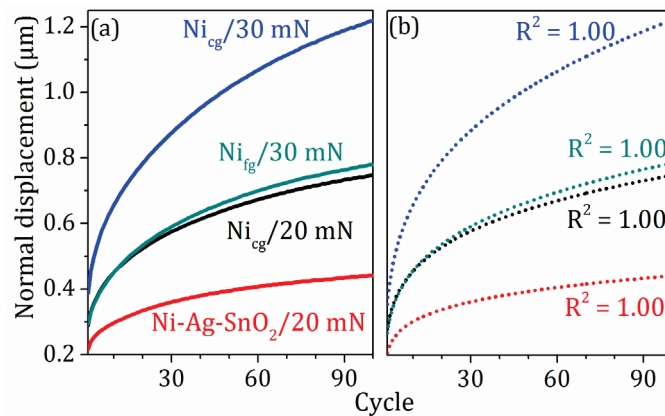


**Fig. 5.12** Examples of (a) measured normal-displacement curves and (b) their respective fitting through simple power-type functions, which are given by Eq. 5.8.

The next step in this analysis was to determine the connection between  $D$  and  $W$ . To that end, it was considered that the cross-section of a wear track should closely resemble the area of a circular segment from a circle of same radius as the ploughing ball. Accordingly,

the height of this circular segment would correspond to the maximum  $D$ . Then, assuming  $W$  to be equal to the volume of the groove of the wear track, this resulted in

$$W = [(4D^2/3)(2R/D - 0.605)^{0.5}]L. \quad (5.9)$$

The term between square brackets is an approximation to the circular-segment area equation, which is multiplied by  $L$  to obtain the desired volume. The use of said approximation allowed greatly simplifying following calculations at the expense of a negligible error with respect to the exact equation (within 0.02% for the values of  $D$  and  $R$  found in this work). Finally, the relation between the experimental measurements of  $W$  and  $D$  was fitted using Eq. 5.9, which is displayed in Fig. 5.13. By adopting a value of  $R$  of 5.8  $\mu\text{m}$  (the real radius of the ball used), the fitting process returned an optimal value of  $L$  of  $96.3 \pm 1.4 \mu\text{m}$ . This was in close agreement with the nominal value of 100  $\mu\text{m}$  from the experiments, thus validating the procedure and assumptions taken so far. Then, by incorporating Eq. 5.8, Eq. 5.9 could be rewritten as

$$W = [(4\alpha^2 N^{2\beta}/3)(2R/(\alpha N^\beta) - 0.605)^{0.5}]L, \quad (5.10)$$

which allows calculating  $W$  after  $N$  cycles. The average error of Eq. 5.10 with respect to the real values of  $W$  obtained by WLI was 3%. Considering that  $N = ft$  [245], being  $f$  and  $t$  the frequency and total time elapsed after  $N$  cycles, respectively,  $W$  could be expressed as a function of time:

$$W = [(4\alpha^2 (ft)^{2\beta}/3)(2R/(\alpha (ft)^\beta) - 0.605)^{0.5}]L. \quad (5.11)$$

Finally, the wear rate as a function of  $N$  or  $t$  was determined by accordingly differentiating Eq. 5.10 and 5.11, resulting in

$$\frac{\partial W}{\partial N} = \frac{4}{3}L\alpha\beta N^{\beta-1} \left[ 2\alpha N^\beta \left( \frac{2R}{\alpha N^\beta} - 0.605 \right)^{0.5} - R \left( \frac{2R}{\alpha N^\beta} - 0.605 \right)^{-0.5} \right] \quad (5.12a)$$

and

$$\frac{\partial W}{\partial t} = \frac{4}{3}L\alpha\beta f^\beta t^{\beta-1} \left[ 2\alpha (ft)^\beta \left( \frac{2R}{\alpha (ft)^\beta} - 0.605 \right)^{0.5} - R \left( \frac{2R}{\alpha (ft)^\beta} - 0.605 \right)^{-0.5} \right]. \quad (5.12b)$$

The curves described by Eq. 5.12a and 5.12b are shown in Fig. 5.14. In agreement with the behaviour of  $D$  observed in Fig. 5.2, the tests exhibited very high initial wear rates, which rapidly decreased until reaching almost constant or steady-state values.

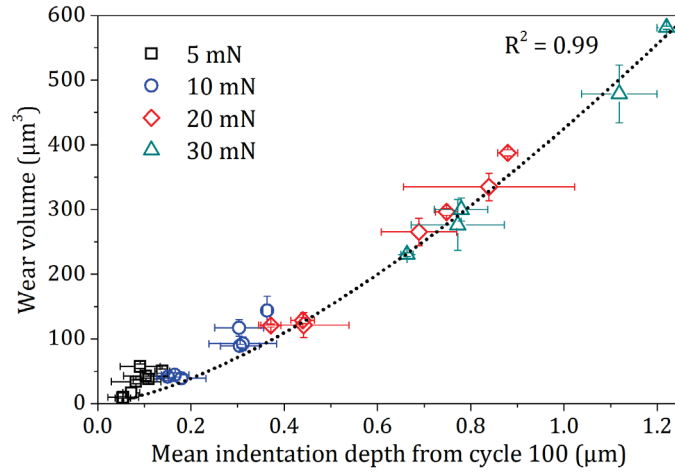


**Fig. 5.13** Correlation between  $W$  and maximum  $D$  (achieved at the end of the wear tests). A function analytically derived from the geometry of both the wear tracks and counter ball (Eq. 5.9) was found to properly describe this relationship. The error bars are given by the standard deviation.

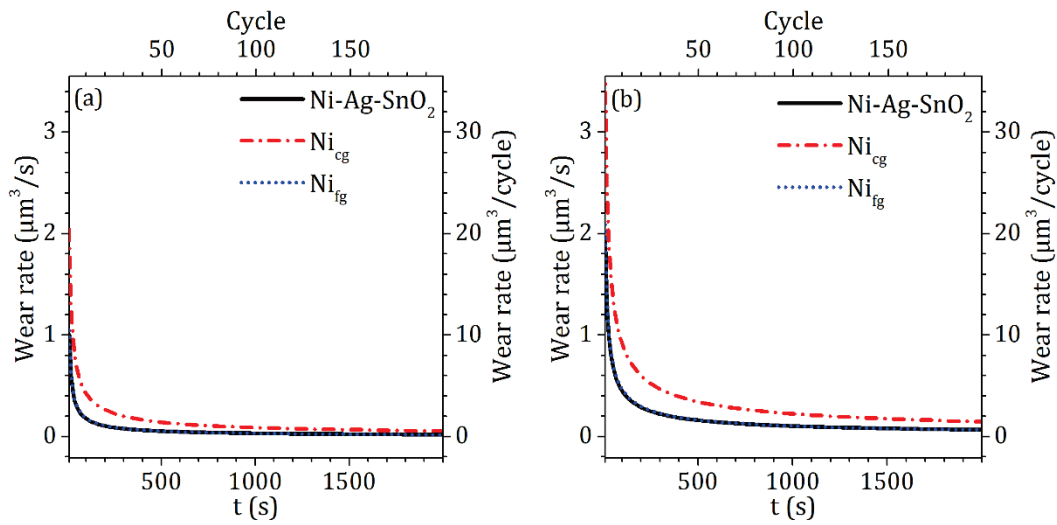


**Fig. 5.14** Wear-rate curves of pure-Ni and composite films from the (a) 20 and (b) 30 mN tests, according to Eq. 5.12. The values beyond the 100<sup>th</sup> cycle ( $t > 1000$  s) show the expected behaviour of the samples according to the model.

Given the nature of the resulting function, the wear rate would asymptotically approach zero after enough time or cycles. In physical terms, this would indicate the transition from the plastic to the elastic regime. Such behaviour would result from the work-hardening of the films due to the recurrent sliding of the hard diamond ball, allowing the material to accommodate stresses with continuously decreasing plastic deformation. In real experiments,

the wear rate may not reach zero and instead stabilise in a higher value, if the work-hardening limit of the material were to be reached during the test. Again, the Ni-Ag-SnO<sub>2</sub> showed a very superior wear resistance with respect to Ni<sub>cg</sub>, with reductions of 65% and 54% in the wear rate by the end of the tests at 20 and 30 mN, respectively.

#### **5.3.4.1 Generalisation of the normal-displacement parameters $\alpha$ and $\beta$**

The wear rate formulas above presented could be expanded to describe more generally the behaviour of the evaluated tribosystems. In order to do that, the parameters  $\alpha$  and  $\beta$  of Eq. 5.8, which depend on the involved material and  $F$  applied, need to be expressed in terms of those dependencies. Given that only the wear tests at 20 and 30 mN were considered in the modelling of the wear rate, the analysis of  $\alpha$  and  $\beta$  was done separately and specifically for those two cases. Doing otherwise would require more experimental data at different  $F$ .

The parameter  $\alpha$  can be interpreted as the indentation depth of the first cycle, since  $N = 1$  results in  $D = \alpha$ . Therefore,  $\alpha$  should be closely related to the  $H$  of the material and the  $F$  applied. The fraction of the counter ball penetrating the samples can be geometrically described as a spherical cap of height equal to  $D$ . Its surface area is given by  $2\pi RD$ , which is a good approximation of the indenter-sample area of contact. Based on the definition of  $H$ , this contact area can also be expressed as  $F/H$ . By equating both expressions, it becomes clear that the initial  $D$  (i.e.,  $\alpha$ ) is given by  $F/2\pi RH$ . Accordingly, the experimental data ( $\alpha$  vs  $H$ ) was fitted separately for each  $F$  with a rational function of  $H$  ( $\alpha_H$ ) given by

$$\alpha_H = c_1/H + c_2, \quad (5.13)$$

where  $c_1$  is a constant which incorporates the effects of  $F$ ,  $R$  and the correction factor for using values of  $H$  obtained with a pyramidal indenter (Berkovich); and  $c_2$  compensates for the deviations which naturally arise from the simplifications of the model. The results of this are displayed in Fig. 5.15a.

Being Eq. 5.8 a power law whose nature derives from the work hardening of the films, the exponent  $\beta$  could be considered to be analogous to the work-hardening exponent. Since  $\beta$  displayed only small fluctuations among films of the same type (see Fig. 5.15b), due to their similar work-hardening behaviour, it was estimated by averaging the values from each sample of the same material ( $\beta_m$ ). The higher values of  $\beta_m$  for larger  $F$  were the natural response to the increase in the strain rate.

The values of  $c_1$ ,  $c_2$  and  $\beta_m$  for each  $F$  and type of material are listed in Table 5.8. Finally, a more general form of Eq. 5.12 can be derived for analysis by replacing  $\alpha$  and  $\beta$  with  $\alpha_H$  and  $\beta_m$ , respectively. The average errors of  $\alpha_H$  and  $\beta_m$  with respect to the values of  $\alpha$  and  $\beta$  found in Table 5.7 were 6 and 10%, respectively.

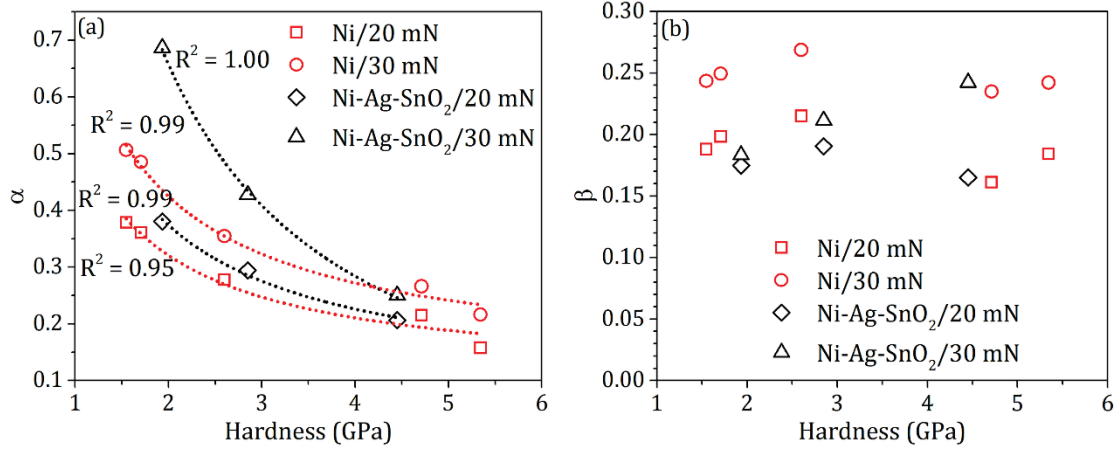


**Fig. 5.15** Analysis of the parameters (a)  $\alpha$  and (b)  $\beta$  from the power-function approximation of  $D$  (Eq. 5.8).

**Table 5.8** Fitting parameters involved in the modelling of the wear rate, used for calculating  $\alpha_H$  and  $\beta_m$  (the latter being a constant, which is listed in the table).

	$F$ (mN)	$c_1$	$c_2$	$\beta_m$
Ni-Ag-SnO <sub>2</sub>	20	0.59	0.08	0.18
	30	1.49	-0.09	0.21
Ni	20	0.44	0.10	0.19
	30	0.61	0.12	0.25

## 5.4 Conclusions

The friction and wear behaviour of the Ni-Ag-SnO<sub>2</sub> composite films was investigated, together with two types of pure-Ni films (coarse and fine grained) for comparison and analysis purposes. The main results here obtained are summarised next.

- In all cases, plastic contact during sliding resulted in ploughing-type abrasive wear, which was evidenced by well-defined grooves with ridges at both sides and by the approximately constant  $\mu$  during the tests. The formation of an oxide-containing tribolayer was confirmed by EDS (oxidative wear), whose composition depended on the  $F$  applied.

The wear tracks' subsurface grain morphology was heavily modified as a result of plastic deformation, which took place in the absence of significant thermal effects (as suggested by the flash-temperature analysis).

- At low  $F$  (5 and 10 mN)  $\mu$  depended on  $H$ , assuming larger values for the softer films due to their higher susceptibility towards adhesion and the formation of asperity junctions. This effect was not observed at high  $F$  (20 and 30 mN), as a result of the work-hardening of the films. Moreover, a general dependence of  $\mu$  on  $F$  was observed for each analysed sample. This was attributed to scale effects, which were explained by the strain-gradient plasticity theory and the change of the involved microslip mechanism.
- The composite films exhibited an enhanced wear resistance with respect to the similarly deposited  $N_{cg}$ , evidenced by reductions in  $W$  (ranging between 52 and 74%) and wear rate (from 54 to 65% at the end of the tests). The increased  $H$  of the Ni-Ag-SnO<sub>2</sub> was found to be responsible for this, since the similarly hard  $N_{fg}$  delivered similar results. This information, together with the fact that all films displayed the same type of friction and wear behaviour, led to conclude that the effect of the Ag-SnO<sub>2</sub> phase in the tribological response of the composite was exclusively the increase in  $H$  through grain refinement. Probably due to the low SnO<sub>2</sub>-nanowires content, no other qualitative changes were detected.
- Numerical models were developed which allowed analysing the  $W$  and wear rate of the studied samples. Regarding the latter, it was demonstrated that ploughing wear in such tribosystems can be accurately described by the geometry of the indenter in combination with traditional concepts related to the mechanical properties of the samples (like the power law of work hardening and the mathematical definition of  $H$ ).

## 6 Analysis of the microstructural thermal stability

### 6.1 Introduction

Nanocrystalline and ultrafine-grained Ni-based films and coatings are widely used in a broad variety of applications due to their high mechanical strength and remarkable wear and corrosion resistance [5,33,34]. However, due to a remarkably large volume-fraction of intercrystalline components (mostly grain boundaries), they possess a large excess of free energy, which results in a metastable microstructure. Then, upon exposure to relatively low temperatures, they might experiment several changes such as grain growth, texture development and phase transformations, which might severely degrade their properties [246–250]. For instance, some authors reported observing the first signs of instability in nanocrystalline Ni films even at temperatures as low as 80 °C [247,251]. These problems may arise not only in applications at hot environments but also at ambient conditions. An example of this is given by tribological systems, where friction during high-speed sliding may increase the temperature locally at asperity junctions, leading to dynamic recrystallization [209,213,252]. Another case is that of electrical contacts and other microelectronic components, where Joule heating, fretting and the action of electrical arcs may also affect their reliability due to thermal effects [253,254].

The electrodeposition technique offers mainly two possibilities for enhancing the thermal stability of several metals. One method involves the use of organic additives in the electrolyte bath, resulting in the incorporation of certain chemical species into the deposits. These impurities segregate into grain boundaries upon heating, exerting a drag force that hinders their mobility. The other approach involves the co-deposition of secondary elements or inert particles, resulting in the formation of alloys and metal-matrix composites, respectively [32]. The alloying elements and reinforcing phases exert a pinning force on migrating grain boundaries and act as nucleation sites, which limits grain growth both during deposition and thermal activation. However, the effectiveness of these methods in preventing thermally induced transformations is often quite limited.

Concerning the Ni-Ag-SnO<sub>2</sub> composite under evaluation, both the high thermal stability of SnO<sub>2</sub> and the non-miscibility of Ag with Ni [9] are expected to play an essential role in its thermal behaviour. For instance, upon heating, the Ag-coated nanowires may act as supporting backbone for the matrix and hinder the movement of its grain boundaries, as it was

the case during the deposition process. Moreover, no phase transformation is thermodynamically favoured. In view of these considerations, the purpose of the work described in this chapter was to assess the microstructural thermal stability of Ni-Ag-SnO<sub>2</sub> and gain an understanding of how this is influenced by its constituent phases. To that end, different annealing treatments were performed on the samples, and the resulting transformations were investigated by means of XRD and EBSD-assisted SEM. As in previous chapters, two sets of pure-Ni films were also studied for analysis and comparison purposes: (i) one which was deposited using exactly the same bath and experimental parameters as for the Ni-Ag-SnO<sub>2</sub> and (ii) another whose grain size was refined to match that of the composite's matrix.

## **6.2 Experimental details**

The Ni-Ag-SnO<sub>2</sub> composite films were produced as described in 3.1, with the only exception that about 1 µm of excess Ni (Ag-SnO<sub>2</sub>-free volume) was purposely left on top. This was done in order to be able to compare, within each sample, the behaviour of both the reinforced and unreinforced regions.

Additionally, two sets of pure Ni films were used for comparison and analysis purposes, denominated coarse-grained (Ni<sub>cg</sub>) and fine-grained (Ni<sub>fg</sub>) Ni. They were deposited using the same bath and experimental parameters as for the composite's matrix, with the only addition of the grain refiner saccharin (< 0.1 g/l) in the case of Ni<sub>fg</sub>, in order to obtain a grain size similar to that of the composite's matrix.

Isothermal annealing treatments were conducted at 300 and 500 °C for 10 h according to 3.1.4. In-situ XRD measurements were carried out during non-isothermal annealing (up to 600 °C) as described in 3.2.6.

## **6.3 Results and discussion**

### **6.3.1 Microstructural features of the as-deposited films**

The grain morphology of the as-deposited samples can be observed in Fig. 6.1, both from the cross-section and surface of the films. The composite presented a fine-grained microstructure which resulted from grain growth stagnation due to the pinning force exerted by the Ag-SnO<sub>2</sub> during the electrodeposition of the Ni matrix. Such refining becomes evident when attending to the microstructure of Ni<sub>cg</sub> which, having been deposited using exactly the same bath and parameters, exhibited much larger grains with a clear columnar structure.

In the case of  $Ni_{fg}$ , the addition of saccharin into the electrolyte resulted in a finer and slightly elongated grain morphology.

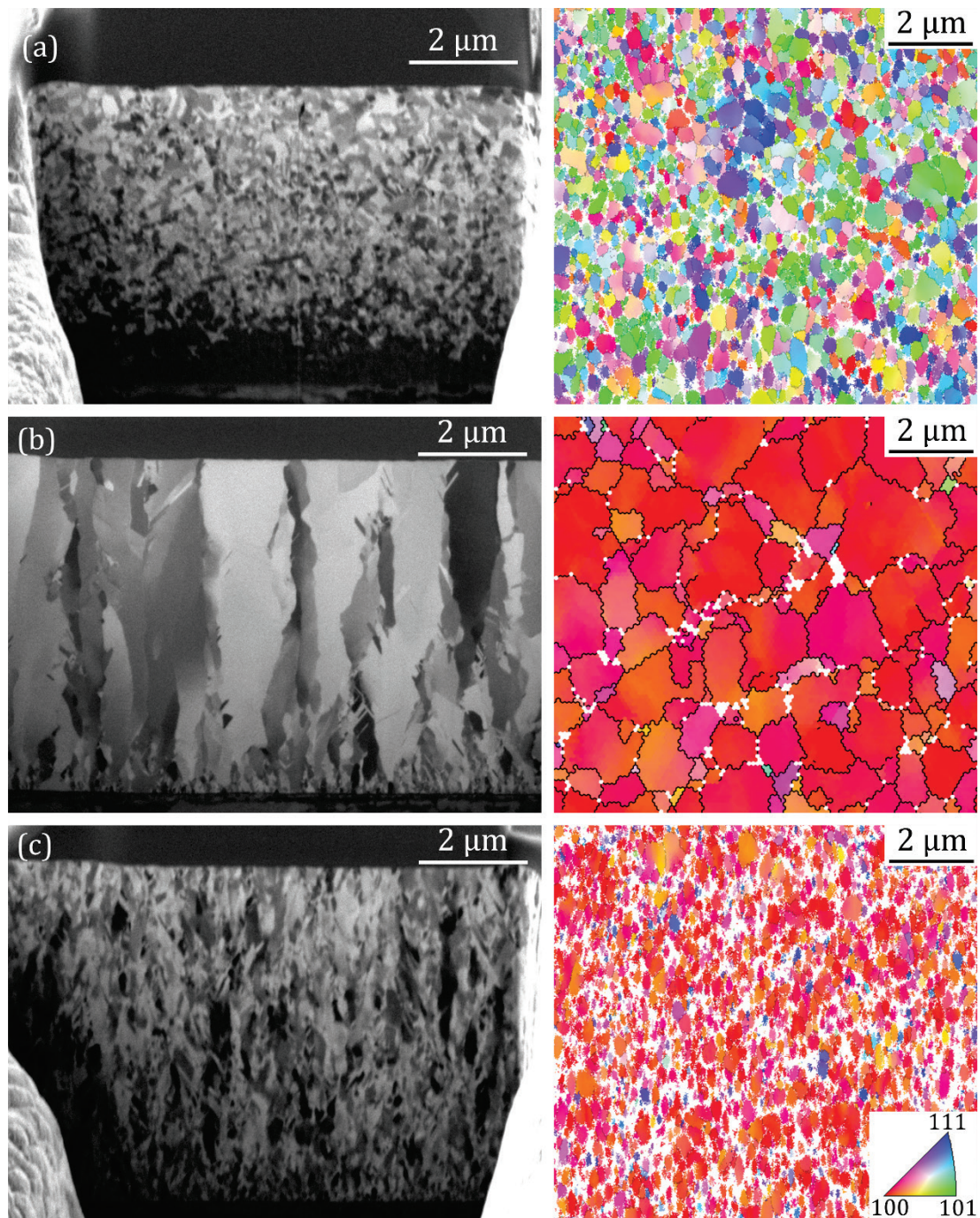


**Fig. 6.1** FIB ion-channelling-contrast images together with inverse pole figure maps (recorded at the cross-section and at the surface, respectively) from as-deposited (a) Ni-Ag-SnO<sub>2</sub>, (b) Ni<sub>cg</sub> and (c) Ni<sub>fg</sub> films.

The inverse pole figure maps of Fig. 6.1 suggest an absence of apparent texture in the Ni-Ag-SnO<sub>2</sub> films. As for the pure-Ni samples, their {100}-planes laid parallel to the surface. The pole figures of Fig. 6.2 certainly confirmed this, showing very strong and well defined <100> fibre texture in the case of pure-Ni samples. As for the composite, no preferential orientation was detected for any of the main crystallographic plane families. The mechanisms responsible for the observed grain morphologies and orientations have been already described in 4.3.1.

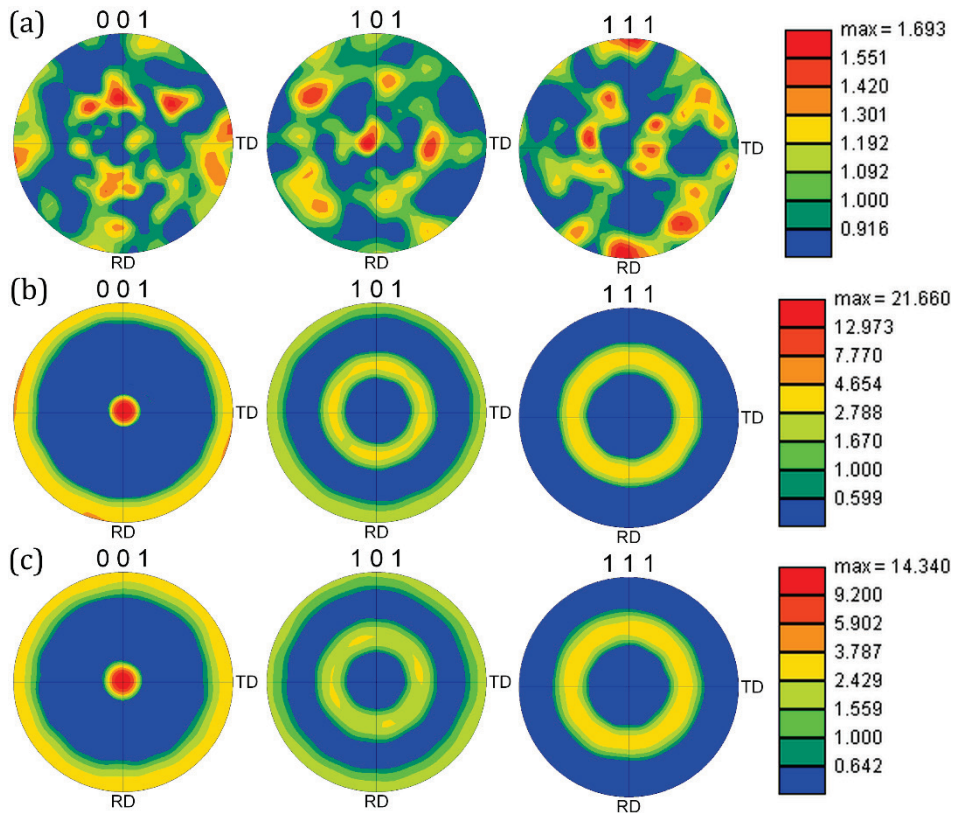


**Fig. 6.2** Pole figures of as-deposited (a) Ni-Ag-SnO<sub>2</sub>, (b) Ni<sub>cg</sub> and (c) Ni<sub>fg</sub>. The random crystallographic orientation of the composite contrasts with the <100> fibre texture of the pure-Ni films.

The grain size distributions of the samples can be observed in Fig. 6.3. A distinction was made for the composite regarding its reinforced (Ag-SnO<sub>2</sub>-rich) and unreinforced (pure Ni) regions. For the former, the grain size was measured by EBSD on the corresponding area of the cross-section of the film while, for the latter, on the surface (like for the pure-Ni samples). If allowed, the grains of the unreinforced region would continue to grow, unconstrained, with the thickness of the film. The grain size distributions of Ni-Ag-SnO<sub>2</sub> and Ni<sub>fg</sub> were accurately fitted with the lognormal function, which is typically applied in the case of

bulk systems with normal grain growth, or films whose grain size is small in relation to their thickness. However, in the case of columnar grains whose length is similar to the film thickness, deviations may occur [255]. This was the case for  $\text{Ni}_{\text{cg}}$ , whose wide grain size distribution showed good fitting to a bimodal function composed of two closely lying lognormal peaks. It should be also noted that, for  $\text{Ni}_{\text{cg}}$ , the considered grain diameters corresponded to the lateral dimension of its columnar grains (measured by EBSD on the surface).

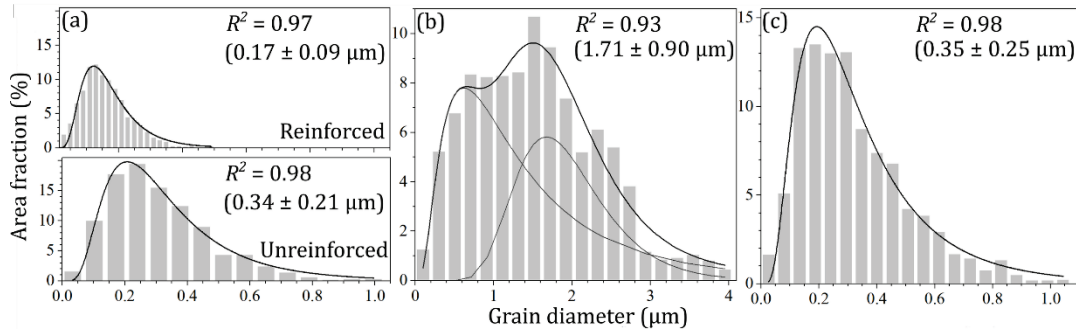


**Fig. 6.3** Grain size distribution of the as-deposited (a)  $\text{Ni-Ag-SnO}_2$ , (b)  $\text{Ni}_{\text{cg}}$  and (c)  $\text{Ni}_{\text{fg}}$  films, showing the coefficient of determination, mean value and standard deviation of the fit functions.

### 6.3.2 Analysis of the thermal stability by means of different annealing treatments

Microstructures with high density of defects, such as those resulting from heavy deformation (dislocation-rich) or grain refinement (grain-boundary-rich), are thermodynamically unstable. Thus, upon annealing, they undergo complex changes leading to the reduction of their large excess of Gibbs free energy. This process is generally recognised to be divided into three stages, namely recovery, recrystallization and grain growth. The first is characterised by the annihilation of dislocations through the formation and growth of subgrains, driven by the reduction of strain energy. During recrystallization, the heterogeneous formation of new, strain-free grains takes place, which grow by migration of high-angle grain boundaries, accompanied by a change in texture. Here, the driving force is the release of the remaining strain energy and, in the case of films, the minimisation of surface and interface energies. In this context, the concept of grain nucleation does not carry its traditional signification, being it that a previously non-existent structure forms. Instead, grains develop from recovered regions, cells or subgrains, which act as nuclei. Finally, grain growth consists

in the coarsening of the microstructure, where free energy is further released by the reduction of grain-boundary area. Not only it is possible for these stages to overlap, but they can also occur discontinuously or uniformly throughout the microstructure [256].

Retarding and pinning forces may affect the mobility of grain boundaries and so the normal development of the above-mentioned processes, resulting in an increased thermal stability of the material. Said forces may originate from the presence of secondary-phase particles, solutes, triple junctions and surface effects.

Great efforts have been placed in the development of analytical and physical models, aimed to explain and predict the behaviour of annealing-related phenomena. These are thoroughly discussed in the review papers from Rollet [257] and Humphreys [258]. However, the applicability of such models is very restricted, given the substantial limitations of the current understanding of the involved physical metallurgy processes.

The annealing behaviour of the samples under study is analysed in the following sections, attending to the relevant aforementioned elements. In order to do that, different types of annealing treatments were carried out, each of them providing different valuable information on these topics.

#### **6.3.2.1 In-situ XRD analysis during non-isothermal annealing**

High-temperature XRD was employed for the qualitative analysis of the microstructure evolution during non-isothermal annealing, regarding grain (or rather crystallite) growth and texture. In this analysis,  $Ni_{cg}$  and  $Ni_{fg}$  are indistinctly treated and regarded simply as Ni films, since no significant qualitative difference was observed in the nature of their behaviour.

It is well established that XRD peak widths are inversely proportional to crystallite size. Based on this principle, the methods from Scherrer, Williamson-Hall and Warren-Averbach [259,260] are typically used in the literature for reporting the grain size of polycrystalline materials (mostly nanocrystalline). However, what it is actually being reported is sometimes a matter of confusion. XRD methods based on peak broadening allow estimating the size of crystallites, which are the fundamental monocrystalline coherent domains. Their dimension and the grain size measured by other complementary techniques (such as TEM) show agreement only in the case of very fine grains, with sizes up to about 60 nm [261]. For coarser microstructures, as in the case of the films here studied, grains constitute agglomerates of these crystallites. It is normally accepted that grains are delimited by high-angle

grain boundaries ( $\geq 15^\circ$  in the present EBSD measurements). Therefore, crystallites could be roughly considered as subgrains, being delimited by low-angle grain boundaries. Moreover, the results from these XRD-based methods should be interpreted as a lower bound on the crystallite size, since a variety of other factors (not always considered in the analysis) can contribute to peak broadening. These include the instrumental peak profile, microstrains, non-uniform lattice distortions, faulting, dislocations and antiphase domain boundaries [262].

Considering the range of grain sizes of the studied samples and the limitations of the technique, the onset and development of microstructure coarsening were analysed only at a qualitative level. This was performed by following the evolution over temperature of the reciprocal of the full width at half maximum (FWHM) of the main XRD peaks. The results of this are presented in Fig. 6.4. When considering the curves of Ni, from both the pure-Ni and composite films, three stages could be recognised. The first one started with null growth at room temperature, showing the first signs of instability at around 100 °C which were followed by slow changes up to 250 °C. The second stage corresponded to the fast growth observed between 250 and 350 °C. Finally, the third stage was characterised by a deceleration and most likely stagnation from 350 °C onwards.

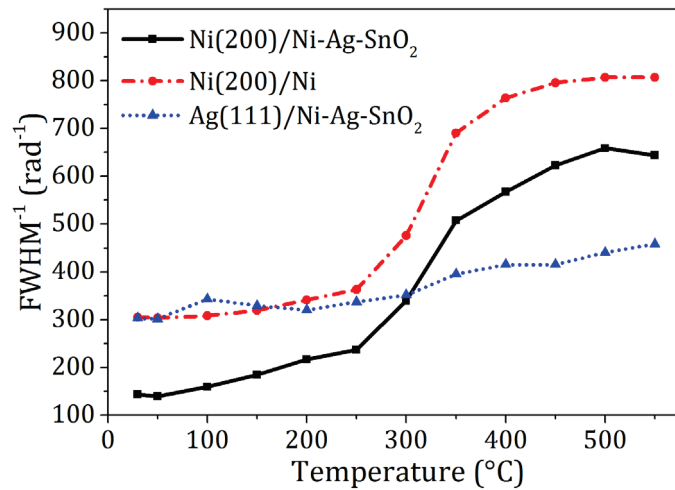


**Fig. 6.4** Analysis of the onset and development of microstructure coarsening, which was performed by following in-situ the evolution of the FWHM<sup>-1</sup> of the main XRD peaks during non-isothermal annealing.

Even in the absence of previous cold work, the first stage can be understood as a recovery process. Here, the subgrain structure developed and coarsened, and the relaxation of the

microstructure took place. This resulted from the annihilation of defects and the release of microstrains. Electrodeposits can be heavily stressed due to their relatively high density of defects, such as impurities, porosity and grain boundaries. These shift atoms locally from their natural positions, increasing the strain energy. Moreover, films tightly bonded to a substrate might develop thermal strains when cooled from the deposition temperature to ambient conditions. These thermal strains arise from differences in thermal expansion and is given by  $(\alpha_{LF} - \alpha_{LS})\Delta T$ , where  $\alpha_{LF}$  and  $\alpha_{LS}$  are the linear thermal expansion coefficients of the film and the substrate, respectively, and  $\Delta T$  the change in temperature. The values of  $\alpha$  for the as-deposited films are listed in Table 6.1. Considering the relatively small variations in  $\alpha_L$  among contacting pairs (Ni/steel for pure-Ni films; Ni/Ag and Ag/SnO<sub>2</sub> for the composite) and the low deposition temperatures ( $\Delta T = 20$  °C for Ni electrodeposits and  $\Delta T = 0$  °C for electroless Ag), the build-up of large thermal strains could be disregarded. The observed behaviours of the films during this first stage of the experiment were in agreement with other works' findings on the thermal stability of nanocrystalline Ni electrodeposits, which reported the first appearance of fluctuations at around 100 °C and low to negligible growth up to 200 °C [247,251,263,264].

**Table 6.1** Linear thermal expansion coefficients of the materials under study.

$\alpha_L$ at 25 °C ( $10^{-6} \times K^{-1}$ )			
Ni	Ag	SnO <sub>2</sub>	AISI 316L
13	19	4	16

Starting at 250 °C, the second stage was characterised by much faster kinetics. This signalled the initiation of rapid grain growth, which developed by migration of high-angle grain boundaries. Temperatures close to 250 °C are typically identified for Ni as the onset of grain growth, which proceeds abnormally up to about 300 °C and normally afterwards [247,251,263–265].

Beginning at about 350 °C, the third and last stage showed the stabilisation of the FWHM<sup>-1</sup>. This indicated in part the stagnation of grain growth and microstructure development, with the completion of a new, more stable configuration. However, this information must be prudently judged, since XRD methods are able to measure crystallite sizes up to approximately 150 nm only. Usually from 100 nm onwards, the broadening of XRD peaks starts to fall below the device resolution and is mostly given by the instrumental peak profile.

Concerning the thin Ag deposits covering the SnO<sub>2</sub> nanowires in the composite, a quite distinct behaviour was observed. The FWHM<sup>-1</sup> evolved in a rather regular manner along the entire temperature range, showing a very limited growth in comparison to Ni. This would be usually unexpected, given the much lower melting point of Ag (962 vs 1455 °C). The reason behind this was that the Ag grains were mostly surrounded by the others from different phases (Ni at one side and SnO<sub>2</sub> at the opposite). This resulted in strong pinning forces, which impeded the normal development of growth kinetics. However Ni grains were mostly surrounded by others of the same kind, which facilitated boundary migration.

The second part in the XRD analysis of the annealing behaviour of the films dealt with the evolution of texture, which was evaluated by means of the relative texture coefficient (RTC) [147,160,266]. It was calculated for the (hkl) diffraction peaks associated to the main crystallographic orientations in FCC metals as

$$RTC(hkl) = \frac{I(hkl)}{I_0(hkl)} \left[ \frac{1}{N_R} \sum \frac{I(hkl)}{I_0(hkl)} \right]^{-1}, \quad (6.1)$$

where  $I(hkl)$  and  $I_0(hkl)$  are the integrated intensities of the (hkl) reflections produced by the films and a standard powder sample, respectively, being  $N_R$  the total number of reflections used. The RTC evolution of the Ni phase from both the pure-Ni and composite films is displayed in Fig. 6.5.

As observed during the characterisation of the as-deposited films, the pure-Ni samples exhibited a very strong  $\langle 100 \rangle$  texture, which gradually evolved into  $\langle 111 \rangle$ . The texture was stable up to 250 °C and then rapidly changed until the  $\langle 111 \rangle$  became dominant (at 450 °C), slowing down from there onwards. These results supported those from the FWHM analysis, which revealed the onset of growth to be at 250 °C. Moreover, the RTC evolution showed close agreement with the three stages of growth previously described. This indicated that growth stagnation was the reason behind the deceleration during the third stage, rather than the limitations of the XRD technique.

In the case of the composite films, their random orientation remained unaltered during the whole treatment (which will be later explained), demonstrating superb thermal stability. Different mechanisms may operate, which favour (or inhibit) the growth of grains of specific orientations, resulting in the development of texture in films. These are thoroughly discussed in the following section.

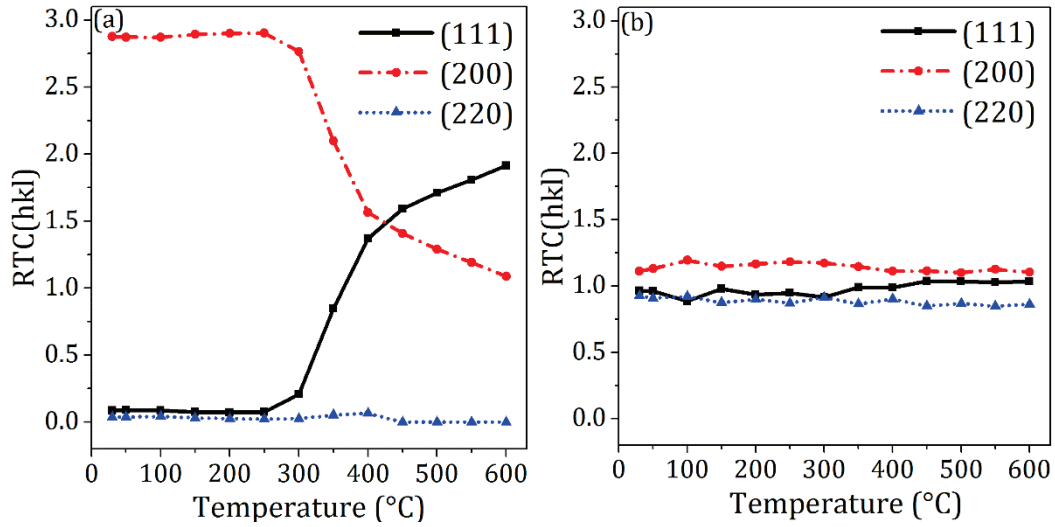


**Fig. 6.5** Texture evolution of (a) pure-Ni and (b) composite films, evaluated in-situ during non-isothermal annealing by means of the RTC.

### 6.3.2.2 Microstructure characterisation after isothermal annealing at elevated temperature

By annealing at a sufficiently high temperature, homogeneous microstructural transformations are promoted. If the treatment's duration is long enough, a new, stable or steady-state microstructure may be achieved. This was performed on the studied films by isothermal annealing at 500 °C for 10 h. According to the XRD results and previous experimentation, such temperature and length would allow producing the desired new, stable configurations. The comparison of the specific features of the annealed and as-deposited states could be used as a benchmark of the thermal stability of the investigated materials, providing also an understanding of the mechanisms driving the involved processes.

The kinetics of recrystallization and growth under isothermal conditions can be described by two complementary models. The first one is given by the Johnson-Mehl-Avrami-Kolmogorov equation (JMAK), which expresses the fraction of transformed material (i.e., the degree of completion of the transformation). It is given by  $1 - \exp(-C\tau^r)$ , where  $C$  and  $r$  are constants associated to nucleation/growth rates and morphology, respectively; and  $\tau$  is the elapsed time [267–269]. The second model is the power law which describes normal growth (homogeneous transformation). It is given by  $d_f^m - d_0^m = \kappa\tau$ , where  $d_0$  and  $d_f$  are the initial and final average grain radius, respectively;  $m$  is the grain growth exponent; and  $\kappa$  is a constant which depends on the activation energy for boundary mobility and temperature

[256]. The theoretical value of  $m$  is 2, but it is only rarely found experimentally (it usually adopts larger values  $\leq 7$ ) [247,256,270].

Proceeding with the experimental results, the grain morphology of the annealed samples is displayed in Fig. 6.6, both from the cross-section and surface of the films. The inverse pole figure maps show relatively regular grain structures in all cases, with no evidence of abnormal grains being present. This supports the assumption of normal/homogeneous growth dominating the process, which could be expected from the high temperature applied. At both types of pure-Ni films, the original  $\langle 100 \rangle$  fibre texture was replaced by a  $\langle 111 \rangle$  orientation.

In the case of  $\text{Ni}_{\text{cg}}$ , the analysis of the cross-section revealed that a fully columnar structure developed, mostly with wide grains extending from the substrate up to the surface. Such morphology is to be expected from the stagnation of normal-growth in films, where the average grain diameter might amount to 2-4 times the film thickness [255]. Being  $\text{Ni}_{\text{cg}}$  a single-phase material and having higher purity than  $\text{Ni}_{\text{fg}}$  (since no additives were present in its deposition bath), its microstructural evolution should have been the one following most closely the JMAK normal-growth kinetics from all the investigated films (with  $m$  not too far from 2). The formation of the columnar structure (i.e., grain boundaries running perpendicular to the surface) was the result of grain-boundary energy minimisation. Moreover, the stagnation of the lateral growth of the grains was associated to a drag force or pinning mechanism. Mullins proposed that such behaviour is a consequence of the formation of thermal grooves on the surface (at grain-boundary intersections), which act as a barrier for grain-boundary migration [271,272]. Thermal grooves result from the balance of surface and grain-boundary tensions at their junction, which is compatible with the perpendicular orientation of grain boundaries.

The  $\text{Ni}_{\text{fg}}$  films displayed also a homogeneous transformation. However, their microstructure could not develop a columnar morphology and its growth stagnated at a much smaller average grain size. Since the only difference in the fabrication of  $\text{Ni}_{\text{fg}}$  with respect to  $\text{Ni}_{\text{cg}}$  was the addition of saccharin in the electroplating bath, the different behaviour could be attributed to a relatively high concentration of sulfur (from the grain refiner) in the deposits [246,247,251]. With negligible solubility in Ni, it segregates and accumulates on grain boundaries upon annealing, impeding their motion and thus increasing the thermal stability of the film. This effect is known as solute drag and its action is physically described by the models of Cahn [273] and Lücke and Stüwe [274].

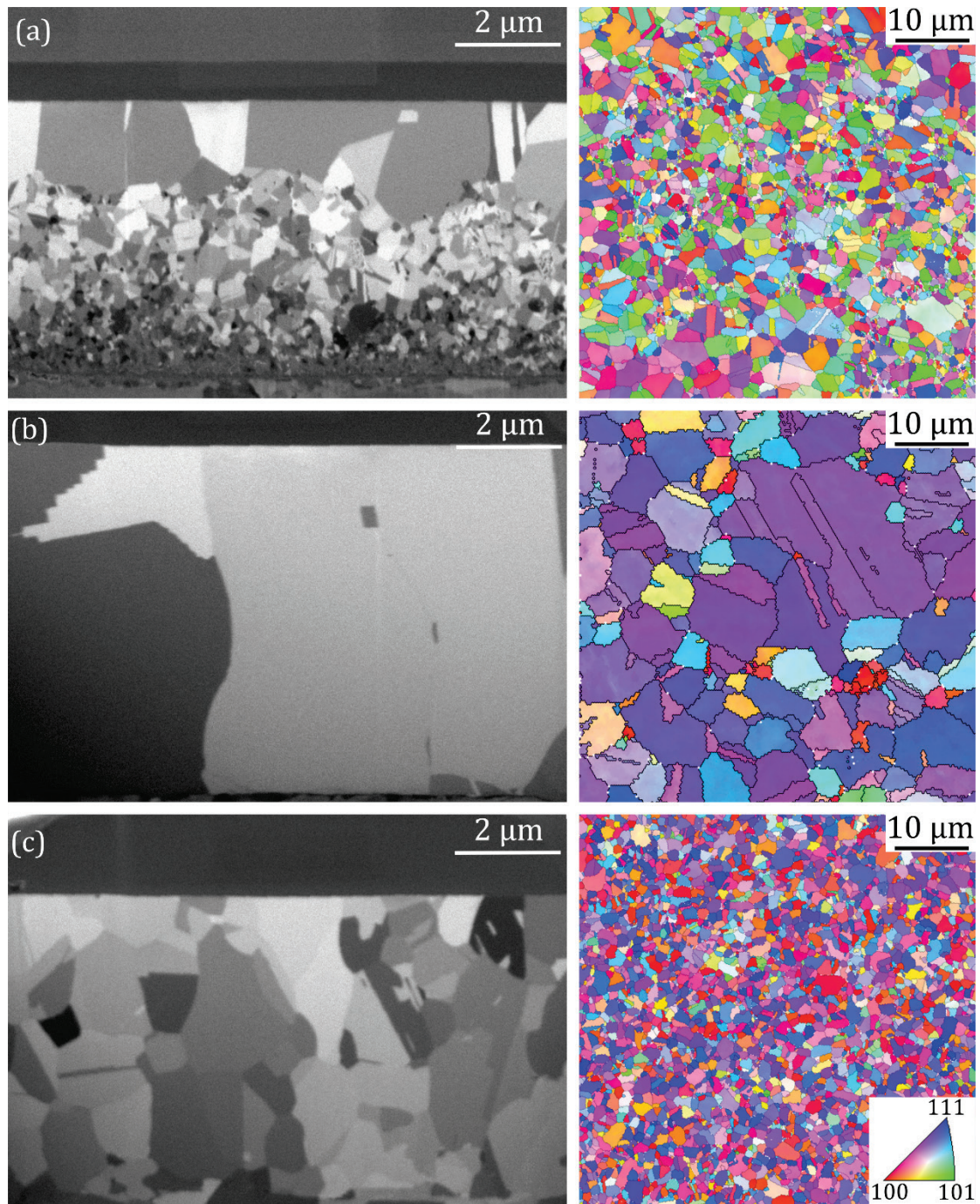


**Fig. 6.6** FIB ion-channelling-contrast images together with inverse pole figure maps (recorded at the cross-section and at the surface, respectively) from (a) Ni-Ag-SnO<sub>2</sub>, (b) Ni<sub>cg</sub> and (c) Ni<sub>fg</sub> films isothermally annealed at 500 °C for 10 h.

In the case of the Ni-Ag-SnO<sub>2</sub> films, a very distinct behaviour was observed between the unreinforced and reinforced regions. The unreinforced area displayed a similar structure to that of Ni<sub>cg</sub>, with large columnar grains running from the top of the reinforced region up to

the surface. On the other hand, the reinforced part exhibited a much finer microstructure, product of the pinning of grain boundaries of the Ni matrix by the secondary phases (Ag-SnO<sub>2</sub>). The interface between a matrix and its reinforcement can be considered equivalent to a reduction in grain-boundary area. This means a reduction in free energy or, from another point of view, that an extra amount of energy is required for removing the obstacle to grain-boundary motion. According to Zener, this energy is proportional to the grain-boundary tension and the size of the pinning structures [152]. The EBSD maps from the cross-section of the composite (Fig. 6.7) allow discerning much more clearly the difference in the grain structure between both its regions.

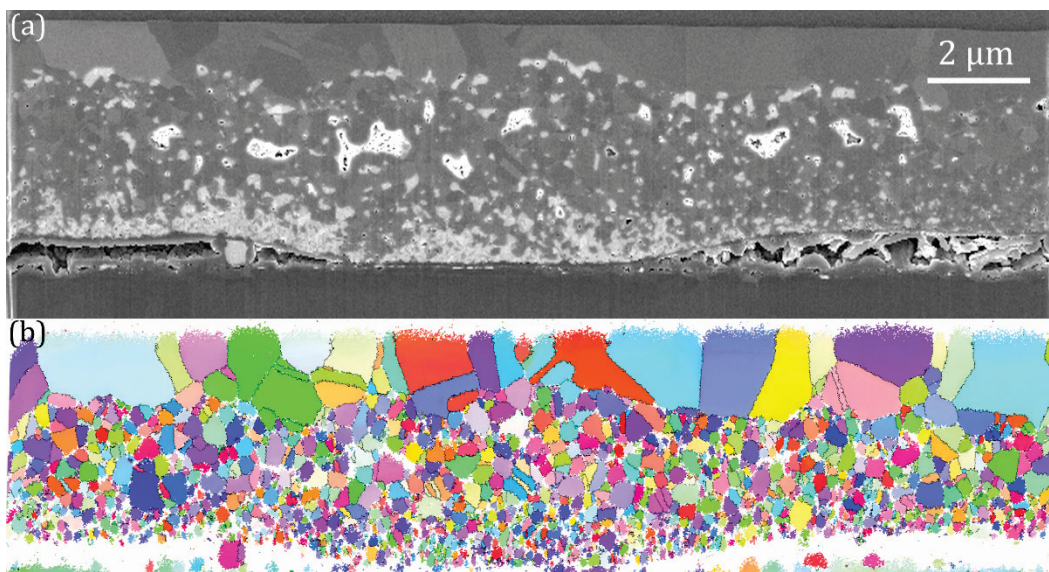


**Fig. 6.7** FIB ion-channelling-contrast images together with inverse pole figure maps (recorded at the cross-section and at the surface, respectively) from (a) Ni-Ag-SnO<sub>2</sub>, (b) Ni<sub>cg</sub> and (c) Ni<sub>fg</sub> films isothermally annealed at 500 °C for 10 h.

The grain size distributions of the films are displayed in Fig. 6.8. Like in their as-deposited states, the annealed samples showed good fitting with the lognormal function (bimodal again in the case of Ni<sub>cg</sub>). For all the pure-Ni samples (including the unreinforced part of the composite), increments in the average grain size of about 300% were observed. On the other hand, the reinforced region of the Ni-Ag-SnO<sub>2</sub> films exhibited an increase of only 70%, what gives a quantitative measure of its enhanced thermal stability. This would most likely result in a strong reduction in the degradation of its mechanical properties, such as yield strength and hardness, which in turn play a major role in the tribological behaviour.

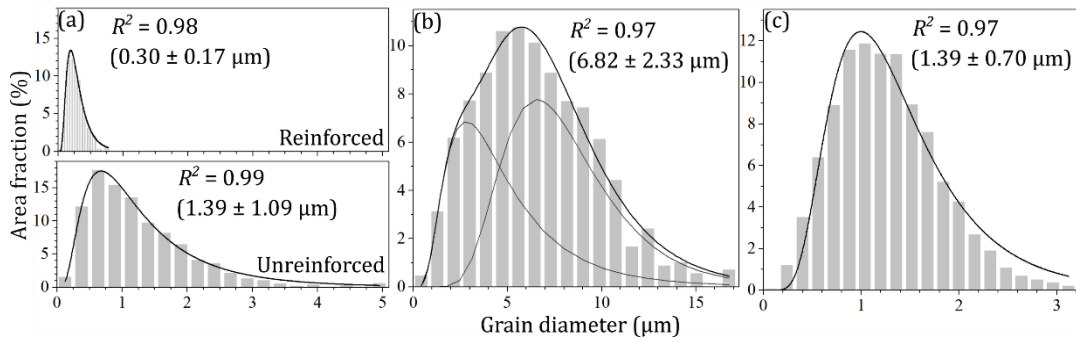


**Fig. 6.8** Grain size distribution of (a) Ni-Ag-SnO<sub>2</sub>, (b) Ni<sub>cg</sub> and (c) Ni<sub>fg</sub> films after isothermal annealing at 500 °C for 10 h, showing the coefficient of determination, mean value and standard deviation of the fit functions.

During recrystallization and growth, the texture evolves driven by different sort of mechanisms. The many possible outcomes depend mostly on the characteristics of the original microstructure and the available sources of Gibb’s free energy. In the case of films, two competing mechanisms are commonly regarded as responsible for the preferential growth of grains with specific orientations. The first one corresponds with the minimisation of surface and interface (film-substrate) energy. For FCC metals, the development of grains with their {111} planes parallel to the surface is favoured, since those are the most densely packed. This results in a reduction of the dangling-bonds density at the surface, thus reducing its energy [255]. This mechanism gains more relevance with decreasing film thickness, due to a larger surface-to-volume ratio.

The second mechanism is strain energy minimisation. Nanocrystalline and ultrafine-grained metals usually display a relatively high yield strength and, therefore, are able to accommodate large strains elastically. Due to their attachment to much thicker substrates, these strains are normally biaxial in nature and thus the strain energy density is directly proportional to the biaxial elastic modulus [275]. Most of FCC metals exhibit anisotropy ratios  $2C_{44}/(C_{11} - C_{12}) > 1$  (2.4 for Ni when applying the stiffness constants  $C_{ij}$  found in [276]), what results in their biaxial moduli assuming minimum values for grains with {100} planes oriented parallel to the surface [277]. The growth of grains with this orientation is therefore favoured, since they minimise strain energy. If the strains were large enough for yielding to occur, they could be accommodated by plastic deformation and thus, the growth of low-yield-strength grains could be favoured. For FCC metals, the grains with {110} orientation possess the lowest yield strength, what makes possible for them to dominate growth in highly strained films.

In view of the above discussed mechanisms, the recrystallization textures of the annealed films were analysed with the help of the pole figures displayed in Fig. 6.9. In agreement with the results from the XRD measurements, Ni<sub>cg</sub> evolved towards a strong  $\langle 111 \rangle$  fibre texture, evidencing that surface energy minimisation governed its recrystallization and growth process. In the case of Ni<sub>fg</sub>, a  $\langle 111 \rangle$  and  $\langle 100 \rangle$  double fibre texture was observed. Similar results were reported by Klement et al. for the annealing of nanocrystalline Ni films [251,278]. Again, the  $\langle 111 \rangle$  component of the texture derived from surface energy minimisation, while the  $\langle 100 \rangle$  was likely the result of strain energy minimization. The use of saccharin as grain refiner favours the co-deposition of impurities and solute atoms, which might strain the deposits. If these strains were large enough, the drive for reducing its associated energy could become predominant for a relevant amount of grains. Moreover, the sulfur segregated at grain boundaries would exert a drag force which could have hindered the development of some nuclei with  $\{111\}$  orientation. This would allow some of the original  $\{100\}$  grains to avoid being consumed and, ultimately, disappear.

The composite films retained their random orientation after annealing. This absence of texture was attributed to two reasons. First, as it was mentioned for Ni<sub>fg</sub>, a limited grain and subgrain-boundary mobility. This resulted from the pinning effect exerted by the Ag-SnO<sub>2</sub> phase. The second reason was the drive for minimisation of interface energy. In the case of the pure-Ni films, the surface area was equal to the film-substrate interface area. However for the composite, the interface was evidently much larger, which resulted from the high surface-to-volume ratio of the nanowire array. The Ag-coated nanowires completely covered the steel substrate and extended towards the surface in all directions, bending along the way. Even when the development of  $\{111\}$ -oriented grains were to be favoured by interface energy minimisation, their orientation with respect to the surface would be random, since it would be dictated by the also random spatial directions along which the nanowires grew (each acting locally as substrate).

The above-described mechanisms could properly explain the results from the EBSD measurements. Then, again, not only in terms of grain size but now also regarding texture, the Ni-Ag-SnO<sub>2</sub> films showed an enhanced thermal stability with respect to the pure-Ni samples.

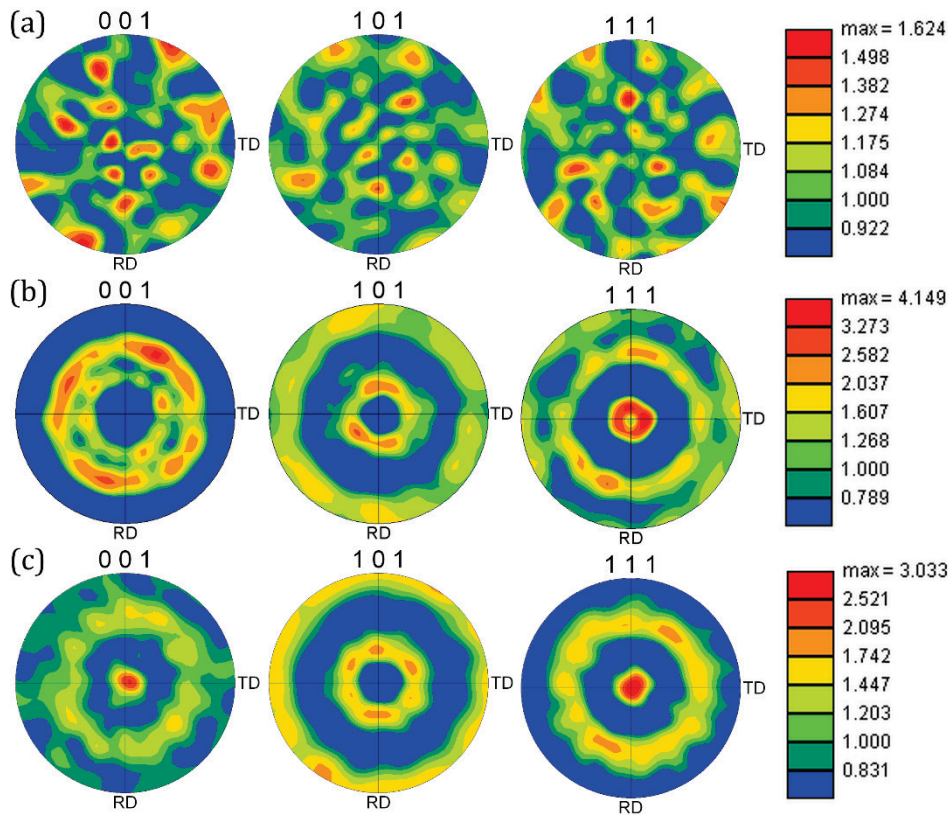


**Fig. 6.9** Pole figures of (a) Ni-Ag-SnO<sub>2</sub>, (b) Ni<sub>cg</sub> and (c) Ni<sub>fg</sub> after isothermal annealing at 500 °C for 10 h. The composite retained its random crystallographic orientation, while the Ni samples evolved from a  $\langle 100 \rangle$  to a  $\langle 111 \rangle$  fibre texture due to surface energy minimisation.

Two alternative mechanisms have been proposed for explaining the formation of strong recrystallization textures from the perspective of nucleation and growth. These are the oriented nucleation and oriented growth models [279,280]. The oriented nucleation model claims that the grains of the favoured orientation nucleate more frequently than the others. Alternatively, the oriented growth model states that nuclei of all orientations are equally present in the original or recovered microstructure, but those of the favoured orientation are able to grow faster. As already mentioned, nucleation in this context must be understood as the development of grains from recovered regions, cells or subgrains, which act as nuclei. In order to determine which mechanism governed the recrystallization of the investigated films, a straightforward method based on EBSD data was applied [280].

Oriented nucleation dictates that the frequency of nucleation of the texture orientation ( $f_T$ ) surpasses the frequency expected in the case of random nucleation ( $f_R$ ). Allowing for an angular deviation of 20°,  $f_R = 0.047$  [280,281]. The value of  $f_T$  was calculated from EBSD data, by dividing the number of grains exhibiting the preferred orientation (applying the same

20° tolerance) by the total number of grains. Then, if  $f_T/f_R \gg 1$ , oriented nucleation was likely the dominant mechanism.

Oriented growth requires that grains with texture orientation were larger than those randomly oriented. That is to say, oriented growth would have taken place if  $d_T/d_R \gg 1$ , where  $d_T$  and  $d_R$  are the average diameter of the grains with the preferred and random orientation, respectively.

The results of this analysis are listed in Table 6.2. The higher values of  $f_T/f_R$  (always much larger than 1) with respect to those of  $d_T/d_R$  (close to 1) indicate that oriented nucleation took place during the present experiments. That is equivalent to say that the majority of nuclei possessed the texture orientation and grew approximately at the same rate as the minority with different orientation.

**Table 6.2** Results of the oriented nucleation vs oriented growth analysis.

	$f_T/f_R$			$d_T/d_R$		
	(001)	(101)	(111)	(001)	(101)	(111)
Ni-Ag-SnO <sub>2</sub>	3.73	8.21	5.31	0.97	0.99	0.99
Ni <sub>cg</sub>	-	-	9.21	-	-	1.73
Ni <sub>fg</sub>	5.84	-	8.93	0.92	-	1.09

### 6.3.2.3 Abnormal growth at the onset temperature of grain growth

During abnormal growth, few grains grow excessively by consuming their smaller neighbours. The result of this inhomogeneous evolution is a microstructure composed of very large grains surrounded by a matrix of finer ones, having a bimodal grain-size distribution. Such a process might take place when there exist large differences in boundary mobility among grains. These could be given by an inhomogeneous grain-boundary drag (by secondary phases, impurities or solutes) or orientation-specific driving forces which favour the growth of subpopulations of grains [256,277]. According to Hiller, abnormal growth may appear in materials with wide grain size distributions, where some grains with much larger size than the average are unstable and grow consuming the others abnormally [282].

Several works report the occurrence of abnormal growth at Ni films when annealing at temperatures up to around 300 °C [246,251,265,283]. In those cases, due to the relatively low temperatures, only few grains may be able to overcome their energy barrier for growth. In

order to evaluate this for the films under study, several samples were isothermally annealed at 300 °C for 10 h. Their resulting grain morphologies are displayed in the inverse pole figure maps of Fig. 6.10.  $Ni_{fg}$  showed the clearest case of abnormal growth, where few, large  $\{111\}$  grains (favoured by surface energy minimisation) ended up surrounded by the original  $\{100\}$ -oriented ones. Something similar occurred with  $Ni_{cg}$ , but in this case, the abnormal grains seemed to have further developed and left behind a smaller fraction of the original microstructure. Such a difference was a consequence of the solute drag force experienced by the grain boundaries of  $Ni_{fg}$ , which was discussed in previous sections.

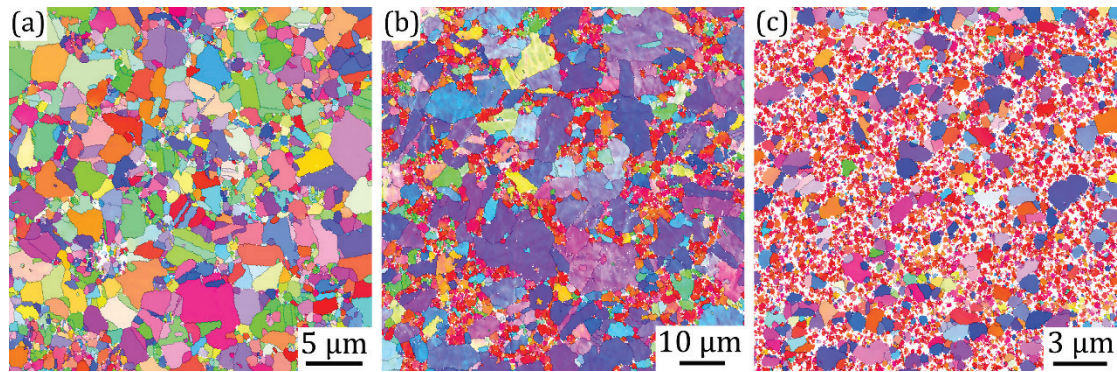


**Fig. 6.10** Inverse pole figure maps of (a)  $Ni-Ag-SnO_2$ , (b)  $Ni_{cg}$  and (c)  $Ni_{fg}$  after isothermal annealing at 300 °C for 10 h. An abnormal grain growth behaviour is evident in the case of the pure-Ni films.

The behaviour of the  $Ni-Ag-SnO_2$  composite was not as evident as that of pure-Ni samples, since its random orientation did not allow discerning between original and developed grains. Then, in an attempt to determine if abnormal growth took place, its grain size distribution was analysed (Fig. 6.11). In view of the unimodal, lognormal nature of the experimental data, it could be concluded that the growth process was characterised by a homogeneous transformation. This was the case since no specific orientation was favoured, resulting in a balanced driving force for growth among grains.

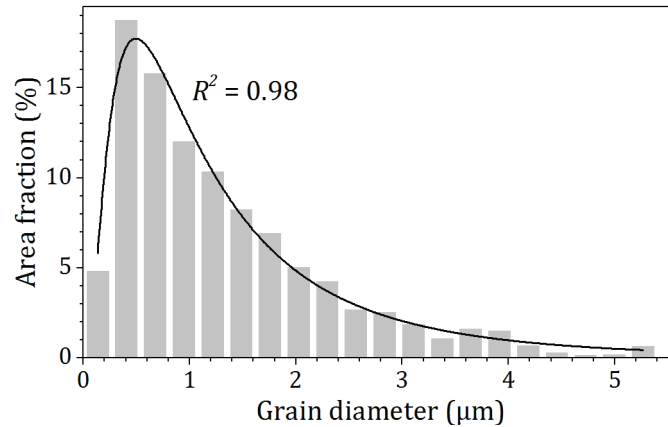


**Fig. 6.11** Grain size distribution of Ni-Ag-SnO<sub>2</sub> after isothermal annealing at 300 °C for 10 h. The unimodal, lognormal nature of the experimental data suggests that a normal growth process took place.

## 6.4 Conclusions

The thermal stability of the Ni-Ag-SnO<sub>2</sub> composite was evaluated by analysing the microstructure evolution during and after different annealing treatments. Two types of pure-Ni films (coarse and fine-grained) were also studied for comparison and analysis purposes. The main results are summarised next.

- The microstructure evolution of both pure-Ni and composite films exhibited similar behaviour during non-isothermal annealing: slow kinetics from 100 to 250 °C, then a fast growth up to 350 °C and finally a deceleration and most likely stagnation from there onwards.
- Both pure-Ni films changed from a  $\langle 100 \rangle$  to a  $\langle 111 \rangle$  fibre texture during both non-isothermal and isothermal annealing (the latter at 500 °C), driven by surface energy minimisation. The Ni-Ag-SnO<sub>2</sub> retained its random orientation, showing better thermal stability in this aspect. This resulted from the minimisation of interface energy in combination with the random spatial orientation of the Ag-coated nanowires.
- Both pure-Ni films showed an increment in the average grain size of about 300% after isothermal annealing at 500 °C, which for the composite was only 70%. This resulted from the strong pinning forces exerted by the Ag-SnO<sub>2</sub> on the migrating grain boundaries of the Ni matrix. EBSD analysis revealed that the oriented nucleation mechanism (instead of oriented growth) governed the recrystallization of the films.

- Pure-Ni films underwent abnormal growth during isothermal annealing at 300 °C. This was not the case of Ni-Ag-SnO<sub>2</sub>, which exhibited a unimodal, lognormal grain size distribution.

## 7 Electrical resistivity evaluation

### 7.1 Introduction

Electrical resistivity is a key property of metals and metallic materials for electrical and electronic applications. A low resistivity is not only important for improving the electrical efficiency of devices by minimising the dissipation of energy into heat, but also for avoiding material degradation which might lead to failure during operation. As a matter of fact, significant Joule heating could result in the deterioration of mechanical properties due to, for instance, recrystallization and grain growth [284]; crack formation and propagation under thermal cycling [285]; electromigration [286,287]; and local melting of material, which might produce the welding of mobile parts [288].

In the case of metal matrix composites, an effective resistive medium is formed by its constituents, namely the matrix and its reinforcing or secondary phases (and eventually porosity). Besides the intrinsic specific resistance of each phase, the effective electrical resistivity is influenced by the shape, arrangement, size and volume fraction of the filler components [289]. Moreover, these characteristics play an active role in defining the magnitude of residual stresses and density of dislocations, which constitute energy barriers to the flow of electrons. For instance, a lower size of the reinforcement and a larger volume fraction result in higher stresses and dislocation density [290], as it is also the case of sharp corners with respect to flat surfaces [291].

The work described in this chapter dealt with the analysis of the electrical resistivity of the Ni-Ag-SnO<sub>2</sub> composite films, with emphasis on the effect or contribution of the reinforcing phases. To that end, Ni, Ag, and Ni-SnO<sub>2</sub>-nanowires samples were also investigated, which provided valuable information for understanding the individual contributions of their counterparts in the composite.

### 7.2 Experimental details

Ni-Ag-SnO<sub>2</sub> composite films were produced as described in 3.1, with the only exception being that SiO<sub>2</sub> wafers were used as substrate instead of steel sheets (for avoiding the flow of current through the substrate during the electrical resistivity measurements).

Ni, Ag and Ni-SnO<sub>2</sub>-nanowires samples were used for comparison and analysis purposes. The Ni and Ni-SnO<sub>2</sub> films were also deposited onto SiO<sub>2</sub> wafers. In both cases, Ni was electrodeposited using the same bath and experimental parameters as for the composite's matrix. Au nanoparticles were sputtered onto the SiO<sub>2</sub> substrate and the SnO<sub>2</sub> nanowires, respectively, in order to make their surface conductive for the Ni electrodeposition. Ag thin films of about 150 nm thickness were deposited onto borosilicate glass wafers, following the procedure described in 3.1.2 for coating the nanowires.

Electrical resistivity measurements were performed by means of the 4-point probe setup described in 3.2.9.

### 7.3 Results and discussion

The bulk electrical resistivity ( $\rho$ ) of the samples was calculated using the voltage ( $V$ ) measured at each applied current ( $I$ ) as

$$\rho = (\pi/\ln 2)t_f F_g (V/I), \quad (7.1)$$

where  $t_f$  denotes film thickness and  $F_g$  is a geometry factor. Each  $t_f$  was evaluated from several FIB cross-sections performed at different regions from all over the samples.  $F_g$  varies with the sample shape and dimensions as well as with the position and spacing of the probes on the surface. It assumed values between 0.93 and 0.95, which were obtained according to the early work from Smits [292].

The resulting  $\rho$  given by Eq. 7.1 are displayed in Fig. 7.1. At very low  $I$ , the flowing electrons followed paths close to the surface, leading to an enhanced scattering. Consequently, high values of  $\rho$  were obtained. For larger  $I$ , the penetration depth increased, reducing gradually  $\rho$  due to a lesser impact of surface effects. Finally,  $\rho$  stabilised around a fixed value (representative of the full thickness of the films) which is used here for the discussion and is also indicated in Fig. 7.1.

The Ni samples exhibited  $\rho$  of 76 n $\Omega$ ·m, being 10% higher than that of annealed bulk Ni (68 n $\Omega$ ·m at 20 °C [48]) and showing agreement with reports from other authors concerning electrodeposited Ni [293–295]. Taking this value as a reference, the Ni-SnO<sub>2</sub> films showed an increase of 50% which resulted from different factors. One of them was the presence of the highly resistive SnO<sub>2</sub> nanowires, whose  $\rho$  exceeds that of Ni by several orders of magnitude [131,296]. In such cases where the reinforcement is much more insulating than the

matrix, the electrical conduction takes place exclusively through the latter, while the secondary phase particles act as scattering sites.

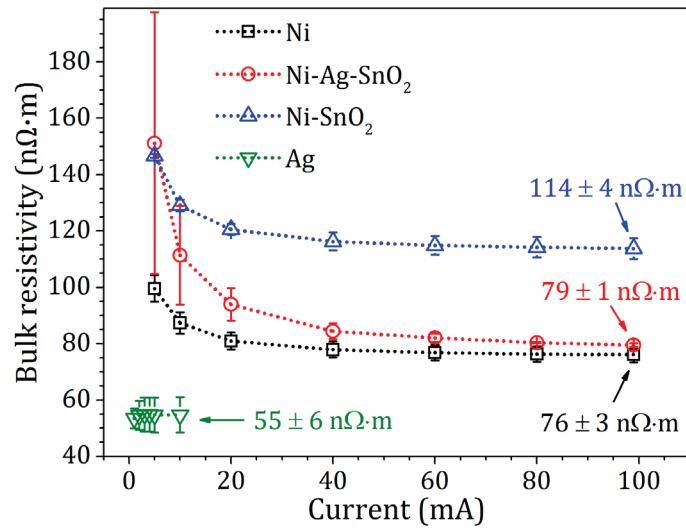


**Fig. 7.1** Results of the 4-point probe experiments, where the indicated values are the characteristic  $\rho$  of each type of sample. These were determined after the stabilisation of the measurements at maximum  $I$ . In the case of Ag, smaller  $I$  were required due to the much lower thickness of these films.

The relatively high  $\rho$  of the Ni-SnO<sub>2</sub> films was also attributed to the different defects present in the microstructure of the Ni matrix, which developed due to the introduction of the SnO<sub>2</sub> nanowires. For instance, the widespread porosity consisting of small to middle-sized pores (relative to film thickness; see Fig. 7.2) should have played a significant role in the observed behaviour. Moreover, the increased density of dislocations and grain boundaries associated to the fine-grained structure (induced by Zener pinning [152]) further contributed to that.

The Mayadas-Shatzkes model is commonly used for describing the influence of grain size on  $\rho$ . It regards grain boundaries as potential-energy barriers for incoming electrons [297,298]. Already at ultrafine grain sizes (> 100 nm), increased values of  $\rho$  have been reported for Ni [293,295,299]. However, the influence of grain boundaries would be largest at the lower end of the nanoscale, where grain diameters are about the same length as the electron's mean free path (between 1 and 15 nm). In terms of average size, this was clearly not the case of the grains of Ni-SnO<sub>2</sub> films. However, the regions with higher nanowire content (e.g., at the vicinity of the substrate) were likely to present a much larger population of such nano-sized grains.

For the Ni-Ag-SnO<sub>2</sub> composite, the calculated  $\rho$  was statistically equivalent to that of pure Ni, being 4% higher in terms of mean value. Therefore, a 31% reduction with respect to Ni-SnO<sub>2</sub> films was observed. Here, the detrimental effects described for the Ni-SnO<sub>2</sub> were counterbalanced by the introduction of the more conductive Ag phase (at the expense of Ni). Moreover, the impact of microstructural features (e.g., porosity and poor interfaces) should have been partly reduced, since the Ag coating of the nanowires provided a more suitable surface for the electrodeposition of Ni than the sputtered Au nanoparticles in the case of Ni-SnO<sub>2</sub>, resulting in a higher quality of the matrix.

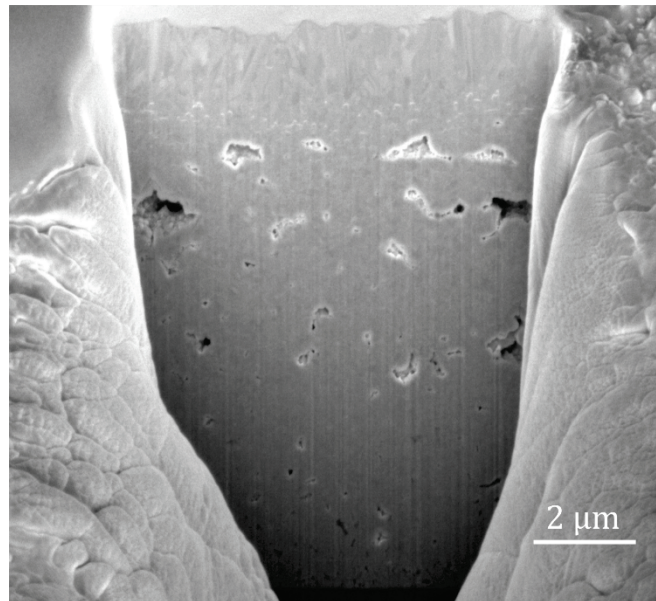


**Fig. 7.2** SEM micrograph showing the cross-section of a Ni-SnO<sub>2</sub> film.

The effect of Ag on the reduction of the composite's  $\rho$  was presumably lower than it could be expected. This was suggested by the relatively high  $\rho$  measured at Ag films of similar features and fabrication to those of nanowires' coatings. At 55 n $\Omega$ ·m, it was over three times that of annealed bulk Ag (16 n $\Omega$ ·m at 20 °C [48]). Responsible for this were the nanocrystalline morphology of the Ag deposits and their low thickness, which enhanced the effect of electron scattering at interfaces. Such scattering also takes place within the composite, since Ag is always in contact with SnO<sub>2</sub>. Moreover, interface scattering is not exclusively produced by insulating neighbour phases but also by highly conductive metallic ones (such as the Ni of the matrix) [300]. On another note, it is well established that thin electroless Ag deposits experience a reduction in  $\rho$  upon mild annealing [301,302]. Therefore, it should be possible to improve the performance of the composite in this way. This should be performed before

the electrodeposition of the Ni matrix, in order to avoid its grain growth and the associated softening of the composite films.

## **7.4 Conclusions**

The bulk electrical resistivity of Ni-Ag-SnO<sub>2</sub> films was evaluated by means of the 4-point method. Ni, Ag and Ni-SnO<sub>2</sub> samples were also studied in order to gain an understanding of the role played by the secondary phases. The findings of this analysis are outlined next.

- The Ni-Ag-SnO<sub>2</sub> composite exhibited  $\rho$  of  $79 \pm 1 \text{ n}\Omega\cdot\text{m}$ , similar to that of pure Ni films ( $76 \pm 3 \text{ n}\Omega\cdot\text{m}$ ) and 31% lower than that of Ni-SnO<sub>2</sub> ( $114 \pm 4 \text{ n}\Omega\cdot\text{m}$ ).
- The highly resistive SnO<sub>2</sub> nanowires and the microstructural defects induced by them in the matrix (i.e., porosity and higher density of grain boundaries and dislocations) degraded the performance of the composite. This was compensated by the introduction of the Ag phase, whose  $\rho$  was estimated at  $55 \pm 6 \text{ n}\Omega\cdot\text{m}$ .
- The relatively high  $\rho$  of the electroless Ag coatings on top of the nanowires might be reduced by mild annealing prior to the matrix deposition. This opens the possibility of an overall improvement in the composite.

## 8 Summary and outlook

### 8.1 Summary

This work dealt with the study of a novel composite film consisting of a Ni matrix reinforced with Ag-coated SnO<sub>2</sub> nanowires, which was developed as a candidate material for electrical contact applications.

As described in chapter 3, the fabrication method consisted of three main steps, starting with the synthesis of the SnO<sub>2</sub> nanowires. This was carried out by CVD, using Sn(O<sup>t</sup>Bu)<sub>4</sub> as the single precursor, where the developing nanostructures followed the VLS growth mechanism. This resulted in disordered arrays of high-aspect-ratio, single-crystalline nanowires, possessing about 100 nm diameter and several μm length. Next, these were coated with a Ag layer 100 to 200 nm thick (core/shell configuration) by means of the electroless technique, using Ag nitrate and D-glucose as Ag-ion source and reducing agent, respectively. Finally, the Ni matrix was galvanostatically deposited using a standard Ni sulfamate solution without enhancing additives. Films with thickness typically between 5 and 10 μm were successfully obtained through this process.

At the beginning of chapter 4, the microstructure of the samples was characterised mainly by FIB-assisted SEM (involving also EBSD), STEM and TEM. This revealed a gradient morphology with decreasing Ag-SnO<sub>2</sub> content towards the surface, where only the longest or straightest nanowires were able to extend. The (area-weighted) average grain size was found to be about 200 nm, which implied an 85% reduction with respect to Ni films produced with the same experimental parameters as the matrix (Ni<sub>cg</sub>). This was attributed to the grain boundary pinning by the secondary phases during the Ni deposition. The absence of crystallographic texture was another characteristic feature of the composite.

Chapter 4 proceeded then with the study of the mechanical properties of the films, which was performed by nanoindentation. With a relatively high hardness of 4.5 GPa, the Ni-Ag-SnO<sub>2</sub> was 66% harder than Ni<sub>cg</sub>, which was attributed to the grain-boundary strengthening. However, a certain degree of softening (17%) was observed with respect to Ni samples possessing similar grain size (Ni<sub>fg</sub>), associated to the softer nature of the Ag phase and porosity. The relatively low Young's modulus of Ni-Ag-SnO<sub>2</sub> (136 GPa) resulted from a reduced density (induced by the selected electrodeposition parameters) and from the influence of Ag (83 GPa). A straightforward method based on analytical and simulation results from other

authors was developed for characterising the stress-strain response of the materials from indentation data. Accordingly, the yield strength of the composite was calculated at 444 MPa, deviating from the Ni reference samples in a similar way as observed with the hardness. In all cases, the behaviour of the studied materials showed agreement with the Hall-Petch relationship.

Chapter 5 dealt with the tribological behaviour of the films. Friction and wear were evaluated in dry-sliding conditions in ambient air, using a linearly reciprocating ball-on-flat setup. This configuration simulated the fretting type of wear experienced by the electrodes of electrical contact devices. Ploughing-type abrasive wear was responsible for the plastic deformation of the samples. It was accompanied by the formation of an oxide-containing tribolayer (oxidative wear), whose composition was load-dependent. The Ni-Ag-SnO<sub>2</sub> displayed enhanced wear resistance with respect to the reference Ni samples (Ni<sub>cg</sub>), manifested by reductions in the wear volume (ranging between 50 and 80%). This was mostly attributed to the higher hardness of the composite. Moreover, numerical models were developed which allowed analysing the tribosystem's wear volume and rate. It was demonstrated that the observed ploughing wear can be accurately described by the geometry of the indenter in combination with traditional concepts related to the mechanical properties of the samples (like the power law of work hardening and the mathematical definition of indentation hardness). Regarding the dynamic friction coefficient, a reduction in its value was observed with increasing loads. This resulted from scale effects induced by strain gradients and the change in the involved microslip mechanism. Furthermore, the composite and the equally hard Ni samples (Ni<sub>fg</sub>) experienced a reduced friction at low loads with respect to Ni<sub>cg</sub>. This was attributed to their harder nature, which make them more resistant to adhesion and the formation of asperity junctions. Overall, the experimental evidence indicated that the effect of the Ag-SnO<sub>2</sub> phase on the tribological response of the composite was given exclusively by the increase in hardness induced by grain refinement.

In chapter 6, the thermal stability of the Ni-Ag-SnO<sub>2</sub> films was evaluated by analysing the evolution of the grain size and texture during different annealing treatments. Unlike the Ni reference samples, the composite retained its original (random) crystallographic orientation. This resulted from the minimisation of interface energy in combination with the random spatial orientation of the Ag-coated nanowires. Moreover, the average grain size increased 70% after 10 h annealing at 500 °C, which contrasted with the 300% observed for Ni films under the same conditions. The reason behind this was the strong pinning forces

exerted by the reinforcement on the migrating grain boundaries of the Ni matrix. In addition, EBSD analysis revealed that the oriented nucleation mechanism governed the recrystallization of the films.

At last, chapter 7 presented the study of the electrical resistivity of the composite, which was based on 4-point probe measurements. The bulk resistivity of Ni-Ag-SnO<sub>2</sub> was found to be quite similar to that of Ni films (79 and 76 nΩ·m, respectively). The highly conductive Ag phase compensated the insulating nature of both the SnO<sub>2</sub> nanowires and the microstructural defects induced by them in the matrix (i.e., porosity and higher density of grain boundaries and dislocations).

## **8.2 Outlook**

The results of the present work provide a detailed picture of the features and possibilities of the investigated composite films. However, several relevant topics remain still to be addressed, leaving the door open for further research. Some of these are listed next.

- Experimenting with additives in the electrodeposition bath (such as grain refiners and levelling agents) could lead to a substantial enhancement of the quality of the matrix. This could in turn result in avoiding the need of a polishing step and an overall improvement in several related material properties.
- Tailoring the composite's properties through the modification of the SnO<sub>2</sub> nanowires. For instance, as mentioned in chapter 2, doping with Sb can greatly increase the electrical conductivity of the nanostructures and even induce metallic-type conduction, which would result in an overall improvement for the composite. Moreover, the geometrical ordering of the nanowire arrays could be attempted. Straight, parallel wires/rods can be obtained by using dissolvable alumina membranes as templates during the CVD. Such configuration might induce a positive effect on both the electrical and elastoplastic properties.
- The Ni-Ag-SnO<sub>2</sub> composite should be further investigated concerning its performance against operation-related degrading phenomena. One possibility would be conducting corrosion tests at different aggressive environments. Regarding electrical-contact devices, switching experiments and welding tests would provide valuable information about the real potential of the material for its target field of application.

- Other composite films with different phase combinations could be fabricated with the multistep procedure developed in this work. The SnO<sub>2</sub>, Ag and even Ni could be replaced in the search of specific sets of properties. For instance, an interesting possibility would be using Ag as metal matrix, resulting in Ag-SnO<sub>2</sub> composite films. As stated in chapter 2, the bulk version of this material is widely applied in several electrical-contact devices.

## References

- [1] M. Braunovic, V. Konchits, N. Myshkin, *Electrical Contacts: Fundamentals, Applications and Technology*, CRC Press, Boca Raton, 2006.
- [2] T. Mutzel, M. Bender, R. Niederreuther, The effect of material composition on dynamic welding of electrical contacts, in: *2013 IEEE 59<sup>th</sup> Holm Conf. Electr. Contacts*, IEEE, 2013: pp. 1–7.
- [3] N. Talijan, V. Cosovic, J. Stajic-Trosic, A. Grujic, D. Zivkovic, E. Romhanji, Microstructure and properties of silver based cadmium free electrical contact materials, *J. Min. Metall. Sect. B Metall.* 43 (2007) 171–176.
- [4] T. Mützel, R. Niederreuther, Advanced silver-tin oxide contact materials for relay application, in: *26<sup>th</sup> Int. Conf. Electr. Contacts, IET*, 2012: pp. 194–199.
- [5] Davis J. R. (Ed.), *ASM Specialty Handbook: Nickel, Cobalt and their Alloys*, ASM International, 2000.
- [6] S. Noël, D. Alamarguy, A. Brézard-Oudot, P. Gendre, An investigation of fretting wear behaviour of nickel coatings for electrical contacts application in dry and lubricated conditions, *Wear.* 301 (2013) 551–561.
- [7] Y.F. Shen, W.Y. Xue, Y.D. Wang, Z.Y. Liu, L. Zuo, Mechanical properties of nanocrystalline nickel films deposited by pulse plating, *Surf. Coatings Technol.* 202 (2008) 5140–5145.
- [8] N.P. Wasekar, P. Haridoss, S.K. Seshadri, G. Sundararajan, Sliding wear behavior of nanocrystalline nickel coatings: Influence of grain size, *Wear.* 296 (2012) 536–546.
- [9] M. Singleton, P. Nash, The Ag–Ni (Silver-Nickel) system, *J. Phase Equilibria.* 8 (1987) 119–121.
- [10] H.O. Pierson, *Handbook of Chemical Vapor Deposition (CVD)*, 2nd ed., Noyes Publications, Norwich, 1999.
- [11] C. Chen, J. Liu, Z. Wang, Microstructure stability and evolution in CVD carbonyl Ni materials upon annealing – Grain growth and detwinning process, *Mater. Sci. Eng. A.* 558 (2012) 285–297.
- [12] L. Brissonneau, R. Sahnoun, C. Mijoule, C. Vahlas, Investigation of nickelocene decomposition during chemical vapor deposition of nickel, *J. Electrochem. Soc.* 147 (2000) 1443.
- [13] R.L. Van Hemert, L.B. Spendlove, R.E. Sievers, Vapor deposition of metals by hydrogen reduction of metal chelates, *J. Electrochem. Soc.* 112 (1965) 1123.
- [14] D.M. Mattox, *Handbook of Physical Vapor Deposition (PVD) Processing*, 2nd ed., Elsevier, Oxford, 2010.
- [15] K. Reichelt, X. Jiang, The preparation of thin films by physical vapour deposition methods, *Thin Solid Films.* 191 (1990) 91–126.
- [16] D.M. Mattox, Physical vapor deposition (PVD) processes, *Met. Finish.* 100 (2002) 394–408.

- [17] S. Berg, T. Nyberg, Fundamental understanding and modeling of reactive sputtering processes, *Thin Solid Films*. 476 (2005) 215–230.
- [18] P. Kelly, R. Arnell, Magnetron sputtering: A review of recent developments and applications, *Vacuum*. 56 (2000) 159–172.
- [19] K. Sarakinos, J. Alami, S. Konstantinidis, High power pulsed magnetron sputtering: A review on scientific and engineering state of the art, *Surf. Coatings Technol.* 204 (2010) 1661–1684.
- [20] S. Knauß, Schematischer Aufbau des Magnetronsputterns (modified), Licence: <http://creativecommons.org/licenses/by-sa/3.0/de>. (2008).
- [21] D. Manova, J.W. Gerlach, S. Mändl, Thin film deposition using energetic ions, *Materials*. 3 (2010) 4109–4141.
- [22] N. Kanani, *Electroplating – Basic Principles, Processes and Practice*, Elsevier, Oxford, 2004.
- [23] K.H. Krishnan, S. John, K.N. Srinivasan, J. Praveen, M. Ganesan, P.M. Kavimani, An overall aspect of electroless Ni-P depositions—A review article, *Metall. Mater. Trans. A*. 37 (2006) 1917–1926.
- [24] J. Sudagar, J. Lian, W. Sha, Electroless nickel, alloy, composite and nano coatings - A critical review, *J. Alloys Compd.* 571 (2013) 183–204.
- [25] A. Zielonka, H.A. Jehn, *Galvanische Schichten*, 3rd ed., Expert-Verlag, 2004.
- [26] J.A. McGeough, M.C. Leu, K.P. Rajurkar, A.K.M. de Silva, Q. Liu, Electroforming process and application to micro/macro manufacturing, *CIRP Ann. - Manuf. Technol.* 50 (2001) 499–514.
- [27] B.Q. Han, E.J. Lavernia, F.A. Mohamed, Mechanical properties of nanostructured materials, *Rev. Adv. Mater. Sci.* 9 (2005) 1–16.
- [28] C.C. Koch, Processing-structure-property relationships in ultrafine grain and nanocrystalline materials, *J. Phys. Conf. Ser.* 144 (2009) 012081.
- [29] M.S. Chandrasekar, M. Pushpavanam, Pulse and pulse reverse plating-Conceptual, advantages and applications, *Electrochim. Acta*. 53 (2008) 3313–3322.
- [30] H. Natter, R. Hempelmann, Nanocrystalline metals prepared by electrodeposition, *Zeitschrift Für Phys. Chemie*. 222 (2008) 319–354.
- [31] A.M. Rashidi, A. Amadeh, The effect of saccharin addition and bath temperature on the grain size of nanocrystalline nickel coatings, *Surf. Coatings Technol.* 204 (2009) 353–358.
- [32] A. Hovestad, L.J.J. Janssen, Electrochemical codeposition of inert particles in a metallic matrix, *J. Appl. Electrochem.* 25 (1995) 519–527.
- [33] *Nickel Plating Handbook*, Nickel Institute, 2014.
- [34] J.K. Dennis, T.E. Such, *Nickel and Chromium Plating*, 3rd ed., Woodhead Publishing, Cambridge, 1993.
- [35] R. Vilar, Laser cladding, *J. Laser Appl.* 11 (1999) 64.
- [36] L. Santo, Laser cladding of metals: A review, *Int. J. Surf. Sci. Eng.* 2 (2008) 327.

- [37] C.L. Sexton, G. Byrne, K.G. Watkins, Alloy development by laser cladding: An overview, *J. Laser Appl.* 13 (2001) 2.
- [38] Q. Ming, L.C. Lim, Z.D. Chen, Laser cladding of nickel-based hardfacing alloys, *Surf. Coatings Technol.* 106 (1998) 174–182.
- [39] L. Pawlowski, Finely grained nanometric and submicrometric coatings by thermal spraying: A review, *Surf. Coatings Technol.* 202 (2008) 4318–4328.
- [40] P. Fauchais, G. Montavon, Latest developments in suspension and liquid precursor thermal spraying, *J. Therm. Spray Technol.* 19 (2010) 226–239.
- [41] B.R. Marple, J. Voyer, J.F. Bisson, C. Moreau, Thermal spraying of nanostructured cermet coatings, *J. Mater. Process. Technol.* 117 (2001) 418–423.
- [42] C. Pierlot, L. Pawlowski, M. Bigan, P. Chagnon, Design of experiments in thermal spraying: A review, *Surf. Coatings Technol.* 202 (2008) 4483–4490.
- [43] J.A. Hearley, J.A. Little, A.J. Sturgeon, The erosion behaviour of NiAl intermetallic coatings produced by high velocity oxy-fuel thermal spraying, *Wear.* 233-235 (1999) 328–333.
- [44] M.L. Lau, H.G. Jiang, W. Nüchter, E.J. Lavernia, Thermal spraying of nanocrystalline Ni coatings, *Phys. Status Solidi.* 166 (1998) 257–268.
- [45] V.L. Tellkamp, M.L. Lau, A. Fabel, E.J. Lavernia, Thermal spraying of nanocrystalline inconel 718, *Nanostructured Mater.* 9 (1997) 489–492.
- [46] T.M. Pollock, S. Tin, Nickel-based superalloys for advanced turbine engines: Chemistry, microstructure and properties, *J. Propuls. Power.* 22 (2006) 361–374.
- [47] M. Van Schilfgaarde, I.A. Abrikosov, B. Johansson, Origin of the Invar effect of iron-nickel alloys, *Nature.* 400 (1999) 1–4.
- [48] ASM Handbook Vol. 2 – Properties and Selection: Nonferrous Alloys and Special-Purpose Materials, ASM International, 1992.
- [49] F. Pfeifer, C. Radeloff, Soft magnetic Ni-Fe and Co-Fe alloys – Some physical and metallurgical aspects, *J. Magn. Mater.* 19 (1980) 190–207.
- [50] K. Otsuka, X. Ren, Recent developments in the research of shape memory alloys, *Intermetallics.* 7 (1999) 511–528.
- [51] K. Otsuka, X. Ren, Physical metallurgy of Ti-Ni-based shape memory alloys, *Prog. Mater. Sci.* 50 (2005) 511–678.
- [52] Y.R. Jeng, P.C. Tsai, S.H. Chiang, Effects of grain size and orientation on mechanical and tribological characterizations of nanocrystalline nickel films, *Wear.* 303 (2013) 262–268.
- [53] G. Ma, J. Yang, Y. Liu, S. He, Z. Jiang, Friction and wear behavior of nanocrystalline nickel in air and vacuum, *Tribol. Lett.* 49 (2013) 481–490.
- [54] F. Ebrahimi, H.Q. Li, Structure and properties of electrodeposited nanocrystalline FCC Ni-Fe alloys, *Rev. Adv. Mater. Sci.* 5 (2003) 134–138.
- [55] S.D. Leith, S. Ramli, D.T. Schwartz, Characterization of  $\text{Ni}_x\text{Fe}_{1-x}$  ( $0.10 < x < 0.95$ ) electrodeposition from a family of sulfamate-chloride electrolytes, *J. Electrochem. Soc.* 146 (1999) 1431–1435.

- [56] C. Cheung, G. Palumbo, U. Erb, Synthesis of nanocrystalline permalloy by electrodeposition, *Scr. Metall. Mater.* 31 (1994) 735–740.
- [57] L. Wang, Y. Gao, Q. Xue, H. Liu, T. Xu, Microstructure and tribological properties of electrodeposited Ni–Co alloy deposits, *Appl. Surf. Sci.* 242 (2005) 326–332.
- [58] M. Srivastava, V. Ezhil Selvi, V.K. William Grips, K.S. Rajam, Corrosion resistance and microstructure of electrodeposited nickel–cobalt alloy coatings, *Surf. Coatings Technol.* 201 (2006) 3051–3060.
- [59] L. Shi, C. Sun, P. Gao, F. Zhou, W. Liu, Mechanical properties and wear and corrosion resistance of electrodeposited Ni–Co/SiC nanocomposite coating, *Appl. Surf. Sci.* 252 (2006) 3591–3599.
- [60] L. Shi, C. Sun, W. Liu, Electrodeposited nickel–cobalt composite coating containing MoS<sub>2</sub>, *Appl. Surf. Sci.* 254 (2008) 6880–6885.
- [61] L. Shi, C.F. Sun, P. Gao, F. Zhou, W.M. Liu, Electrodeposition and characterization of Ni–Co–carbon nanotubes composite coatings, *Surf. Coatings Technol.* 200 (2006) 4870–4875.
- [62] A.N. Correia, S.A.S. MacHado, Electrodeposition and characterization of thin layers of Ni–Co alloys obtained from dilute chloride baths, *Electrochim. Acta.* 45 (2000) 1733–1740.
- [63] A.A. Talin, E.A. Marquis, S.H. Goods, J.J. Kelly, M.K. Miller, Thermal stability of Ni–Mn electrodeposits, *Acta Mater.* 54 (2006) 1935–1947.
- [64] A. Stephen, T. Nagarajan, M. Ananth, Magnetization behaviour of electrodeposited Ni–Mn alloys, *Mater. Sci. Eng. B.* 55 (1998) 184–186.
- [65] A. Stephen, M. Ananth, V. Ravichandran, B. Narashiman, Magnetic properties of electrodeposited nickel–manganese alloys: Effect of Ni/Mn bath ratio, *J. Appl. Electrochem.* 30 (2000) 1313–1316.
- [66] S.H. Goods, J.J. Kelly, N.Y.C. Yang, Electrodeposited nickel–manganese: an alloy for microsystem applications, *Microsyst. Technol.* 10 (2004) 498–505.
- [67] E. Chassaing, N. Portail, A.F. Levy, G. Wang, Characterisation of electrodeposited nanocrystalline Ni–Mo alloys, *J. Appl. Electrochem.* 34 (2004) 1085–1091.
- [68] E. Beltowska-Lehman, A. Bigos, P. Indyka, M. Kot, Electrodeposition and characterisation of nanocrystalline Ni–Mo coatings, *Surf. Coatings Technol.* 211 (2012) 67–71.
- [69] N. Krstajic, V. Jovic, L. Gajickrstajic, B. Jovic, A. Antozzi, G. Martelli, Electrodeposition of Ni–Mo alloy coatings and their characterization as cathodes for hydrogen evolution in sodium hydroxide solution, *Int. J. Hydrogen Energy.* 33 (2008) 3676–3687.
- [70] S. Martinez, M. Metikoš-Huković, L. Valek, Electrocatalytic properties of electrodeposited Ni–15Mo cathodes for the HER in acid solutions: Synergistic electronic effect, *J. Mol. Catal. A Chem.* 245 (2006) 114–121.
- [71] K.H. Hur, J.H. Jeong, D.N. Lee, Microstructures and crystallization of electroless Ni–P deposits, *J. Mater. Sci.* 25 (1990) 2573–2584.

- [72] W. Sha, X. Wu, K.G. Keong, *Electroless Copper and Nickel-Phosphorus Plating*, Woodhead Publishing, Cambridge, 2011.
- [73] H. Ashassi-Sorkhabi, S.H. Rafizadeh, Effect of coating time and heat treatment on structures and corrosion characteristics of electroless Ni-P alloy deposits, *Surf. Coatings Technol.* 176 (2004) 318–326.
- [74] M. Palaniappa, S.K. Seshadri, Friction and wear behavior of electroless Ni-P and Ni-W-P alloy coatings, *Wear.* 265 (2008) 735–740.
- [75] I. Baskaran, R. Sakthi Kumar, T.S.N. Sankara Narayanan, A. Stephen, Formation of electroless Ni-B coatings using low temperature bath and evaluation of their characteristic properties, *Surf. Coatings Technol.* 200 (2006) 6888–6894.
- [76] Y.W. Riddle, T.O. Bailerare, Friction and wear reduction via an Ni-B electroless bath coating for metal alloys, *Jom.* 57 (2005) 40–45.
- [77] K. Krishnaveni, T.S.N. Sankara Narayanan, S.K. Seshadri, Electroless Ni-B coatings: Preparation and evaluation of hardness and wear resistance, *Surf. Coatings Technol.* 190 (2005) 115–121.
- [78] N. Krasteva, V. Fotty, S. Armyanov, Thermal stability of Ni-P and Ni-Cu-P amorphous alloys, *J. Electrochem. Soc.* 141 (1994) 2864–2867.
- [79] Y. Liu, Q. Zhao, Study of electroless Ni-Cu-P coatings and their anti-corrosion properties, *Appl. Surf. Sci.* 228 (2004) 57–62.
- [80] C.Y. Lee, K.L. Lin, Solderability of electroless nickel alloys using wetting balance technique, *Jpn. J. Appl. Phys.* 33 (1994) 4708–4713.
- [81] C.J. Chen, K.L. Lin, The deposition and crystallization behaviors of electroless Ni-Cu-P deposits, *J. Electrochem. Soc.* 146 (1999) 137–140.
- [82] D.H. Kim, Soft magnetic films by electroless Ni-Co-P plating, *J. Electrochem. Soc.* 142 (1995) 3763.
- [83] Y. Gao, L. Huang, Z.J. Zheng, H. Li, M. Zhu, The influence of cobalt on the corrosion resistance and electromagnetic shielding of electroless Ni-Co-P deposits on Al substrate, *Appl. Surf. Sci.* 253 (2007) 9470–9475.
- [84] T.S.N. Sankara Narayanan, S. Selvakumar, A. Stephen, Electroless Ni-Co-P ternary alloy deposits: preparation and characteristics, *Surf. Coatings Technol.* 172 (2003) 298–307.
- [85] S.L. Wang, Studies of electroless plating of Ni-Fe-P alloys and the influences of some deposition parameters on the properties of the deposits, *Surf. Coatings Technol.* 186 (2004) 372–376.
- [86] S.K. Tien, J.G. Duh, Y.I. Chen, Structure, thermal stability and mechanical properties of electroless Ni-P-W alloy coatings during cycle test, *Surf. Coatings Technol.* 177-178 (2004) 532–536.
- [87] Y. Gao, Z. Zheng, M. Zhu, C. Luo, Corrosion resistance of electrolessly deposited Ni-P and Ni-W-P alloys with various structures, *Mater. Sci. Eng. A.* 381 (2004) 98–103.
- [88] D.L. Song, Y. Li, L.L. Yang, Preparation and process optimization of Ni-Tl-B coating with fretting damage resistance, *Adv. Mater. Res.* 139-141 (2010) 460–463.

- [89] D. Song, L. Yang, Study on the alleviating fretting wear property of Ni-Tl-B coatings, in: 2010 Int. Conf. Mech. Autom. Control Eng., IEEE, 2010: pp. 3856–3859.
- [90] H. Shimauchi, Preparation of Ni-Sn alloys by an electroless-deposition method, *J. Electrochem. Soc.* 141 (1994) 1471.
- [91] M.G. Alvarez, S.M. Vazquez, F. Audebert, H. Sirkin, Corrosion behaviour of Ni-B-Sn amorphous alloys, *Scr. Mater.* 39 (1998) 661–668.
- [92] V.V. Reddy, B. Ramamoorthy, P.K. Nair, A study on the wear resistance of electroless Ni-P/Diamond composite coatings, *Wear.* 239 (2000) 111–116.
- [93] S. Zhang, K. Han, L. Cheng, The effect of SiC particles added in electroless Ni-P plating solution on the properties of composite coatings, *Surf. Coatings Technol.* 202 (2008) 2807–2812.
- [94] Y. Wu, H. Liu, B. Shen, L. Liu, W. Hu, The friction and wear of electroless Ni-P matrix with PTFE and/or SiC particles composite, *Tribol. Int.* 39 (2006) 553–559.
- [95] G. Straffelini, D. Colombo, A. Molinari, Surface durability of electroless Ni-P composite deposits, *Wear.* 236 (1999) 179–188.
- [96] J.N. Balaraju, S.K. Seshadri, M.S. Division, N.A. Laboratories, M. Centre, Electroless Ni-P composite coatings, *J. Appl. Electrochem.* 33 (2003) 807–816.
- [97] J.N. Balaraju, T.S.N.S. Narayanan, S.K. Seshadri, Structure and phase transformation behaviour of electroless Ni-P composite coatings, *Mater. Res. Bull.* 41 (2006) 847–860.
- [98] R.D. Malucci, Overview: connector contact quality, in: *Proc. 35<sup>th</sup> Meet. IEEE Holm Conf. Electr. Contacts*, IEEE, 1989: p. 95.
- [99] P.G. Slade, Y.K. Chien, J.A. Bindas, Switching performance of AgW-Ag(Sn,In)O and AgW-AgSnO<sub>2</sub> contact pairs, in: *Proc. 35<sup>th</sup> Meet. IEEE Holm Conf. Electr. Contacts*, IEEE, 1989: pp. 53–67.
- [100] K. Pechrach, J.W. McBride, P.M. Weaver, Arc root mobility on piezo-actuated contacts in miniature circuit breakers, in: *Proc. 49<sup>th</sup> IEEE Holm Conf. Electr. Contacts*, IEEE, 2005: pp. 76–83.
- [101] Y. Huang, W. Wen, C. Lin, G. Jin, C. Tang, L. Hao, G. Tian, J. Zhong, Research on an intelligent operating mechanism of high voltage circuit breaker, in: *2014 IEEE 60<sup>th</sup> Holm Conf. Electr. Contacts*, IEEE, 2014: pp. 1–5.
- [102] R.F. Stinson, J.A. Sarro, The use of carbon fiber composites in sliding contacts, in: *Proc. 48<sup>th</sup> IEEE Holm Conf. Electr. Contacts*, IEEE, 2002: pp. 175–183.
- [103] C. Holzapfel, Selected aspects of the electrical behavior in sliding electrical contacts, in: *2011 IEEE 57<sup>th</sup> Holm Conf. Electr. Contacts*, IEEE, 2011: pp. 1–9.
- [104] G.F. Dorsey, D.S. Coleman, B.K. Witherspoon, High speed data across sliding electrical contacts, in: *2012 IEEE 58<sup>th</sup> Holm Conf. Electr. Contacts*, IEEE, 2012: pp. 1–12.
- [105] C.B. Shao, J.G. Zhang, Electric contact behavior of Cu-Sn intermetallic compound formed in tin platings, in: *Proc. 44<sup>th</sup> IEEE Holm Conf. Electr. Contacts*, IEEE, 1998: pp. 26–33.

- [106] N. Dzektsler, V. Izmailov, L. Sargsian, Welding of aluminum alloy lugs to aluminum cables, in: Proc. 41<sup>st</sup> IEEE Holm Conf. Electr. Contacts, IEEE, 1995: pp. 17–20.
- [107] W. Johler, High temperature resistant gold alloys for switching signal relay contacts, in: Proc. 54<sup>th</sup> IEEE Holm Conf. Electr. Contacts, IEEE, 2008: pp. 35–40.
- [108] M.L. Trudeau, M. Braunovic, K.J. Bryden, J.Y. Ying, Fretting studies of nanocrystalline Pd, Pd-Ag and Pd-Y films, in: Proc. 42<sup>nd</sup> IEEE Holm Conf. Electr. Contacts jt. with 18<sup>th</sup> Int. Conf. Electr. Contacts, IEEE, 1996: pp. 383–394.
- [109] P.G. Slade, Electrical Contacts: Principles and Applications, 1st ed., CRC Press, 1999.
- [110] R. Shirakawa, S. Suzuki, A. Matsuda, N. Shibata, Cd-free silver alloy for sliding contact, in: Proc. 38<sup>th</sup> IEEE Holm Conf. Electr. Contacts, IEEE, 1992: pp. 119–124.
- [111] N. Yanagihara, O. Sakaguchi, T. Yamamoto, Development of AgNi contact material, in: Proc. 23<sup>rd</sup> Int. Conf. Electr. Contacts, 2006: pp. 266–271.
- [112] R. Michal, K.E. Saeger, Application of silver-based contact materials in air-break switching devices for power engineering, in: Proc. 34<sup>th</sup> Meet. IEEE Holm Conf. Electr. Contacts, IEEE, 1988: pp. 121–127.
- [113] P. Braumann, A. Koffler, The influence of manufacturing process, metal oxide content, and additives on the switching behaviour of Ag/SnO<sub>2</sub> in relays, in: Proc. 50<sup>th</sup> IEEE Holm Conf. Electr. Contacts jt. with 22<sup>nd</sup> Int. Conf. Electr. Contacts Electr. Contacts, 2004, IEEE, 2004: pp. 90–97.
- [114] J. Aronstein, Evaluation of an aluminum conductor material for branch circuit applications, in: Proc. 33<sup>rd</sup> IEEE Holm Conf. Electr. Contacts, 1987: pp. 107–112.
- [115] M.A. Farahat, E. Gockenbach, A.A. El-Alaily, M.M. Abdel Aziz, Effect of coating materials on the electrical performance of copper joints, in: Proc. 42<sup>nd</sup> IEEE Holm Conf. Electr. Contacts jt. with 18<sup>th</sup> Int. Conf. Electr. Contacts, IEEE, 1996: pp. 472–478.
- [116] S. Benhenda, N. Benjemaa, M. Bourir, Effect of pulse plating parameters on electrical contact behaviour of nickel coatings, in: Proc. 39<sup>th</sup> IEEE Holm Conf. Electr. Contacts, IEEE, 1993: pp. 219–223.
- [117] M. Antler, Corrosion control and lubrication of plated noble metal connector contacts, IEEE Trans. Components, Packag. Manuf. Technol. Part A. 19 (1996) 304–312.
- [118] J. Xu, U. Herr, T. Klassen, R.S. Averback, Formation of supersaturated solid solutions in the immiscible Ni–Ag system by mechanical alloying, J. Appl. Phys. 79 (1996) 3935.
- [119] C. Srivastava, B.M. Mundotiya, Morphology dependence of Ag-Ni solid solubility, Electrochem. Solid-State Lett. 15 (2011) K10–K15.
- [120] C.L. Wang, S.Z. Lin, Y. Niu, W.T. Wu, Z.L. Zhao, Microstructural properties of bulk nanocrystalline Ag-Ni alloy prepared by hot pressing of mechanically pre-alloyed powders, Appl. Phys. A Mater. Sci. Process. 76 (2003) 157–163.
- [121] C. Srivastava, B.M. Mundotiya, Size and solid solubility in electrodeposited Ag-Ni nanoparticles, Mater. Sci. Forum. 736 (2012) 21–26.
- [122] C.Y. Tung, H.M. Lin, J.M. Gu, P.Y. Lee, Preparation of nanocrystalline Ag-Ni particles by gas condensation method, Nanostructured Mater. 9 (1997) 117–120.

- [123] M.A. Meyers, K.K. Chawla, *Mechanical Behavior of Materials*, 2nd ed., Cambridge University Press, New York, 2009.
- [124] C.C. Lee, D.H. Chen, Large-scale synthesis of Ni-Ag core-shell nanoparticles with magnetic, optical and anti-oxidation properties, *Nanotechnology*. 17 (2006) 3094–3099.
- [125] D.H. Chen, S.R. Wang, Protective agent-free synthesis of Ni-Ag core-shell nanoparticles, *Mater. Chem. Phys.* 100 (2006) 468–471.
- [126] S. Senapati, S.K. Srivastava, S.B. Singh, H.N. Mishra, Magnetic Ni/Ag core-shell nanostructure from prickly Ni nanowire precursor and its catalytic and antibacterial activity, *J. Mater. Chem.* 22 (2012) 6899.
- [127] H.W. Jang, S.Y. Kim, J.L. Lee, Mechanism for ohmic contact formation of oxidized Ni/Au on p-type GaN, *J. Appl. Phys.* 94 (2003) 1748.
- [128] Z. Hassan, Y.C. Lee, F.K. Yam, Z.J. Yap, N. Zainal, H. Abu Hassan, K. Ibrahim, Thermal stability of Ni/Ag contacts on p-type GaN, *Phys. Status Solidi*. 1 (2004) 2528–2532.
- [129] C.H. Chou, C.L. Lin, Y.C. Chuang, H.Y. Bor, C.Y. Liu, High thermally stable Ni/Ag(Al) alloy contacts on p-GaN, *Appl. Phys. Lett.* 90 (2007) 022103.
- [130] Ç. Kılıç, A. Zunger, Origins of coexistence of conductivity and transparency in SnO<sub>2</sub>, *Phys. Rev. Lett.* 88 (2002) 7–10.
- [131] Q. Wan, E. Dattoli, W. Lu, Doping-dependent electrical characteristics of SnO<sub>2</sub> nanowires, *Small*. 4 (2008) 451–454.
- [132] Q. Wan, T.H. Wang, Single-crystalline Sb-doped SnO<sub>2</sub> nanowires: synthesis and gas sensor application, *Chem. Commun. (Camb)*. 1 (2005) 3841–3.
- [133] M. Batzill, U. Diebold, The surface and materials science of tin oxide, *Prog. Surf. Sci.* 79 (2005) 47–154.
- [134] T. Hyodo, N. Nishida, Y. Shimizu, M. Egashira, Preparation and gas-sensing properties of thermally stable mesoporous SnO<sub>2</sub>, *Sensors Actuators B Chem.* 83 (2002) 209–215.
- [135] N. Barsan, U. Weimar, Understanding the fundamental principles of metal oxide based gas sensors; the example of CO sensing with SnO<sub>2</sub> sensors in the presence of humidity, *J. Phys. Condens. Matter*. 15 (2003) R813–R839.
- [136] Z.R. Dai, J.L. Gole, J.D. Stout, Z.L. Wang, Tin oxide nanowires, nanoribbons, and nanotubes, *J. Phys. Chem. B*. 106 (2002) 1274–1279.
- [137] J. Pan, H. Shen, S. Mathur, One-dimensional SnO<sub>2</sub> nanostructures: synthesis and applications, *J. Nanotechnol.* 2012 (2012) 1–12.
- [138] R.S. Wagner, W.C. Ellis, Vapor-liquid-solid mechanism of single crystal growth, *Appl. Phys. Lett.* 4 (1964) 89.
- [139] X. Wei, D.K. Roper, Tin sensitization for electroless plating review, *J. Electrochem. Soc.* 161 (2014) D235–D242.

- [140] J.F. Silvain, O. Fouassier, S. Lescaux, Atomic force microscopy and x-ray photoelectron spectroscopy investigations of the morphology and chemistry of a PdCl<sub>2</sub>/SnCl<sub>2</sub> electroless plating catalysis system adsorbed onto shape memory alloy particles, *J. Appl. Phys.* 96 (2004) 4945.
- [141] B. Huang, W. Gan, G. Guo, Y. Li, T. Lin, X. Liu, Electroless silver plating on Pb-based glass frits by a one-step activation method without stannum and palladium, *Ceram. Int.* (2013) 1–5.
- [142] H.C. Koo, S.Y. Kim, S.K. Cho, J.J. Kim, Ag seed-layer formation by electroless plating for ultra-large-scale integration interconnection, *J. Electrochem. Soc.* 155 (2008) D558.
- [143] H. Zhang, X. Zou, J. Liang, X. Ma, Z. Tang, J. Sun, Development of electroless silver plating on para-aramid fibers and growth morphology of silver deposits, *J. Appl. Polym. Sci.* 124 (2012) 3363–3371.
- [144] W.C. Oliver, G.M. Pharr, An improved technique for determining hardness and elastic modulus using load and displacement sensing indentation experiments, *J. Mater. Res.* 7 (1992) 1564–1583.
- [145] W.C. Oliver, G.M. Pharr, Measurement of hardness and elastic modulus by instrumented indentation: Advances in understanding and refinements to methodology, *J. Mater. Res.* 19 (2011) 3–20.
- [146] Metallic materials - Instrumented indentation test for hardness and materials parameters - Part 4: Test method for metallic and non-metallic coatings, DIN EN ISO 14577-4. (2007).
- [147] T. Borkar, S.P. Harimkar, Effect of electrodeposition conditions and reinforcement content on microstructure and tribological properties of nickel composite coatings, *Surf. Coatings Technol.* 205 (2011) 4124–4134.
- [148] K. Schöler, B. Philippi, M. Weinmann, V.M. Marx, H. Vehoff, Effects of processing on texture, internal stresses and mechanical properties during the pulsed electrodeposition of nanocrystalline and ultrafine-grained nickel, *Acta Mater.* 61 (2013) 3945–3955.
- [149] F. Yang, W. Tian, H. Nakano, H. Tsuji, S. Oue, H. Fukushima, Effect of Current Density and Organic Additives on the Texture and Hardness of Ni Electrodeposited from sulfamate and Watt's Solutions, *Mater. Trans.* 51 (2010) 948–956.
- [150] E.O. Hall, The deformation and ageing of Mild steel: III Discussion of results, *Proc. Phys. Soc. Sect. B.* 64 (1951) 747–753.
- [151] N.J. Petch, The cleavage strength of polycrystals, *J. Iron Steel Inst.* 174 (1953) 25–28.
- [152] C.S. Smith, Zener pinning, *Met. Technol. Trans. Metall. Soc.* (1948) 15–51.
- [153] M. Hillert, Inhibition of grain growth by second-phase particles, *Acta Metall.* 36 (1988) 3177–3181.
- [154] J.A. Bearden, X-ray wavelengths, *Rev. Mod. Phys.* 39 (1967) 78–124.
- [155] J.C. Russ, R.T. Dehoff, *Practical Stereology*, 2nd ed., Plenum Press, New York, 1999.
- [156] J. Ohser, F. Mücklich, *Statistical Analysis of Microstructures in Materials Science*, Wiley, 2000.

- [157] R. Mishra, B. Basu, R. Balasubramaniam, Effect of grain size on the tribological behavior of nanocrystalline nickel, *Mater. Sci. Eng. A*. 373 (2004) 370–373.
- [158] L.S. Stephens, K.W. Kelly, S. Simhadri, A.B. McCandless, E.I. Meletis, Mechanical property evaluation and failure analysis of cantilevered LIGA nickel microposts, *J. Microelectromechanical Syst.* 10 (2001) 347–359.
- [159] C.S. Lin, P.C. Hsu, L. Chang, C.H. Chen, Properties and microstructure of nickel electrodeposited from a sulfamate bath containing ammonium ions, *J. Appl. Electrochem.* 31 (2001) 925–933.
- [160] I. Kim, D.Y. Sung, B.H. Park, M.G. Lee, Texture of Electrodeposited Ni Films, *Mater. Sci. Forum.* 449-452 (2004) 565–568.
- [161] F. Ebrahimi, G.R. Bourne, M.S. Kelly, T.E. Matthews, Mechanical properties of nanocrystalline nickel produced by electrodeposition, *Nanostructured Mater.* 11 (1999) 343–350.
- [162] D.N. Lee, Texture development in thin films, *Mater. Sci. Forum.* 408-412 (2002) 75–94.
- [163] N.A. Pangarov, On the crystal orientation of electrodeposited metals, *Electrochim. Acta.* 9 (1964) 721–726.
- [164] N.A. Pangarov, Preferred orientations in electro-deposited metals, *J. Electroanal. Chem.* 9 (1965) 70–85.
- [165] G. Kaupp, *Atomic Force Microscopy, Scanning Nearfield Optical Microscopy and Nanoscratching: Application to Rough and Natural Surfaces*, Springer, Berlin, 2006.
- [166] M. Kato, Hall-Petch relationship and dislocation model for deformation of ultrafine-grained and nanocrystalline metals, *Mater. Trans.* 55 (2014) 19–24.
- [167] G.A. Malygin, Plasticity and strength of micro- and nanocrystalline materials, *Phys. Solid State.* 49 (2007) 1013–1033.
- [168] M.A. Meyers, A. Mishra, D.J. Benson, Mechanical properties of nanocrystalline materials, *Prog. Mater. Sci.* 51 (2006) 427–556.
- [169] J.D. Eshelby, F.C. Frank, F.R.N. Nabarro, XLI. The equilibrium of linear arrays of dislocations, London, Edinburgh, Dublin *Philos. Mag. J. Sci.* 42 (2010) 351–364.
- [170] J.C.M. Li, Petch Relation and Grain Boundary Sources, *Trans. Metall. Soc. AIME.* 227 (1963) 239.
- [171] M.F. Ashby, The deformation of plastically non-homogeneous materials, *Philos. Mag.* 21 (1970) 399–424.
- [172] C.E. Carlton, P.J. Ferreira, What is behind the inverse Hall-Petch effect in nanocrystalline materials?, *Acta Mater.* 55 (2007) 3749–3756.
- [173] W.F. Hosford, *Mechanical Behavior of Materials*, Cambridge University Press, New York, 2005.
- [174] S. Kibey, J.B. Liu, D.D. Johnson, H. Sehitoglu, Predicting twinning stress in fcc metals: Linking twin-energy pathways to twin nucleation, *Acta Mater.* 55 (2007) 6843–6851.

- [175] A. Godon, J. Creus, S. Cohendoz, E. Conforto, X. Feaugas, P. Girault, C. Savall, Effects of grain orientation on the Hall-Petch relationship in electrodeposited nickel with nanocrystalline grains, *Scr. Mater.* 62 (2010) 403–406.
- [176] O. Arnould, O. Hubert, F. Hild, Abnormal grain growth effects on the mechanical behavior of Ni electrodeposits, *Mater. Sci. Forum.* 467-470 (2004) 957–962.
- [177] T. Otit, Y. Cao, S.M. Allameh, Z. Zong, O. Akogwu, W.O. Soboyejo, Nanoindentation measurements of the mechanical properties of Ni thin films: Effects of film microstructure and substrate modulus, *Mater. Manuf. Process.* 22 (2007) 195–205.
- [178] J.D. Giallonardo, U. Erb, K.T. Aust, G. Palumbo, The influence of grain size and texture on the Young's modulus of nanocrystalline nickel and nickel-iron alloys, *Philos. Mag.* 91 (2011) 4594–4605.
- [179] J.K. Luo, A.J. Flewitt, S.M. Spearing, N.A. Fleck, W.I. Milne, Young's modulus of electroplated Ni thin film for MEMS applications, *Mater. Lett.* 58 (2004) 2306–2309.
- [180] M. Wang, N. Pan, Predictions of effective physical properties of complex multiphase materials, *Mater. Sci. Eng. R Reports.* 63 (2008) 1–30.
- [181] J.B. Watchman, Elastic deformation of ceramics and other refractory materials, in: *Mech. Therm. Prop. Ceram. Proc.*, National Bureau of Standards, Washington, 1969: pp. 139–168.
- [182] J.K. Mackenzie, The elastic constants of a solid containing spherical holes, *Proc. Phys. Soc. Sect. B.* 63 (2002) 2–11.
- [183] A. Reuss, Berechnung der Fließgrenze von Mischkristallen auf Grund der Plastizitätsbedingung für Einkristalle, *ZAMM - J. Appl. Math. Mech./Zeitschrift Für Angew. Math. Und Mech.* 9 (1929) 49–58.
- [184] Z.S. Ma, Y.C. Zhou, S.G. Long, C.S. Lu, An inverse approach for extracting elastic-plastic properties of thin films from small scale sharp indentation, *J. Mater. Sci. Technol.* 28 (2012) 626–635.
- [185] Z.S. Ma, Y.C. Zhou, S.G. Long, X.L. Zhong, C. Lu, Characterization of stress-strain relationships of elastoplastic materials: An improved method with conical and pyramidal indenters, *Mech. Mater.* 54 (2012) 113–123.
- [186] M. Dao, N. Chollacoop, K.J. Van Vliet, T.A. Venkatesh, S. Suresh, Computational modeling of the forward and reverse problems in instrumented sharp indentation, *Acta Mater.* 49 (2001) 3899–3918.
- [187] Z. Yuan, F. Li, B. Chen, F. Xue, The correlation between indentation hardness and material properties with considering size effect, *J. Mater. Res.* 29 (2014) 1317–1325.
- [188] Z. Hu, K. Lynne, F. Delfanian, Characterization of materials' elasticity and yield strength through micro-/nano-indentation testing with a cylindrical flat-tip indenter, *J. Mater. Res.* 30 (2015) 578–591.
- [189] J.R. Matthews, Indentation hardness and hot pressing, *Acta Metall.* 28 (1980) 311–318.
- [190] X. Hernot, O. Bartier, Y. Bekouche, R. El Abdi, G. Mauvoisin, Influence of penetration depth and mechanical properties on contact radius determination for spherical indentation, *Int. J. Solids Struct.* 43 (2006) 4136–4153.

- [191] R. Hill, B. Storakers, A.B. Zdunek, A theoretical study of the brinell hardness test, *Proc. R. Soc. A Math. Phys. Eng. Sci.* 423 (1989) 301–330.
- [192] D. Tabor, *The Hardness of Metals*, Oxford University Press, New York, 1951.
- [193] P. Zhang, S.X. Li, Z.F. Zhang, General relationship between strength and hardness, *Mater. Sci. Eng. A.* 529 (2011) 62–73.
- [194] Y. Cheng, C. Cheng, Scaling approach to conical indentation in elastic-plastic solids with work hardening, *J. Appl. Phys.* 84 (1998) 1284.
- [195] K. Holmberg, A. Matthews, *Coatings Tribology: Properties, Mechanisms, Techniques and Applications in Surface Engineering*, 2nd ed., Elsevier, Oxford, 2009.
- [196] D.H. Jeong, F. Gonzalez, G. Palumbo, K.T. Aust, U. Erb, The effect of grain size on the wear properties of electrodeposited nanocrystalline nickel coatings, *Scr. Mater.* 44 (2001) 493–499.
- [197] A.M. Pillai, A. Rajendra, A.K. Sharma, Evaluation of effect of grain size on mechanical and tribological properties of pulse electrodeposited nanocrystalline nickel using nanoindentation techniques, *Trans. IMF.* 90 (2012) 143–148.
- [198] M. Shafiei, A.T. Alpas, friction and wear mechanisms of nanocrystalline Nickel in ambient and inert atmospheres, *Metall. Mater. Trans. A.* 38 (2007) 1621–1631.
- [199] T. Kayaba, K. Hokkirigawa, K. Kato, Analysis of the abrasive wear mechanism by successive observations of wear processes in a scanning electron microscope, *Wear.* 110 (1986) 419–430.
- [200] *ASM Handbook Vol. 18 – Friction, Lubrication, and Wear Technology*, ASM International, 1992.
- [201] K.H. Zum Gahr, *Microstructure and Wear of Materials*, Elsevier, Amsterdam, 1987.
- [202] D.A. Rigney, Transfer, mixing and associated chemical and mechanical processes during the sliding of ductile materials, *Wear.* 245 (2000) 1–9.
- [203] P.J. Blau, *Friction Science and Technology: From Concepts to Applications*, 2nd ed., CRC Press, Boca Raton, 2009.
- [204] J. Rösler, H. Harders, M. Bäker, *Mechanical Behaviour of Engineering Materials: Metals, Ceramics, Polymers and Composites*, Springer, Berlin, 2007.
- [205] B. Yao, Z. Han, K. Lu, Correlation between wear resistance and subsurface recrystallization structure in copper, *Wear.* 294-295 (2012) 438–445.
- [206] H. Xiao, T. Senda, E. Yasuda, Dynamic recrystallization during the sliding wear of alumina at elevated temperatures, *J. Am. Ceram. Soc.* 79 (1996) 3243–3249.
- [207] C. Rynio, H. Hattendorf, J. Klöwer, G. Eggeler, The evolution of tribolayers during high temperature sliding wear, *Wear.* 315 (2014) 1–10.
- [208] Q. Guo-Zheng, Characterization for dynamic recrystallization kinetics based on stress-strain curves, in: P. Wilson (Ed.), *Recent Developments in the Study of Recrystallization*, InTech, 2013: pp. 61 – 88.
- [209] J.H. Dautzenberg, The role of dynamic recrystallization in dry sliding wear, *Wear.* 60 (1980) 401–411.

- [210] X. Chen, Z. Han, K. Lu, Enhancing wear resistance of Cu–Al alloy by controlling subsurface dynamic recrystallization, *Scr. Mater.* 101 (2015) 76–79.
- [211] M. Kalin, Influence of flash temperatures on the tribological behaviour in low-speed sliding: A review, *Mater. Sci. Eng. A.* 374 (2004) 390–397.
- [212] D. Kuhlmann-Wilsdorf, Demystifying flash temperatures I. Analytical expressions based on a simple model, *Mater. Sci. Eng.* 93 (1987) 107–118.
- [213] G. Sutter, N. Ranc, Flash temperature measurement during dry friction process at high sliding speed, *Wear.* 268 (2010) 1237–1242.
- [214] M. Kalin, J. Vižintin, Comparison of different theoretical models for flash temperature calculation under fretting conditions, *Tribol. Int.* 34 (2001) 831–839.
- [215] H.A. Abdel-Aal, A remark on the flash temperature theory, *Int. Commun. Heat Mass Transf.* 24 (1997) 241–250.
- [216] M.F. Ashby, J. Abulawi, H.S. Kong, Temperature maps for frictional heating in dry sliding, *Tribol. Trans.* 34 (1991) 577–587.
- [217] J.F. Archard, The temperature of rubbing surfaces, *Wear.* 2 (1959) 438–455.
- [218] D. Kuhlmann-Wilsdorf, Flash temperatures due to friction and Joule heat at asperity contacts, *Wear.* 105 (1985) 187–198.
- [219] R. Holm, Calculation of the temperature development in a contact heated in the contact surface, and application to the problem of the temperature rise in a sliding contact, *J. Appl. Phys.* 19 (1948) 361–366.
- [220] E. Rabinowicz, *Friction and Wear of Materials*, Wiley, New York, 1965.
- [221] M.R. Drury, J.L. Urai, Deformation-related recrystallization processes, *Tectonophysics.* 172 (1990) 235–253.
- [222] L. Wang, Y. Gao, T. Xu, Q. Xue, A comparative study on the tribological behavior of nanocrystalline nickel and cobalt coatings correlated with grain size and phase structure, *Mater. Chem. Phys.* 99 (2006) 96–103.
- [223] *Tribology for Scientists and Engineers*, Springer, New York, 2013.
- [224] W.L. Li, N.R. Tao, Z. Han, K. Lu, Comparisons of dry sliding tribological behaviors between coarse-grained and nanocrystalline copper, *Wear.* 274-275 (2012) 306–312.
- [225] T.W. Scharf, A. Neira, J.Y. Hwang, J. Tiley, R. Banerjee, Self-lubricating carbon nanotube reinforced nickel matrix composites, *J. Appl. Phys.* 106 (2009) 013508.
- [226] D.H. Buckley, NASA technological memorandum TMX71781, (1975).
- [227] F.P. Bowden, D. Tabor, *The Friction and Lubrication of Solids, Part 2*, Oxford University Press, Oxford, 1964.
- [228] D.A. Rigney, J.P. Hirth, Plastic deformation and sliding friction of metals, *Wear.* 53 (1979) 345–370.
- [229] D.A. Rigney, W.A. Glaeser, The significance of near surface microstructure in the wear process, *Wear.* 46 (1978) 241–250.
- [230] B. Bhushan, M. Nosonovsky, Scale effects in friction using strain gradient plasticity and dislocation-assisted sliding (microslip), *Acta Mater.* 51 (2003) 4331–4345.

- [231] A. Carpinteri, M. Paggi, Size-scale effects on the friction coefficient, *Int. J. Solids Struct.* 42 (2005) 2901–2910.
- [232] Z. Rymuza, S. Pytko, The effect of scale in tribological testing, *J. Mater. Res. Technol.* 1 (2012) 13–20.
- [233] B. Bhushan, M. Nosonovsky, Comprehensive model for scale effects in friction due to adhesion and two- and three-body deformation (plowing), *Acta Mater.* 52 (2004) 2461–2474.
- [234] N.A. Fleck, G.M. Muller, M.F. Ashby, J.W. Hutchinson, Strain gradient plasticity: Theory and experiment, *Acta Metall. Mater.* 42 (1994) 475–487.
- [235] W.D. Nix, H. Gao, Indentation size effects in crystalline materials: A law for strain gradient plasticity, *J. Mech. Phys. Solids.* 46 (1998) 411–425.
- [236] J.A. Hurtado, K.S. Kim, Scale effects in friction of single-asperity contacts. I. From concurrent slip to single-dislocation-assisted slip, *Proc. R. Soc. A Math. Phys. Eng. Sci.* 455 (1999) 3363–3384.
- [237] J.A. Hurtado, K.S. Kim, Scale effects in friction of single-asperity contacts. II. Multiple-dislocation-cooperated slip, *Proc. R. Soc. A Math. Phys. Eng. Sci.* 455 (1999) 3385–3400.
- [238] J.F. Archard, Contact and rubbing of flat surfaces, *J. Appl. Phys.* 24 (1953) 981.
- [239] J.F. Archard, W. Hirst, The wear of metals under unlubricated conditions, *Proc. R. Soc. A Math. Phys. Eng. Sci.* 236 (1956) 397–410.
- [240] H.C. Meng, K.C. Ludema, Wear models and predictive equations: their form and content, *Wear.* 181-183 (1995) 443–457.
- [241] S.M. Hsu, M.C. Shen, A.W. Ruff, Wear prediction for metals, *Tribol. Int.* 30 (1997) 377–383.
- [242] C.A. Schuh, T.G. Nieh, T. Yamasaki, Hall–Petch breakdown manifested in abrasive wear resistance of nanocrystalline nickel, *Scr. Mater.* 46 (2002) 735–740.
- [243] S. Suárez, A. Rosenkranz, C. Gachot, F. Mücklich, Enhanced tribological properties of MWCNT/Ni bulk composites - Influence of processing on friction and wear behaviour, *Carbon N. Y.* 66 (2014) 164–171.
- [244] D.A. Rigney, Some thoughts on sliding wear, *Wear.* 152 (1992) 187–192.
- [245] ASTM, ASTM G133: Standard test method for linearly reciprocating ball-on-flat sliding wear, *ASTM Stand.* 05 (2010).
- [246] M. Thuvander, M. Abraham, A. Cerezo, G.D.W. Smith, Thermal stability of electrodeposited nanocrystalline nickel and iron–nickel alloys, *Mater. Sci. Technol.* 17 (2001) 961–970.
- [247] H.Q. Li, F. Ebrahimi, An investigation of thermal stability and microhardness of electrodeposited nanocrystalline nickel-21% iron alloys, *Acta Mater.* 51 (2003) 3905–3913.
- [248] C.S. Lin, P.C. Hsu, K.C. Peng, L. Chang, C.H. Chen, Annealing behavior of nickel electrodeposited from sulfamate bath at different temperatures., *Mater. Trans.* 42 (2001) 316–322.

- [249] M. Hourai, P. Holdway, A. Cerezo, G.D.W. Smith, Microstructure and thermal stability of electrodeposited nanocrystalline nickel, *Mater. Sci. Forum.* 386-388 (2002) 397–402.
- [250] C.S. Lin, C.Y. Lee, C.F. Chang, C.H. Chang, Annealing behavior of electrodeposited Ni-TiO<sub>2</sub> composite coatings, *Surf. Coatings Technol.* 200 (2006) 3690–3697.
- [251] U. Klement, U. Erb, A.M. El-Sherik, K.T. Aust, Thermal stability of nanocrystalline Ni, *Mater. Sci. Eng. A.* A203 (1995) 177–186.
- [252] N. Anifantis, A. Dimarogonas, Flash and bulk temperatures of gear teeth due to friction, *Mech. Mach. Theory.* 28 (1993) 159–164.
- [253] L. Morin, N.B. Jeman, D. Jeannot, Make arc erosion and welding in the automotive area, *IEEE Trans. Components Packag. Technol.* 23 (2000) 240–246.
- [254] S.Y. Chang, C.J. Hsu, C.H. Hsu, S.J. Lin, Investigation on the arc erosion behavior of new silver matrix composites: Part I. Reinforced by particles, *J. Mater. Res.* 18 (2003) 804–816.
- [255] C.V. Thompson, Grain growth in thin films, *Annu. Rev. Mater. Sci.* 20 (1990) 245–268.
- [256] F.J. Humphreys, M. Hatherly, *Recrystallization and Related Annealing Phenomena*, 2nd ed., Elsevier, Oxford, 2004.
- [257] A.D. Rollett, Overview of modeling and simulation of recrystallization, *Prog. Mater. Sci.* 42 (1997) 79–99.
- [258] F.J. Humphreys, Modelling microstructural evolution during annealing, *Model. Simul. Mater. Sci. Eng.* 8 (2000) 893–910.
- [259] H. Savaloni, M. Gholipour-Shahraki, M.A. Player, A comparison of different methods for x-ray diffraction line broadening analysis of Ti and Ag UHV deposited thin films: nanostructural dependence on substrate temperature and film thickness, *J. Phys. D. Appl. Phys.* 39 (2006) 2231–2247.
- [260] V. Soleimani, M. Mojtahedi, A comparison between different X-ray diffraction line broadening analysis methods for nanocrystalline ball-milled FCC powders, *Appl. Phys. A.* 119 (2015) 977–987.
- [261] V. Uvarov, I. Popov, Metrological characterization of X-ray diffraction methods at different acquisition geometries for determination of crystallite size in nano-scale materials, *Mater. Charact.* 85 (2013) 111–123.
- [262] P.E. Tomaszewski, The uncertainty in the grain size calculation from X-ray diffraction data, *Phase Transitions.* 86 (2013) 260–266.
- [263] H. Natter, M. Schmelzer, R. Hempelmann, Nanocrystalline nickel and nickel-copper alloys: Synthesis, characterization, and thermal stability, *J. Mater. Res.* 13 (2011) 1186–1197.
- [264] K. Pantleon, M.A.J. Somers, Interpretation of microstructure evolution during self-annealing and thermal annealing of nanocrystalline electrodeposits-A comparative study, *Mater. Sci. Eng. A.* 528 (2010) 65–71.
- [265] N. Wang, Z. Wang, K.T. Aust, U. Erb, Isokinetic analysis of nanocrystalline nickel electrodeposits upon annealing, *Acta Mater.* 45 (1997) 1655–1669.

- [266] A.A. Rasmussen, P. Møller, M.A.J. Somers, Microstructure and thermal stability of nickel layers electrodeposited from an additive-free sulphamate-based electrolyte, *Surf. Coatings Technol.* 200 (2006) 6037–6046.
- [267] W.A. Johnson, R.F. Mehl, Reaction kinetics in processes of nucleation and growth, *Trans. Metall. Soc. AIME.* 135 (1939) 416–442.
- [268] M. Avrami, Kinetics of phase change. I General theory, *J. Chem. Phys.* 7 (1939) 1103.
- [269] M. Avrami, Kinetics of phase change. II - Transformation-time relations for random distribution of nuclei, *J. Chem. Phys.* 8 (1940) 212–224.
- [270] E.J. Mittemeijer, *Fundamentals of Materials Science. The Microstructure-Property Relationship Using Metals as Model Systems*, Springer, Heidelberg, 2010.
- [271] W.W. Mullins, Theory of thermal grooving, *J. Appl. Phys.* 28 (1957) 333.
- [272] W.W. Mullins, The effect of thermal grooving on grain boundary motion, *Acta Metall.* 6 (1958) 414–427.
- [273] J.W. Cahn, The impurity-drag effect in grain boundary motion, *Acta Metall.* 10 (1962) 789–798.
- [274] K. Lücke, H. Stüwe, On the theory of impurity controlled grain boundary motion, *Acta Metall.* 19 (1971) 1087–1099.
- [275] C.V. Thompson, R. Carel, Texture development in polycrystalline thin films, *Mater. Sci. Eng. B.* 32 (1995) 211–219.
- [276] H.M. Ledbetter, R.P. Reed, Elastic properties of metals and alloys, I. Iron, nickel, and iron-nickel alloys, *J. Phys. Chem. Ref. Data.* 2 (1973) 531.
- [277] C. V. Thompson, R. Carel, Stress and grain growth in thin films, *J. Mech. Phys. Solids.* 44 (1996) 657–673.
- [278] U. Klement, L. Hollang, S.R. Dey, M. Battabyal, O.V. Mishin, W. Skrotzki, Effect of annealing on microstructural development and grain orientation in electrodeposited Ni, *Solid State Phenom.* 160 (2010) 235–240.
- [279] A. Berger, P.J. Wilbrandt, F. Ernst, U. Klement, P. Haasen, On the generation of new orientations during recrystallization: Recent results on the recrystallization of tensile-deformed fcc single crystals, *Prog. Mater. Sci.* 32 (1988) 1–95.
- [280] R.D. Doherty, Recrystallization and texture, *Prog. Mater. Sci.* 42 (1997) 39–58.
- [281] I. Samajdar, R.D. Doherty, Grain boundary misorientation in DC-cast aluminum alloy, *Scr. Metall. Mater.* 31 (1994) 527–530.
- [282] M. Hillert, On the theory of normal and abnormal grain growth, *Acta Metall.* 13 (1965) 227–238.
- [283] S.C. Mehta, D.A. Smith, U. Erb, Study of grain growth in electrodeposited nanocrystalline nickel-1.2 wt.% phosphorus alloy, *Mater. Sci. Eng. A.* 204 (1995) 227–232.
- [284] D. Fabrègue, B. Mouawad, C.R. Hutchinson, Enhanced recovery and recrystallization of metals due to an applied current, *Scr. Mater.* 92 (2014) 3–6.

- [285] T.Y. Hung, C.J. Huang, C.C. Lee, C.C. Wang, K.C. Lu, K.N. Chiang, Investigation of solder crack behavior and fatigue life of the power module on different thermal cycling period, *Microelectron. Eng.* 107 (2013) 125–129.
- [286] J.W. Nah, J.O. Suh, K.N. Tu, Effect of current crowding and Joule heating on electromigration-induced failure in flip chip composite solder joints tested at room temperature, *J. Appl. Phys.* 98 (2005) 013715.
- [287] M.L. Trouwborst, S.J. van der Molen, B.J. van Wees, The role of Joule heating in the formation of nanogaps by electromigration, *J. Appl. Phys.* 99 (2006) 114316.
- [288] S.N. Kharin, H. Nouri, T. Davies, The mathematical models of welding dynamics in closed and switching electrical contacts, in: *Proc. 49<sup>th</sup> IEEE Holm Conf. Electr. Contacts*, 2003, IEEE, 2003: pp. 107–123.
- [289] S.Y. Chang, C.F. Chen, S.J. Lin, T.Z. Kattamis, Electrical resistivity of metal matrix composites, *Acta Mater.* 51 (2003) 6291–6302.
- [290] R.J. Arsenault, N. Shi, Dislocation generation due to differences between the coefficients of thermal expansion, *Mater. Sci. Eng.* 81 (1986) 175–187.
- [291] Zhou Zhao, Song Zhijian, Xu Yingkun, Effect of microstructure on the mechanical properties of an Al alloy 6061-SiC particle composite, *Mater. Sci. Eng. A.* 132 (1991) 83–88.
- [292] F.M. Smits, Measurement of sheet resistivities with the four-point probe, *Bell Syst. Tech. J.* 37 (1958) 711–718.
- [293] M.J. Aus, B. Szpunar, U. Erb, A.M. El-Sherik, G. Palumbo, K.T. Aust, Electrical resistivity of bulk nanocrystalline nickel, *J. Appl. Phys.* 75 (1994) 3632.
- [294] E. Tóth-Kádár, I. Bakonyi, L. Pogány, Á. Cziráki, Microstructure and electrical transport properties of pulse-plated nanocrystalline nickel electrodeposits, *Surf. Coatings Technol.* 88 (1997) 57–65.
- [295] J.E. Darnbrough, B. Roebuck, P.E.J. Flewitt, The influence of temperature and grain boundary volume on the resistivity of nanocrystalline nickel, *J. Appl. Phys.* 118 (2015) 184302.
- [296] M. Nagasawa, S. Shionoya, Properties of Oxidized SnO<sub>2</sub> Single Crystals, *Jpn. J. Appl. Phys.* 10 (1971) 727–731.
- [297] A.F. Mayadas, Electrical resistivity model for polycrystalline films: the case of specular reflection at external surfaces, *Appl. Phys. Lett.* 14 (1969) 345.
- [298] A. Mayadas, M. Shatzkes, Electrical-Resistivity model for polycrystalline films: The case of arbitrary reflection at external surfaces, *Phys. Rev. B.* 1 (1970) 1382–1389.
- [299] R.K. Islamgaliev, K. Pekala, M. Pekala, R.Z. Valiev, The determination of the grain boundary width of ultrafine grained copper and nickel from electrical resistivity measurements, *Phys. Status Solidi.* 162 (1997) 559–566.
- [300] A. Misra, M.F. Hundley, D. Hristova, H. Kung, T.E. Mitchell, M. Nastasi, J.D. Embury, Electrical resistivity of sputtered Cu/Cr multilayered thin films, *J. Appl. Phys.* 85 (1999) 302.

- [301] E. Glickman, A. Inberg, V. Bogush, G. Aviram, N. Croitoru, Y. Shacham-Diamand, On the mechanism of annealing effect in electrical resistivity of sub-100 nm Ag (1% W) films, *Microelectron. Eng.* 76 (2004) 182–189.
- [302] H.C. Koo, J.J. Kim, Effects of stabilizing agents on film properties in Ag electroless plating, *J. Electrochem. Soc.* 155 (2008) D176.

## List of figures

<b>Fig. 2.1</b> Sequence of events during CVD reactions (adapted from [10]).....	6
<b>Fig. 2.2</b> Portrayal of a typical magnetron sputtering setup and the basic sequence of events during film deposition [20]. Electrons travelling close to the target (forced by a magnetic field) enhance ionisation and collision processes, increasing the sputtering yield.....	8
<b>Fig. 2.3</b> Basic representation of an electrodeposition cell, indicating its essential components. ....	10
<b>Fig. 2.4</b> Schematic of metallic-coating deposition by laser cladding. ....	13
<b>Fig. 2.5</b> Exemplary engineering applications where Ni-based coatings are readily used, namely: bearings, gears, pistons, carburettors, control valves, moulds, water pumps, gas-turbine compressors, landing gears, printed circuit boards and heatsinks.....	15
<b>Fig. 2.6</b> Corrosion pitting on (a) single-layer Ni plus Cr; (b) dual-layer Ni plus Cr; and (c) dual-layer Ni plus micro-discontinuous Cr (adapted from [33]).....	16
<b>Fig. 2.7</b> Phase diagram of the Ni-Ag system showing virtually no mutual solid solubility (reproduced from [9]). ....	24
<b>Fig. 2.8</b> Top view of SnO <sub>2</sub> -nanowire arrays of different morphology: (a) ordered array of short nanowires which sustained epitaxial growth; (b) disordered network of long nanowires; and (c) hierarchical nanowire structures obtained by secondary growth onto primary nanowires.....	26
<b>Fig. 3.1</b> (a) Schematic representation of VLS nanowire growth and (b) disordered network of long SnO <sub>2</sub> nanowires. ....	28
<b>Fig. 3.2</b> Ag-coated SnO <sub>2</sub> -nanowire arrays: (a) general and (b) close range visualisation....	29
<b>Fig. 3.3</b> Two-cathode electrochemical cell (and related equipment) employed for the electrodeposition of the Ni matrix of the composite.....	30
<b>Fig. 3.4</b> Comparison of the cathode potential evolution during the electrodeposition of a pure-Ni film and the Ni matrix of the Ni-Ag-SnO <sub>2</sub> composite. The sudden stabilisation of the cathode potential observed in the composite's curve is a good indicator of the moment at which the nanowires become completely embedded in the matrix.....	31
<b>Fig. 3.5</b> FIB/SEM dual-beam system used for cross-sectioning and imaging of the samples. FIB tomography, electron-backscatter diffraction and energy-dispersive X-ray spectroscopy analysis were also among its available features. ....	32
<b>Fig. 3.6</b> (a) Sink-in of a surface during indentation (which is normally the case for ductile metals), resulting in a reduced depth of contact ( $h_c$ ) with respect to the indenter's maximum displacement ( $h$ ). The opposite case is known as pile-up, where the indented material flows plastically and surrounds the indenter above the original surface plane. (b) Exemplary load-displacement curve obtained from a nanoindentation measurement. The contact rigidity ( $S$ ) is given by the slope of the unloading segment at maximum load. This magnitude, together	

with the applied load and $h$ , were used to derive all other parameters and material properties.....	35
<b>Fig. 4.1</b> Cross-section of an as-deposited Ni-Ag-SnO <sub>2</sub> film (prior to polishing and removal of excess Ni) imaged by (a) standard SEM and (b) FIB ion-channelling contrast. The former exposes clearly the gradient nature of the microstructure, where the dotted lines enclose regions (i-iv) of different composition in terms of reinforcement content. Here, the brighter phase embedded in a darker matrix corresponds to the Ag-SnO <sub>2</sub> . The second image (b) reveals the fine-grained morphology of the matrix, which resulted from the strong pinning of grain boundaries exerted by the Ag-coated nanowires during the Ni deposition.....	39
<b>Fig. 4.2</b> Surface view of electrodeposited Ni (a) onto Ag-coated SnO <sub>2</sub> nanowires (composite) and (b) on a flat substrate. Corresponding AFM topographic height profiles are also shown with their respective $R_q$ values. The presence of the nanowires translated into a 500% increase in roughness. ....	40
<b>Fig. 4.3</b> (a) Bright-field TEM image of the longitudinal section of a Ag-coated nanowire. The SAD patterns from (b) Ag and (c) SnO <sub>2</sub> were obtained from the areas enclosed by circles. ....	41
<b>Fig. 4.4</b> Bright-field STEM images displaying the (a) cross and (b) longitudinal sections of Ag-coated SnO <sub>2</sub> nanowires within a Ni matrix. ....	41
<b>Fig. 4.5</b> FIB-tomography reconstructions from (a) a Ni-Ag-SnO <sub>2</sub> composite film and (b) from arrays of free-standing SnO <sub>2</sub> nanowires. ....	43
<b>Fig. 4.6</b> Grain size distribution histograms (with their corresponding fitting curves) obtained by means of EBSD from (a) Ni-Ag-SnO <sub>2</sub> , (b) Ni <sub>cg</sub> and (c) Ni <sub>fg</sub> . The values of $d_A$ are shown with their standard deviation in brackets. ....	44
<b>Fig. 4.7</b> Ion-channelling-contrast images of FIB cross-sections of (a) Ni <sub>cg</sub> and (b) Ni <sub>fg</sub> samples. ....	45
<b>Fig. 4.8</b> [001] inverse pole figures recorded at the surface of (a) Ni-Ag-SnO <sub>2</sub> , (b) Ni <sub>cg</sub> and (c) Ni <sub>fg</sub> films.....	45
<b>Fig. 4.9</b> Exemplary nanoindentation load-displacement curves from the investigated films. ....	46
<b>Fig. 4.10</b> Hall-Petch plots from the hardness of (a) pure-Ni films, (b) pure Ni together with one data point corresponding to the Ni-Ag-SnO <sub>2</sub> and (c) composite films. The error bars are given by the standard deviation. ....	48
<b>Fig. 4.11</b> Strain-stress curves of the investigated films derived from nanoindentation data. ....	52
<b>Fig. 4.12</b> Hall-Petch plots from the yield stress of (a) pure-Ni and (b) Ni-Ag-SnO <sub>2</sub> films. The error bars are given by the standard deviation. ....	53
<b>Fig. 5.1</b> Evolution of $\mu$ for the tests at $F$ of (a) 5, (b) 10, (c) 20 and (d) 30 mN. ....	57
<b>Fig. 5.2</b> Mean normal displacement (i.e., penetration depth) of the sliding ball for the tests at $F$ of (a) 5, (b) 10, (c) 20 and (d) 30 mN.....	57

<b>Fig. 5.3</b> SEM micrographs showing wear tracks from all the types of samples under study for the tests at (a) 20 and (b) 30 mN. The white rectangles show examples of dark spots corresponding to oxygen-rich tribolayers.....	58
<b>Fig. 5.4</b> SEM micrographs showing the groove and side ridges of wear tracks produced at $F = 30$ mN on (a) Ni-Ag-SnO <sub>2</sub> , (b) Ni <sub>cg</sub> and (c) Ni <sub>fg</sub> . The white rectangles show examples of dark spots corresponding to oxygen-rich tribolayers.....	59
<b>Fig. 5.5</b> Oxygen-content measured at the entire surface of the groove of the wear tracks by means of EDS. The values are normalised according to the oxygen-content measured at the unworn surrounding area (0 mN). The error bars are given by the standard deviation. ....	60
<b>Fig. 5.6</b> FIB ion-channelling-contrast images from the cross-sections of wear tracks produced at $F = 30$ mN on (a) Ni-Ag-SnO <sub>2</sub> , (b) Ni <sub>cg</sub> and (c) Ni <sub>fg</sub> . In each case, a layer of plastically deformed grains is observed directly underneath the surface.....	62
<b>Fig. 5.7</b> Steady-state $\mu$ from all the evaluated samples and test conditions, calculated by averaging the value from the last 50 cycles of each test. The error bars (almost negligible) are given by the standard deviation. A pronounced dependence of $\mu$ on $F$ can be clearly observed. ....	65
<b>Fig. 5.8</b> $W$ from all the evaluated samples and test conditions, obtained by means of WLI. The error bars are given by the standard deviation. ....	67
<b>Fig. 5.9</b> Linear dependence of $W$ on $H$ for the (a) pure-Ni and (b) composite films. The error bars are given by the standard deviation. ....	69
<b>Fig. 5.10</b> Linear dependence on $F$ of both the slope and intercept from Eq. 5.4 ( $A$ and $B$ , respectively), which describes the linear relationship between $W$ and $H$ for (a) pure-Ni and (b) composite films. The error bars are given by the standard error in the calculation of $A$ and $B$ using the fit functions of Fig. 5.9.....	69
<b>Fig. 5.11</b> Results from the $W_{100}$ model of Eq. 5.7 for (a) pure-Ni and (b) Ni-Ag-SnO <sub>2</sub> films.	71
<b>Fig. 5.12</b> Examples of (a) measured normal-displacement curves and (b) their respective fitting through simple power-type functions, which are given by Eq. 5.8. ....	72
<b>Fig. 5.13</b> Correlation between $W$ and maximum $D$ (achieved at the end of the wear tests). A function analytically derived from the geometry of both the wear tracks and counter ball (Eq. 5.9) was found to properly describe this relationship. The error bars are given by the standard deviation. ....	74
<b>Fig. 5.14</b> Wear-rate curves of pure-Ni and composite films from the (a) 20 and (b) 30 mN tests, according to Eq. 5.12. The values beyond the 100 <sup>th</sup> cycle ( $t > 1000$ s) show the expected behaviour of the samples according to the model. ....	74
<b>Fig. 5.15</b> Analysis of the parameters (a) $\alpha$ and (b) $\beta$ from the power-function approximation of $D$ (Eq. 5.8). ....	76
<b>Fig. 6.1</b> FIB ion-channelling-contrast images together with inverse pole figure maps (recorded at the cross-section and at the surface, respectively) from as-deposited (a) Ni-Ag-SnO <sub>2</sub> , (b) Ni <sub>cg</sub> and (c) Ni <sub>fg</sub> films. ....	80

<b>Fig. 6.2</b> Pole figures of as-deposited (a) Ni-Ag-SnO <sub>2</sub> , (b) Ni <sub>cg</sub> and (c) Ni <sub>fg</sub> . The random crystallographic orientation of the composite contrasts with the <100> fibre texture of the pure-Ni films. ....	81
<b>Fig. 6.3</b> Grain size distribution of the as-deposited (a) Ni-Ag-SnO <sub>2</sub> , (b) Ni <sub>cg</sub> and (c) Ni <sub>fg</sub> films, showing the coefficient of determination, mean value and standard deviation of the fit functions. ....	82
<b>Fig. 6.4</b> Analysis of the onset and development of microstructure coarsening, which was performed by following in-situ the evolution of the FWHM <sup>-1</sup> of the main XRD peaks during non-isothermal annealing. ....	84
<b>Fig. 6.5</b> Texture evolution of (a) pure-Ni and (b) composite films, evaluated in-situ during non-isothermal annealing by means of the RTC. ....	87
<b>Fig. 6.6</b> FIB ion-channelling-contrast images together with inverse pole figure maps (recorded at the cross-section and at the surface, respectively) from (a) Ni-Ag-SnO <sub>2</sub> , (b) Ni <sub>cg</sub> and (c) Ni <sub>fg</sub> films isothermally annealed at 500 °C for 10 h. ....	89
<b>Fig. 6.7</b> FIB ion-channelling-contrast images together with inverse pole figure maps (recorded at the cross-section and at the surface, respectively) from (a) Ni-Ag-SnO <sub>2</sub> , (b) Ni <sub>cg</sub> and (c) Ni <sub>fg</sub> films isothermally annealed at 500 °C for 10 h. ....	90
<b>Fig. 6.8</b> Grain size distribution of (a) Ni-Ag-SnO <sub>2</sub> , (b) Ni <sub>cg</sub> and (c) Ni <sub>fg</sub> films after isothermal annealing at 500 °C for 10 h, showing the coefficient of determination, mean value and standard deviation of the fit functions. ....	91
<b>Fig. 6.9</b> Pole figures of (a) Ni-Ag-SnO <sub>2</sub> , (b) Ni <sub>cg</sub> and (c) Ni <sub>fg</sub> after isothermal annealing at 500 °C for 10 h. The composite retained its random crystallographic orientation, while the Ni samples evolved from a <100> to a <111> fibre texture due to surface energy minimisation. ....	93
<b>Fig. 6.10</b> Inverse pole figure maps of (a) Ni-Ag-SnO <sub>2</sub> , (b) Ni <sub>cg</sub> and (c) Ni <sub>fg</sub> after isothermal annealing at 300 °C for 10 h. An abnormal grain growth behaviour is evident in the case of the pure-Ni films. ....	95
<b>Fig. 6.11</b> Grain size distribution of Ni-Ag-SnO <sub>2</sub> after isothermal annealing at 300 °C for 10 h. The unimodal, lognormal nature of the experimental data suggests that a normal growth process took place. ....	96
<b>Fig. 7.1</b> Results of the 4-point probe experiments, where the indicated values are the characteristic $\rho$ of each type of sample. These were determined after the stabilisation of the measurements at maximum $I$ . In the case of Ag, smaller $I$ were required due to the much lower thickness of these films. ....	100
<b>Fig. 7.2</b> SEM micrograph showing the cross-section of a Ni-SnO <sub>2</sub> film. ....	101

## List of tables

<b>Table 2.1</b> Basic compositions of the most relevant types of electrolytes used for the electrodeposition of Ni, namely the Watts and Ni-sulfamate solutions [33].	12
<b>Table 2.2</b> Characteristic physical and mechanical properties of Ni [5].	14
<b>Table 2.3</b> Characteristic physical and mechanical properties of Ag [48,123].	23
<b>Table 2.4</b> Characteristic physical properties of SnO <sub>2</sub> [133].	25
<b>Table 3.1</b> Compositions of the pretreatment solutions and electroless bath used for depositing Ag onto SnO <sub>2</sub> -nanowire arrays.	28
<b>Table 3.2</b> Bath composition used during the electrodeposition of the Ni matrix onto the Ag-coated SnO <sub>2</sub> nanowires.	30
<b>Table 4.1</b> Hardness and Young's modulus of the samples, obtained by nanoindentation (standard deviation in brackets).	46
<b>Table 4.2</b> Results of the calculation of the composite's Young's modulus from different models based on the rule-of-mixtures, together with their deviation from the measured values.	50
<b>Table 4.3</b> Parameters associated to the plastic behaviour of the films under uniaxial tension (given by Eq. 4.3), which were calculated from indentation data. Standard deviation values are listed in brackets.	52
<b>Table 5.1</b> Area-weighted average grain diameter, mechanical properties and roughness of the samples, obtained by EBSD, nanoindentation and WLI, respectively (with the standard deviation in brackets).	56
<b>Table 5.2</b> Zum Gahr's cutting-efficiency parameter calculated for all the studied samples. The low values obtained indicate ploughing-type wear behaviour. Standard deviation values are listed in brackets.	60
<b>Table 5.3</b> Maximum contact pressure according to the Hertzian elastic-contact model, calculated for the investigated samples and experimental conditions.	61
<b>Table 5.4</b> Estimation of flash temperatures for the performed tests, expressed as the temperature difference between the hot real-contact areas and the bulk, according to different models available in the literature [217–220].	63
<b>Table 5.5</b> Evaluation of the parameter $k$ from Archard's model for the performed tests. In all cases, the values of $k$ indicated the occurrence of severe wear ( $k \geq 10^{-4}$ ).	67
<b>Table 5.6</b> Coefficients of the linear fit functions describing the relationships of $A$ and $B$ (from Eq. 5.4) with $F$ , according to Eq. 5.5.	70
<b>Table 5.7</b> Parameters of the power functions used for fitting the experimental data concerning the evolution of $D$ during wear tests (Eq. 5.8).	72
<b>Table 5.8</b> Fitting parameters involved in the modelling of the wear rate, used for calculating $\alpha_H$ and $\beta_m$ (the latter being a constant, which is listed in the table).	76

<b>Table 6.1</b> Linear thermal expansion coefficients of the materials under study.....	85
<b>Table 6.2</b> Results of the oriented nucleation vs oriented growth analysis. ....	94

